RIVISTA DEL NUOVO CIMENTO Vol. 40, N. 2 2017
DOI 10.1393/ncr/i2017-10132-x

Laser acceleration

T. Tajima([1])(*), K. Nakajima([2]) and G. Mourou([3])

([1]) *Department of Physics and Astronomy, University of California, Irvine, CA 92697, USA*
([2]) *Center for Relativistic Laser Science, Institute for Basic Science (IBS), Gwangju 61005, Korea*
([3]) *IZEST, Ecole Polytechnique, 91128, Palaiseau, France*

received 15 August 2016

Summary. — The fundamental idea of Laser Wakefield Acceleration (LWFA) is reviewed. An ultrafast intense laser pulse drives coherent wakefield with a relativistic amplitude robustly supported by the plasma. While the large amplitude of wakefields involves collective resonant oscillations of the eigenmode of the entire plasma electrons, the wake phase velocity $\sim c$ and ultrafastness of the laser pulse introduce the wake stability and rigidity. A large number of worldwide experiments show a rapid progress of this concept realization toward both the high-energy accelerator prospect and broad applications. The strong interest in this has been spurring and stimulating novel laser technologies, including the Chirped Pulse Amplification, the Thin Film Compression, the Coherent Amplification Network, and the Relativistic Mirror Compression. These in turn have created a conglomerate of novel science and technology with LWFA to form a new genre of high field science with many parameters of merit in this field increasing exponentially lately. This science has triggered a number of worldwide research centers and initiatives. Associated physics of ion acceleration, X-ray generation, and astrophysical processes of ultrahigh energy cosmic rays are reviewed. Applications such as X-ray free electron laser, cancer therapy, and radioisotope production etc. are considered. A new avenue of LWFA using nanomaterials is also emerging.

(*) Recipient of the Italian Physical Society "Enrico Fermi" Prize 2015.

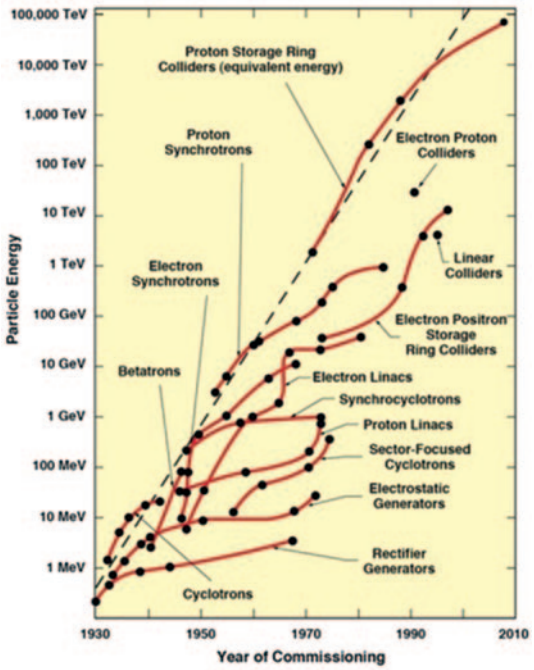

Fig. 1. – Livingston chart (from ref. [1]).

1. – Introduction

1˙1. *The basic philosophy of Laser Wakefield Acceleration.* – In this paper we would like to form a fundamental framework of how to drive robust accelerating fields in a medium of plasma. The introduction of plasma as an accelerating medium rather than accelerating in a vacuum (surrounded by a metal/dielectric) is in part forced by the current necessity to increase the accelerating gradient beyond the breakdown limit. This is in a sense a crisis in the well-established tradition of accelerator physics to rely on the tightly organized structured material (solid-state metal or dielectric) so that the accelerator is well controlled by the external materials and magnets. This crisis may be seen in the recent (*i.e.* the latest few decades) saturation in the energy growth rate in the Livingston Chart (as modified over that of the original Livingston one [1]). See fig. 1. One sees that the recent increment of the energies of accelerators has ceased to become exponential, and shows rather linear (in time, which is seen as saturation in the semi-logarithmic Livingston). Thus the increase of energies is currently being accomplished not by the new methods, but by increasing the amount of the measures implemented. The solid-state materials, in spite of their superior structural sturdy stability, face their inherent weakness when challenged to increase the accelerating field beyond their breakdown field. This is because the solid material is organized by the quantum-mechanical binding potential (whose strength (or energy) is characterized as $\sim$ eV). On the other hand, the ionized materials of plasma are characterized by their kinetic energy of particles $\gg$ eV.

When the material is ionized by the strong field imposed by the mechanism of breakdown, or by the heating exceeding the temperature $>$ eV, the plasma does not possess the organizational force that makes atoms (or solids) hold together. Thus our task is

Fig. 2. – In the left panel the high phase velocity wakefield showing sustained and coherent structure, while in the right panel tsunami wave approaching onshore, losing its phase velocity to become violent.

now to discover an organizational principle alternative to the above atomic cohesion. We recognize that the plasma is amorphous, as its name arose from the amebic plasma cell in the blood. What the plasma has is the long-ranged collective force that, if properly marshaled, can organize itself into coherent and large amplitude plasma (Langmuir) oscillations or plasmons, whose length is characterized by the collisionless skin depth c/ω_{pe} where ω_{pe} is the electron plasma frequency rather than the de Broglie length. In this paper we show the following. First, through the resonant excitation (just like a swing) we can use this plasma's eigenmode to sustain collective and coherent waves. Secondly, we recognize that even an extremely high-amplitude wave, if it has high phase velocity, does not make wave-particle interaction with the plasma bulk particles and remains robust and does not destroy the plasma. See fig. 2 (wakefield wave and tsunami wave). This high-phase velocity principle is akin to the observation that a tsunami wave offshore having a high phase velocity does not involve resonant interaction with objects (such as ships) that float on the ocean, while the tsunami onshore upon decelerating its phase velocity can render devastating damage on objects as it begins to resonate. Thirdly, extending the above second principle when the high phase velocity approaches the speed of light c, the excited structure of the wake is speeding also at (or near) the speed of light. Since the electrons that respond to this immense wake cannot exceed the speed of light by the relativistic dynamics, the electrons at the crest of the wave tend and converge to this velocity, showing what we call the relativistic coherence [2]. Lastly, we recognize that it is difficult for the plasma to go unstable if the time scale of the drive is far shorter than that for ions to respond. The overall plasma cannot get destroyed as electrons get to restore back to where ions stand. (By extension this ultrafast motion cannot cohere with slow electron motion either). This is the principle of ultrafast dynamical stability going beyond much shorter than the ion time scales.

Related to the ultrafast requirement (the fourth principle), it is interesting to look at the frequency (or inversely the period) of the driving force. The simplest accelerator of electrons may be a capacitor. In the capacitor a DC (*i.e.* zero frequency) electrostatic field is applied between two places and electrons are accelerated to the energy of the voltage between the two plates. The van de Graff accelerator is similar in this sense. In these accelerators the frequency of the accelerating fields is essentially zero. As pointed out above relating to Principle 2 and Principle 4, when the field is DC (and thus the phase velocity is zero), the breakdown of the medium or the wave motion can take place to destroy the accelerating structure readily. This is (at least one of the reasons) why in the Livingston Chart (fig. 1) the second generation of accelerators begins to acquire a high velocity. This is because then the wave can "run away" from trouble (*i.e.* instability).

In order to accomplish this, accelerator physicists introduced RF (in the frequency of some 10^{10}/s within a couple of orders of magnitude) accelerators. These are cyclotrons, synchrotrons, and linacs (see fig. 1), in which the phase velocity has been hiked up (up to the speed of light, ultimately). Thus such photons have energy of $\sim 10^{-4}$ eV (within an order of magnitude). All accelerators in the Livingston Chart (fig. 1) use photons of energy 0–10^{-4} eV. On the other hand, in the ultrafast regime (and Principle 4 above) the time scales are in fs. Thus in the usage of optical lasers, we have the photons that drive these particles with the energy of eV. In this regard, this is a leap from the conventional accelerators' photon energy in the neighborhood of zero *i.e.* $\sim 10^{-4}$ eV to eV in our laser accelerators. As we will see, this leap of several orders resulted in an equal leap in the accelerating gradient. (As we will discuss in sect. **6**, we will try to further increase the photon energy of the driver to another 3 or 4 orders of magnitude beyond eV photons of optical lasers.)

To embody these organizational principles, Tajima and Dawson [3] proposed the employment of an ultrashort and intense laser pulse to excite a wakefield in such a way that the laser pulse length l_0 is resonant to the wavelength of the eigenmode of the plasma, *i.e.* half of the plasma wavelength $l_p = 2\pi c/\omega_{pe}$. This choice of resonant wavelength is to efficaciously excite the coherent eigenmode of the plasma without causing other disturbances in it, satisfying the first guiding principle above. The laser in the underdense plasma speeds at the phase velocity close to the speed of light, which of course is much higher than the thermal speed of electrons, realizing the above second condition. Such a short pulse length to make the plasma wavelength resonance is in the fs regime, thereby not disturbing ions. This embodies the fourth principle above. In most recommended cases, we select the frequency of the laser much higher than the plasma frequency, which leads to set the Lorentz factor γ_p of the phase velocity of the wakefield much greater than unity. This introduces relativistic coherence, the guiding direction mentioned as third point above. The recommended intensity of the laser pulse is such that the ponderomotive potential (the photon pressure force potential) of the laser in the plasma amounts to $\Phi = mc^2\sqrt{1+a_0^2}$ so that the excited plasma wave motion acquires the electron momentum of mca_0. Here the normalized vector potential of the laser is $a_0 = eE_0/m\omega_0 c$ and E_0, ω_0 are the electric field and frequency of the laser. The ponderomotive force arises from the nonlinear Lorentz force $v \times B/c$, which causes the polarization of electrons in the plasma in the longitudinal direction, even though the electric field of the laser is in the transverse direction. This polarization $E_p = m\omega_p c a_0/e$ yields the electrostatic field in the longitudinal direction in the same magnitude. This is the rectification of the transverse field of laser into the longitudinal wakefield. This is the origin of the excited wakefield. When a_0 of the laser is greater than unity, such a laser is called relativistic (intensity). At the verge of relativistic strength, *i.e.* $a_0 = 1$, the wakefield amplitude assumes the value of $E_p = m\omega_p c/e$. This is the wave breaking field in the nonrelativistic case. The wave tends to break if the wave amplitude is high so that the high-amplitude portion of the wave typically propagates faster than the lower portions and takes over those. The relativistic phase of intense laser also makes the amplitude of the wakefield E_p relativistically intense, *i.e.* $a_p = eE_p/m\omega_p c$ greater than unity. Note here to distinguish the phase velocity of wakefield being relativistic ($\gamma_p \gg 1$) and the laser amplitude being relativistic $a_0 \gg 1$. However, it is of interest to recognize that the latter $a_0 \gg 1$ provides the relativistic coherence to the wakefield and the realization of relativistically coherent wakefield possible $a_p \gg 1$ [2].

Once we introduce the method and mechanism behind relativistically coherent and robust wakefield as above by the short pulsed electromagnetic (EM) waves (laser wakefield

accelerator (LWFA)), it is not difficult to also introduce the wakefield driven by a bunch of relativistic charged particles (such as electron bunch [4] and ion bunch [5]). In the latter the charged particles' electric fields point in the radial direction, while the magnetic fields introduced by the beam current are in the azimuthal direction, making the ponderomotive force essentially identical to the pulsed EM (or laser) waves. We may call all these methods as wakefield acceleration as a whole.

It is also transparent that this method is not restricted to the frequency of the driving EM waves. Although the vast majority of the experiments of LWFA have been carried out in the eV ranged optical laser (because of its availability ([6]; see sect. **2**)), the frequency may be doubled or tripled, or even into the X-ray regimes (see sect. **3** and sect. **6**). We also find that in astrophysical phenomena such as in the active galactic nuclei the shock-driven EM waves have astrophysical long wavelength and thus low frequency, while their value of a_0 may be extremely high.

The coherence and robustness of wakefield acceleration of electrons have been invented as a response to a series of experiences, lessons, and inventions to overcome the difficulties during the research that ensued after Veksler's work in 1956 [7]. In addition, the four pillars of wakefield [3] made one more point: the pickup of electrons in the excited wakefield is easy, while the high phase velocity of LWFA would have a difficult time to trap much heavier ions. This is because the ion trapping takes adiabatic acceleration (see sect. **5**).

1˙2. *Historical background of plasma acceleration.* – We now review the historical developments how these principles have been found and/or developed. Veksler introduced the concept of collective acceleration in 1956 [7]. His vision consisted of two elements. The first element is the introduction of plasma as the accelerating medium. In the conventional acceleration method when we increase the accelerating electric field in a vacuum surrounded by a metallic tube, the electric field on the surface of the metallic walk increases and eventually the surface begins to spark, yielding electron breakdown of the metal. As is necessary in most accelerator structure, waveguide comes with a slow wave structure. Such a structure is accompanied by a protruded surface metallic structure, which makes the local electric field even greater. In addition, most materials contain impurities within their structure, such as f-centers. These in combination make the metallic breakdown field far greater than the typical gradient that shifts the electronic wave function by an eV over an Å, *i.e.* electric field of 10^8 eV/cm down to typically MeV/cm (or even less). In order to overcome this difficulty Veksler suggested to use the already broken down material of plasma to begin with. His second element is to resort to the collective field as opposed to individual force. As is known, the fields in plasma permeate in such a way that a charge feels nearly from all charges through the Coulomb interaction. If we further marshal the plasma to form a collection of charges made up with $(Ne)^2$ (a collection of N charges), the interaction force is proportional to $(Ne)^2$, indicating that the collective force is proportional to N^2, as opposed to the conventional linear force proportional to N. (If N is 10^6, the collective force is 10^6 times greater than its linear counterpart).

Lured by this concept, a large body of investigations ensued [8-11]. Norman Rostoker's program was one of them (some of these efforts are reviewed in the Proceedings of the Norman Rostoker Memorial Symposium, [12]). For example, in one of these attempts [13] it was suggested that once an electron beam is injected into a plasma to cause a large-amplitude plasma wave by the beam-plasma interaction (a collective interaction), such large amplitude wave would trap ions and accelerate them to a speed similar to that

of the electron beam. If ions were to be trapped by speeding electron cloud or beam with energy ε_e, the ions would be accelerated to the energy of $\varepsilon_i = (M/m)\varepsilon_e$, where M and m are masses of ions and electrons, respectively, because they would speed with the same velocity. Since the mass ratio M/m of ions to electrons is nearly 2000 for protons and greater for other ions, the collective acceleration of ions would gain a large energy boost. None of the collective acceleration experiments in those days, however, found energy enhancement of such magnitude mentioned above. The primary reason for this was attributed to the sluggishness (inertia) of ions and the electrons being pulled back to ions, instead of the other way around, too fast "reflexing (return flow) of electrons" as described in [14] (see also [15]). The ion acceleration takes place only over the sheath of electrons (of the beam injected) that are ahead of ions, while the sheath is tied to the beam injection aperture (an immovable metallic boundary in this experiment). As we see in more detail, Mako and Tajima theoretically found that the ion energy may be enhanced only by a factor of $2\alpha + 1$ (which is about 6 or 7 for typical experimental situations and α will be defined later in sect. **2**) over the electron energy, instead of by a factor of nearly 2000, due to the electron reflexing and no co-propagation of the electron beam and the ions, while the formed sheath is stagnant where it was formed. (For example, Tajima and Mako suggested to reduce the culpable electron reflexing by providing a concave geometry. Similar geometrical attempt to facilitate the laser-driven ion acceleration would appear also later in 2000's–2010's.) In the year 2000 the first experiments [16-18] to collectively accelerate ions by laser irradiation were reported. In these experiments a thin foil of metal (or other solid materials) was irradiated by an intense laser pulse, which produced a hot stream of electrons from the front surface that faced the laser pulse, propagating through this foil emerging from its back surface. Now this physical situation of what is happening at the rear surface of the foil is nearly equivalent to what the group of Rostoker had done in 1970's and 80's in terms of the dynamics of electrons emanating from the metallic boundary and its associated ion response. The superheated electrons by the laser caused the acceleration of ions in the sheath which was stuck stationary on the rear surface of the target, but not beyond. Such acceleration was then called the Target Normal Sheath Acceleration (TNSA) [16-19]. (The words "target normal" were attached, as in some of the experiments the laser injection was away from the normal direction of the surface. Yet, the accelerated ions were in the normal direction of the rear surface. This shows that the ion momentum was not a direct transfer of the laser photon momentum, but an indirect one via the conversion through the electron heating. The more direct momentum conversion remained a task for the future.) Since then, a large amount of effort has been steadily dedicated to this subject. See fig. 3. We revisit some of the electron dynamics in detail and analyze subsequent ion dynamics. Since much of the similarities of the physics at the sheath and somewhat lost knowledge of the earlier (70's and 80's) research, it may not be without merit to revisit this analysis below. From such a discussion we hope that we can connect the research of the earlier collective acceleration and the contemporary laser ion acceleration and learn the lesson from the former for the latter.

Because of the advantage in accelerating limited mass by laser to cope with the mismatch between the electron and ion dynamics as discussed above, experiments producing high-energy ions from sub-micrometer to nanometer targets much thinner than ones in early experiments driven by ultrahigh contrast (UHC) short-pulse lasers [20-24] have attracted a recent strong interest. Of particular focus is how much the ion energy enhancement is observed in the experiments and simulations in these thin targets and how it scales with the laser intensity. An alternative to reduce the amount of mass of acceler-

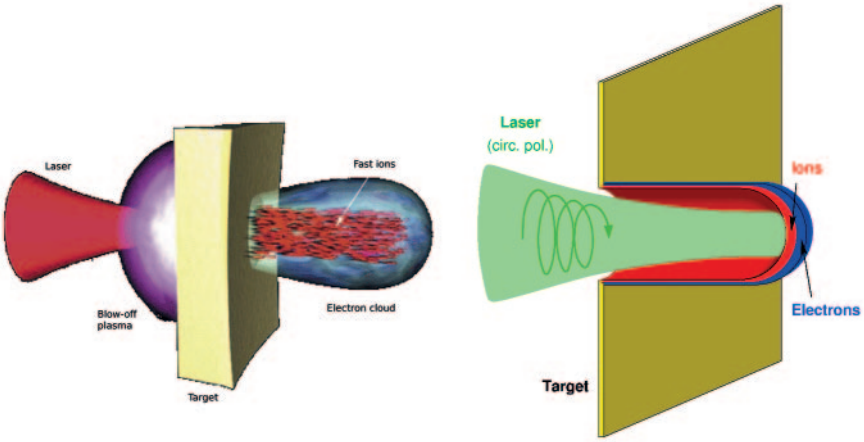

Fig. 3. – The Comparison of the TNSA laser-target interaction and the CAIL one. In the TNSA (left), the target remains unmoved, behind which a sheath is formed and ion acceleration is limited over this sheath. When the target is sufficiently thin (right), some portion of the target may co-move with the ponderomotively accelerated electron layer. This achieves partial coherence of ion motion behind the electron sheet (from ref. [31]).

ated matter is to increase the accelerating laser force, *i.e.* the ponderomotive force and its induced electrostatic force. If we increase this sufficiently large so that this wave can capture even heavier ions, we should be able to accelerate ions. The first of this kind of ion acceleration was suggested by the Radiation Pressure Acceleration (RPA) [25].

One way of achieving the capture of ions with as small as possible mass with as large as possible ponderomotive force may be discussed through the competition between the target thickness d and the laser strength parameter a_0 [26]. The experiments and simulations lately show that the proton energy increases as the target thickness decreases for a given laser intensity, and that there is an optimal thickness of the target (at several nm) at which the maximum proton energy peaks and below which the proton energy now decreases. This optimal thickness for the peak proton energy is consistent with the thickness dictated by the relation $a_0 \sim \sigma = \frac{n_0}{n_c}\frac{d}{\lambda}$, where σ is the (dimensionless) normalized electron areal density, a_0, d are the (dimensionless) normalized amplitude of electric field of laser and target thickness [26-28]. Here we introduce the dimensionless parameter of the ratio of the normalized areal density to the normalized laser amplitude $\xi = \sigma/a_0$. This optimal condition is understood as arising from the condition that the radiation force pushes out electrons from the foil layer if $\sigma \leq a_0$ or $\xi \leq 1$, while with $\sigma \geq a_0$ or $\xi \geq 1$ the laser pulse does not have a sufficient power to cause maximal polarization to all electrons. Note that this optimal thickness for typically available laser intensity is much smaller than for cases with previously attempted target thicknesses (for ion acceleration). See fig. 4 for increased degrees of adiabaticity of ion acceleration. In the case of fig. 4(a) laser generates energetic electrons on the front surface of the thick target. Electrons travel through the target to emerge from the rear side with a broad energy spread. These electrons exit into vacuum to pull ions. However, most electrons are pulled back to the immobile target before ions gain much energy. Electrons at the margin of the electron cloud are ejected out by the electron space charge. In the case of fig. 4(b) electrons with the delta function energy spectrum enter from the metallic

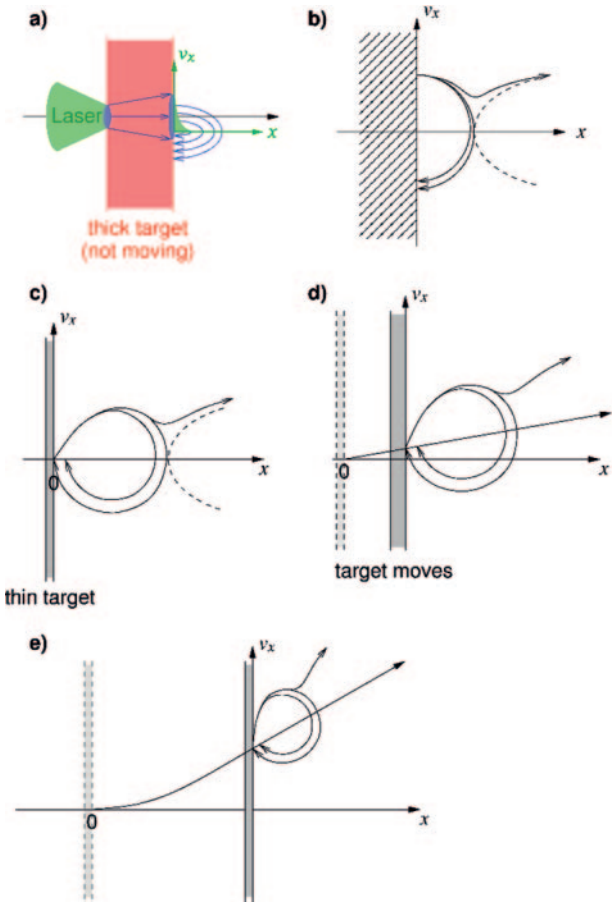

Fig. 4. – Various degrees of target motions from the total detachment from the electron sheet (a) to totally co-moving case (e). (a) TNSA. (b) The Mako-Tajima scenario. (c) A case study with an ultrathin target that is immobile. (d) When the target is sufficiently thin. (e) When the target is pushed with the laser ponderomotive force (such as the circularly polarized laser pulse) without too much heating of electrons and adiabatic acceleration to a degree (from ref. [31]).

immobile (real) surface. Electrons rush out in vacuum to pull ions. However, most electrons are pulled back to the immobile boundary before ions gain large energy. Some electrons are ejected forward. The electron dynamics is much in common with case (a), although the electron spectrum is broad and has a tail in (a). Now for the case fig. 4(c) one significant difference of (c) from (a) is that the electron energy is directly determined by the laser and its ponderomotive potential beyond the rear surface of that target. Thus the energy of ions is expected to be narrow in its width and to have higher maximum than (a). When the target is sufficiently thin (fig. 4(d)) the rear surface of the target (and sometimes entire target) begins to move, while the laser interacts with the target. When the target is pushed with the laser ponderomotive force (such as the circularly polarized laser pulse) without too much heating of electrons (fig. 4(e)), ions in the target as a whole are trapped in an accelerating bucket with tight phase space circles. If and when the laser leaks through and electrons are ejected forward, the bucket may begin to

collapse. Cases (c)–(e) belong to the regime of CAIL, while (e) is in particular in the RPA conditions (these points are to be discussed further in sect. **5**). One additional way to increase the adiabaticity of ion acceleration by laser is to institute the plasma property to gradually (and thus adiabatically) change over the propagation direction. An earliest example of this idea was proposed by Rau *et al.* [29]. Here their approach was to excite the Alfvén wave that varies its phase velocity as a function of the magnetic field $B(z)$ and/or the plasma density $n(z)$ (as the Alfvén velocity $v_A(z) = B(z)/(4\pi n(z)M)^{1/2}$) in such a way to increase $v_A(z)$ from a small value to a larger one, which can in turn change the phase velocity of the accelerating field gradually increasing over the distance (z).

Thus we attribute the observed enhanced value of the maximum proton energy in the experiment [30] to the ability to identify and provide prepared thin targets on the order of nm to reach this optimal condition. This experiment has been analyzed closely [31,32]. In reality at this target thickness the laser field teeters over partial penetration through the target, rendering the realization of optimum rather sensitive. Under this condition, electron motions maintain primarily those organized characteristics directly influenced by the laser field, rather than chaotic and thermal motions of electrons resulting from laser heating. In 1D Particle-In-Cell (PIC) simulation we observe that momenta of electrons show in fact coherent patterns directing either to the ponderomotive potential direction, the backward electrostatic pull direction, or the wave trapping motion direction, in a stark contrast to broad momenta of thermal electrons. In another word, through a very thin target the partially penetrated laser fields enable the electrons to execute dynamic motions still directly tied with the laser rather than thermal motions. We note that the ponderomotive force due to this trapped radiation contributes to the acceleration of electrons in this sheet and thus retards these electrons from being decelerated by the electrostatic force emanated from the diamond foil. In a typical sheath acceleration scheme the termination of ion acceleration commences due to this electron reflexing by the electrostatic field and the lack of adiabatic acceleration.

On the other hand, most of the theories have been based on the so-called Plasma Expansion Model (PEM) [19], which is motivated by much thicker and massive target. In this regime electrons are first accelerated by the impinging relativistic laser pulse and penetrate the target driven by ponderomotive force. Leaving the target at the rear side, electrons set up an electrostatic field that is pointed normal to the target rear surface, which is the so-called TNSA (Target Normal Sheath Acceleration) acceleration. Most electrons are forced to turn around and build up a quas-istationary electron layer. These fast electrons are assumed to follow thermal or Boltzmann distribution in theoretical studies of the conventional TNSA mechanism for thicker targets [19,21,33,34] where the acceleration field is estimated by the exponential potential dependency in the Poisson equation. Though this mechanism is widely used in the interpretation of the experimental results, it does not apply to the ultrathin nanometer scale targets, because the direct laser field and attenuated partially transmitted laser pulse play an important role in electron dynamics and the energetic electrons oscillate coherently, instead of chaotic thermal motions. Based on a self-consistent solution of the Poisson equation and TNSA model, Andreev *et al.* [20] had proposed an analytical model for thin foils and predicted the optimum target thickness at about 100 nm. It obviously does not explain the experimental results [30,35].

In conclusion, the past research has shown the following. There were early critics who worried about the plasma instability destroying the integrity of wakefield, as they believed that plasma is "inherent unstable" and particularly if we impose such a strong wave on plasma. Such worry proved to be not the case. As discussed, the driver of

the wakefield (a shout bunch of laser, or charged particle beam) runs away from the plasma where it produces the disturbance in the form of wake so fast (typically at or near the speed of light, which is far greater than the thermal speed of the plasma) that the wakefield phase which follows driver cannot become resonant with the thermal plasma. Thus the wakefield remains robust but does not get destroyed by the plasma instability. In fact its amplitude could grow as large as it could till the wave-breaking limit (if it is a nonrelativistic case) or remains further robust (in the case in which the relativistic coherence acts on it [2]). We have discussed if and when such conditions are fulfilled and when such conditions are not realized. Earlier experiences to follow Veksler's collective acceleration ran into some of the difficulties in which the accelerating structure in fact became unstable due to the plasma instabilities. These are invariably due to the slow phase velocity of the excited waves (see fig. 4). We learned a valuable lesson from this: for example, the first author (TT) was working in the laboratory of Prof. Rostoker in the early 1970's when such low phase velocity structure that was tied to the plasma boundary was deleterious for the appropriate acceleration conditions. We re-experienced such mechanism in 2000 when the early laser-driven ion acceleration encountered similar physics. In the case of electron acceleration, as electrons are light with respect to the strength of the wake, it can easily trap electrons and can carry away once they are within the trapping condition [36]. On the other hand, ions are heavy and their trapping by a fast phase velocity is difficult so that a gradual phase velocity increment (adiabatic process) is necessary. In the following sections, we will learn these experiences and conditions. We also learn how these discoveries impacted on many new developments that were not foreseen in [3].

Section **2** introduces the latest progress on the base technology of ultrafast and ultraintense lasers that has enabled the LWFA so far and will further spur its research and actual applications. Section **3** reviews the fundamental LWFA scalings that have been obtained from theory and simulation and well realized and verified by experimental research. LWFA not only may be the foundation for future colliers, but also may provide a unique access to fundamental physics that are not based on this standard luminosity paradigm, on which sect. **4** discusses. Section **5** is dedicated to discuss on laser acceleration of ions comparing its common as well as distinct physical processes from that of electrons. Section **6** introduces the possibility that is opened up by the latest laser compression technique and novel acceleration regime of LWFA, commencing the zeptosecond science. We find a plenty of wakefield acceleration processes in display in the Nature, particularly in the astrophysical accretion disks and their jets, as detailed in sect. **7**. There emerge a large class of applications of LWFA, one of which is the LWFA creation of high energy photon sources (X-rays and gamma-rays), the subject of sect. **8**. Medical and pharmaceutical applications of LWFA are among the important ones of its applications, as detailed in sect. **9**, many of which are branching out from earlier sections (**3**, **5**, and **8**). Section **10** concludes our LWFA review of and its prospect for the future research and exciting applications as well as possible impacts on far-reaching fields just emerging.

2. – Laser compression

One of the basic requirements for LWFA [3] mentioned in Introduction in sect. **1**. is to have an ultrafast intense laser pulse compression (in the fs regime). The technique of Chirped Pulse Amplification (CPA) [38] was invented timely to meet this requirement. A major review on this demand and realization of CPA is found in [6]. Thus we will not

repeat this here. The CPA had spurred the experimental realization of LWFA in a major way. By so doing it further spurred along with LWFA the advent of high-field science [6, 39]. As we will see in sect. **3**, the LWFA demands on the collider specs have further stimulated the intense laser technology in an entirely new direction and horizon as the invention of CAN (Coherent Amplification Network) fiber laser system [40]. This was to answer the call for high-repetition rated, high-efficiency intense laser needed for the high-luminosity collider beam drivers [41, 42]. In recent years there arose demands for high-energy LWFA requiring low density of the accelerating plasma (or high frequency of laser drive). The lower the density is, the higher the laser energy required becomes (see sect. **3**). The initiative of compressing high-energy lasers of nanoseconds into those in femtoseconds has also inspired methods for compression of high-energy laser on the one hand, while further compression desires (beyond CPA) of fs lasers into the regime of single-cycled laser (in a few fs) have arisen. The thin film compression (TFC) technique [37] was born from this demand. In this section we will delineate this development in detail. It is remarkable to note that this single-cycled optical laser compression opened a way to create a single-cycled X-ray laser possibility, which would be never imagined as possible so readily till the arrival of TFC. This is because the earlier innovation of the relativistic mirror compression of optical laser pulse works best in converting a single-cycled regime of optical laser into single-cycled X-ray laser pulses [43, 44]. This development further opened a path toward the X-ray LWFA possibility [45], as discussed in sect. **6**. This is an alternative way to access LWFA scaling (sect. **3**) by increasing the critical density instead of decreasing the plasma density. Such developments revolutionize both ultraintense lasers (into EW lasers) and ultrafast pulse lasers (into zeptoseconds), as predicted by the Pulse Duration-Intensity Conjecture (sect. **6**) [46]. Such laser pulses are so unique that we still need a lot to learn in the future on their implications.

There is a tendency to think that ultrashort pulse is a prerogative of small-scale laser. In the pulse duration-peak power conjecture [46] the opposite was demonstrated. Pulse duration and peak power are entangled. To shorten a pulse, it is necessary first to increase its peak power. In this article we show an example that illustrates this prediction, making possible the entry of laser into the zeptosecond and exawatt domain.

Since the beginning of the 1980's optical pulse compression [47] has become one of the standard ways to produce femtosecond pulse in the few cycle regime. The technique relies on a single-mode fiber and is based on the interplay between the spectrum broadening produced by self phase modulation and the Group Velocity Dispersion necessary to stretch the pulse. The combination of both effects contributes to create a linearly frequency-chirped pulse that can be compressed using dispersive elements like grating pairs, prism pairs or chirped mirrors. In their pioneering experiment Grischkowsky *et al.* [47] used a single-mode optical fiber and were able to compress a picosecond pulse with nJ energy to the femtosecond level. This work triggered an enormous interest that culminated with the generation of a pulse as short as 6 fs corresponding to 3 optical cycles at 620 nm by Shank's group [48] see fig. 5. In their first experiment the pulse was only 20 nJ, clamped at this level by the optical damage due to the core small size. To go higher in energy, Svelto and his group [49] introduced a compression technique based on fused silica hollow-core capillary, filled with noble gases and showed that they could efficiently compress their pulses to the 100 μJ level. Refining this technique, Svelto, Krausz *et al.* [50] could compress a 20 fs into 5 fs or 2 cycles of light at 800 nm, where the energy was typically sub mJ. In both cases, like with single-mode fiber, the compression effect was still driven by the interplay between self-phase modulation and group velocity dispersion.

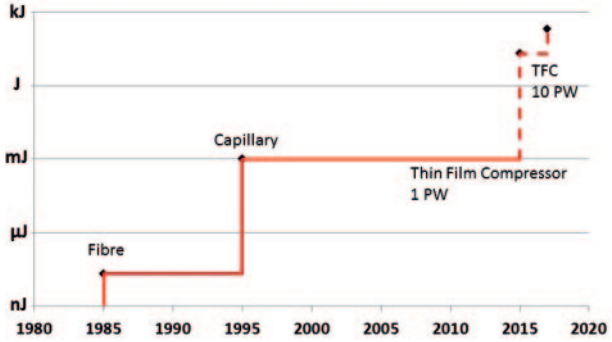

Fig. 5. – Evolution of few optical cycle pulses over the years.

To go higher in energy, bulk compression was attempted by Corkum and Rolland [51]. See fig. 5. In their embodiment the pulse is free propagating and not guided anymore. The pulse was relatively long around 50 fs with an input energy of 500 μJ leading to an output pulse of 100 μJ in 20 fs. This scheme is impaired by the beam bell shape intensity distribution. It leads to a nonuniform broadening compounded with small-scale self-focusing making the pulse impossible to compress except for the top part of the beam that can be considered as constant limiting the efficiency and attractiveness of this technique. (See also sect. **6**˙1.)

2˙1. *Large energy pulse compression: Thin Film Compression (TFC).* – Here we are describing a novel scheme capable to compress 25 fs large energy pulses as high as 1 kJ to the 1–2 fs level. We call this technique Thin Film Compressor or TFC. See fig. 6. The incoming already short laser pulse (such as 25 fs) goes through a thin film of dielectric, which phase-modulates the laser pulse in broadening its spectrum. Once this optical nonlinearity makes the spectrum broaden, we can make the pulse compressed further by a pair of chirped mirrors to further compress the laser pulse, say, by a factor of two. If one tried this process three times, one could compress the pulse eventually by an order of magnitude. As shown in simulation this technique is very efficient $> 50\%$ and preserves the beam quality [37].

Unlike in the previous bulk compression technique performed with large-scale laser exhibiting bell-shape distribution, the technique relies on the top hat nature of large-scale femtosecond lasers when they are well constructed. Figure 7 shows the output of a PW laser generating 27 J in 27 fs called CETAL in the National Institute of Laser, Plasma and Radiophysics (NILPR) in Bucharest [52]. (Its recent application is mentioned in [53], see sect. **5**˙3.) Similar flat-top energy distributions are exhibited by the BELLA system at Lawrence Berkeley Laboratory. The next generation of high-power laser will deliver 10 PW like ELI-NP in Romania or Apollon in France, with a similar top hat beam. Simulation shows that the pulse being already very short, *i.e.* 27 fs, will require a very thin optical element of a fraction of a mm thick for a beam of 16 cm diameter. This element will be extremely difficult to manufacture, extremely fragile to manipulate and very expensive, making the idea of pulse compression of high-energy pulse unpractical. Our solution is to use a thin "plastic" film of $\sim 500\,\mu$m with a diameter of 20 cm. The element, that we call plastic for simplicity could be amorphous polymer thermoplastic, like the PVdC (polyvinylidene chloride), the additive PVC (polyvinyl chloride), the triacetate

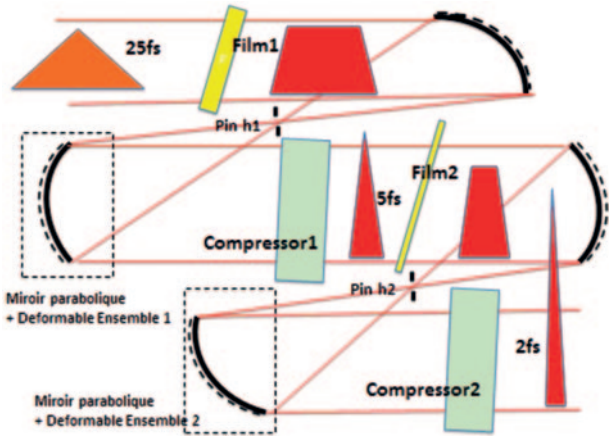

Fig. 6. – Embodiment of a double Thin Film Compressor TFC Thin film "plastic" of 500 μm thickness as uniform as possible is set in the near field of PW producing a flat-top beam with the B-integral value (B) of about 3–7. The beam propagates through a telescope composed of 2 parabolae, used to adjust finely the B and reduce the laser beam hot spots. Before compression the beam is corrected for its residual wavefront nonuniformity and the thin-film thickness variations. The pulse is compressed using chirped mirrors to 6.4 fs. The measurement is performed using a single-shot autocorrelator. The same step is repeated in a second compressor with a film of 100 μm producing an output of 2 fs, 20 J. (After [37].)

of cellulose, the polyester, or other elements as long as they are transparent to the wavelength under study, robust, flexible and exhibit a uniform thickness, ideally within a fraction of a wavelength. It is paramount to have a thickness as uniform as possible across the beam, but it does not have to be flat. As opposed to a thin (a fraction of a mm) quartz, silicate over a dimension of 20 cm, is abundant, inexpensive and sturdier. It should be susceptible to withstand the laser shot without breaking. In the case where the film breaks, it can be replaced cheaply and easily for the following shot. In the preferred embodiment shown in fig. 6, the laser beam is focused by an off-axis parabola with a f# about 10. The focused beam plays two roles: a) it can be used to adjust the beam intensity by sliding the film up and down (over a small travel though) in order to optimize intensity and b) to provide a means to eliminate the high spatial frequencies produced by the beam nonuniformities due to the small-scale focusing. A pinhole of suitable dimension is located at the focus. After the focal point the beam is re-imaged to infinity by a second parabola. The pulse can be measured at this point using a standard single-shot autocorrelator technique. Simulations, in the next section demonstrate the possibility to compress a 27 J, 27 fs into 6 fs in a first stage and 2 fs in a second stage where the plastic thickness is 100 μm. The beam remains of good quality after this double compression as shown in fig. 7.

Because there is no real loss in the system we expect an overall compressor efficiency in the range $> 50\%$. As a consequence the peak power is increased close to 10 times. Note that ideally, after each "thin film" a wave front corrector is installed to take into account a possible nonuniformity of the film thickness that could not affect the B value but would be harmful to the wave front. This simple technique provides a spectacular reduction in pulse duration of more than 10 times transforming a PW laser into a greater than 10 PW laser. It can also be extended to the 10 PW regime to boost its power to more than 100 PW or 0.1 EW.

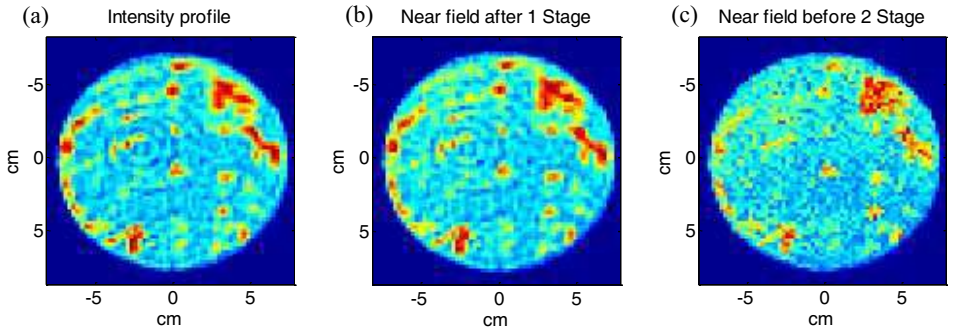

Fig. 7. – This figure shows the intensity across the beam profile: a) at the laser output, b) after the first stage (no spatial filter, c) after the second stage (no spatial filter) (after [37]).

2˙2. *Modelling of the two-stage Thin-Film-Compressor.* – Let us consider the physical model thoroughly. The main process which is responsible for spectrum broadening in solid materials is self-phase modulation. The self-phase modulation is a result of changing the refractive index at intense radiation:

$$n = n_0 + 1/2 \cdot n_2 \cdot |A|^2 = n_0 + \gamma \cdot I. \tag{2.1}$$

Here $A(t - z/u, z)$ is the complex amplitude of the electric field, I the intensity, n_0 the linear part of the refractive index, $\gamma[\mathrm{cm}^2/\mathrm{kW}] = (2 \cdot \pi/n_0)^2 \cdot \chi^3[\mathrm{esu}]$, χ^3 the nonlinear susceptibility. Typical values of γ for optical glasses are $(3\text{–}8) \cdot 10^{-7}\,\mathrm{cm}^2/\mathrm{GW}$ [54]. The other important phenomenon is linear dispersion —the dependence of refractive index on wavelength and the effect of self-steepening. The influence of the processes on pulse parameters can be described in the frame of quasi-optical approximation [55]:

$$\frac{\partial A}{\partial z} + \frac{1}{u}\frac{\partial A}{\partial t} - i\frac{k_2}{2}\frac{\partial^2 A}{\partial t^2} + i\gamma_1|A|^2 A + \frac{3\pi \cdot \chi^{(3)}}{n_0 \cdot c}\frac{\partial}{\partial t}(|A|^2 A) = 0. \tag{2.2}$$

Here, $\gamma_1 = (3\pi \cdot k_0 \cdot \chi^{(3)})/(2 \cdot n_0^2)$, u is the group velocity, c the speed of light, t the time, z the longitudinal coordinate, $k_2 = \frac{\partial^2 k}{\partial \omega^2}|_{\omega_0}$ the parameter of group velocity dispersion (GVD) and k_0 the wave vector. We use the equation with the initial condition on the boundary ($z = 0$): $A = A_0 \cdot \exp(-2\ln(2)t^2/T^2)$. Chirped mirrors are implemented after each nonlinear stage. The mirrors produce a correction of spectral phase and pulse shortening. In the simple case, it corrects only quadratic component of the phase:

$$A_c(t) = F\left(e^{-\frac{i\alpha\omega^2}{2}} F^{-1}(A_{\mathrm{out}}(t, L))\right). \tag{2.3}$$

Here A_{out} and A_c are the amplitudes of the pulse at the output of the nonlinear element and after the recompression, F and F^{-1} are the direct and inverse Fourier transform, α is the parameter of Group Velocity Dispersion of chirped mirrors.

In order to demonstrate the potential of Thin-Film Compressor, we use the following initial beam parameters: pulse duration $T = 27\,\mathrm{fs}$, energy 27 J, central wavelength 800 nm, flat-top transverse intensity distribution with diameter 160 mm. The thicknesses of the first and second nonlinear elements are 0.5 mm and 0.1 mm. The cubic nonlinearity

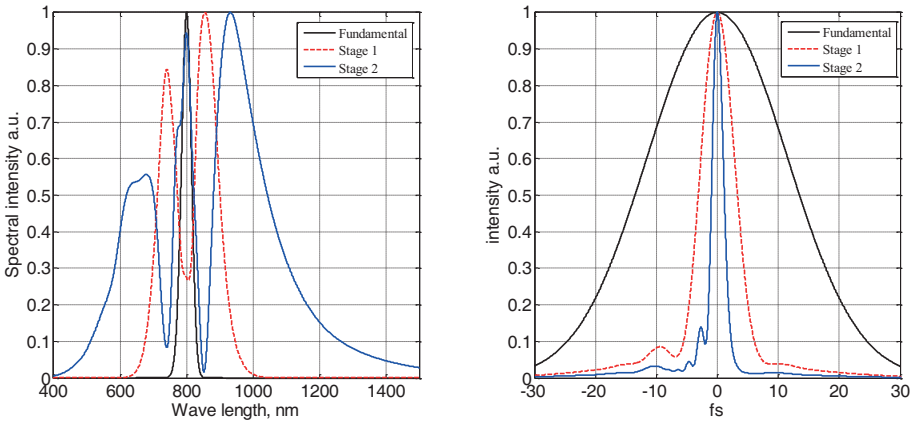

Fig. 8. – Successive spectra and pulse durations corresponding to the laser output, after the first stage and second stage. After the first stage the pulse length is 6.4 fs, and after the second stage the pulse is shrunk to 2.1 fs (after [37]).

parameter $\gamma = 3.35 \cdot 10^{-7}\,\mathrm{cm}^2/\mathrm{GW}$, $k_2 = 36.7\,\mathrm{fs}^2/\mathrm{mm}$. The fundamental peak intensity is $4.7\,\mathrm{TW/cm}^2$, after the first and second stages with temporal recompression procedure $16.6\,\mathrm{TW/cm}^2$ and $43\,\mathrm{TW/cm}^2$ at pulse durations 6.4 fs and 2.1 fs, respectively. The accumulated B integral values inside the first and second nonlinear elements are 6.1 and 4.4. The B integral values are permissible, and small-scale self-focusing can be suppressed in accordance with the technique presented in [56]. The results of numerical simulations (the spectral and temporal intensity profiles) are presented on fig. 8.

The proposed technique gives the opportunity to compress initially Fourier-transform–limited pulses and increase the peak power by one order of magnitude with the help of only passive optical components. Moreover, the numerical simulations demonstrate the Thin-Film Compressor does not change the transversal intensity distribution significantly. Also, it is necessary to underline the main advantage of the compressor —the possibility to implement it for high-energy and super power laser systems.

A similar phase modulation approach using a thin film has been adopted in achieving a subcyclic pulse in the optical laser regime [57]. This technique is probably not intended for intense lasers but for attosecond science [58].

2˙3. *Relativistic compression.* – This result becomes extremely relevant to the so-called Relativistic λ^3 regime [43] where relativistic few cycle pulses are focused on one λ^2 area (fig. 9a). The relativistic mirror is not planar and rather deforms due to the indentation created by the focused Gaussian beam. As it moves relativistically in and out and sideways, the reflected beam is broadcasted in specific directions and provides an elegant way to isolate an individual pulse (fig. 9b). In the relativistic regime Naumova *et al.* [44] predict a pulse duration T —compressed by the relativistic mirror— scaling like $T = 600\ (\text{attosecond})/a_0$ fig. 10. Here a_0 is the normalized vector potential, which is unity at $10^{18}\,\mathrm{W/cm}^2$ and scales as the square root of the intensity. Similar results are predicted by the Pukhov' group [59]. For intensity of the order of $10^{22}\,\mathrm{W/cm}^2$ the compressed pulse could be of the order of only a few attoseconds or even zeptoseconds. Naumova *et al.* [43] have simulated the generation of thin sheets of electrons of few nm thickness, much shorter than the laser period. This offers the prospect for X and

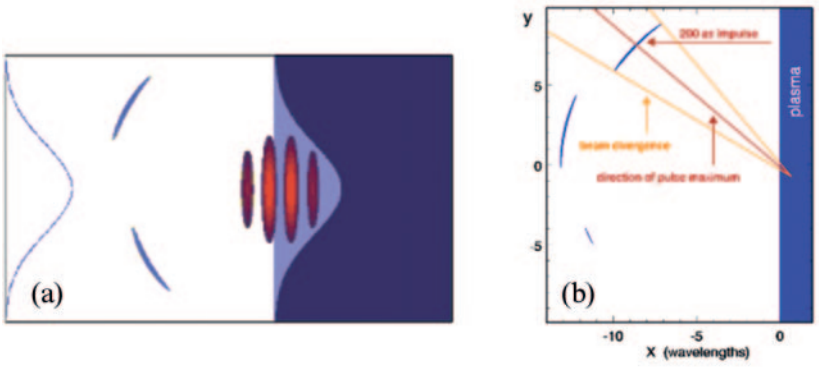

Fig. 9. – (a) Interaction of few cycle pulse in the relativistic λ regime. It shows the shaped mirror created by the enormous light pressure. In this time scale only the electrons have the time to move. The ions are too slow to follow. (b) The reflection of an ultra relativistic pulse by a high-Z target will broadcast the beam in a specific way. The pulse is compressed by a factor proportional to a_0. The pulses will be easily isolated (after [43]).

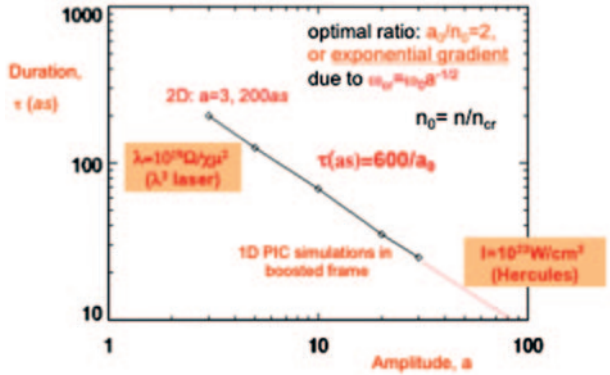

Fig. 10. – Pulse duration as function of a_0, the normalized vector potential. The expression of the pulse duration is derived to be 600 as/a_0. For a_0 of the order of 1000, pulse duration of 600 zs could be achieved (after [43]).

gamma coherent scattering with good efficiency. A similar concept called "relativistic flying mirror" has been demonstrated [25, 60], using a thin sheet of accelerated electrons. Reflection from this relativistic mirror will lead to high efficiency, pulse compression.

2˙4. *Physics of a vacuum nonlinearity and pulse compression in the vacuum.* – As the pulse is compressed into extremely short duration, a modest efficiency could produce sizable nonlinearities in a vacuum, although the value of n_2 is 18 orders of magnitude smaller than a typical optical transparent medium like glass. The critical power is inversely proportional to the square of the frequency and the vacuum critical power is 10^{24} W at 1.0 μm [6]. It should be 6 orders of magnitude less for one attosecond pulse, or 10^{18} W for 1 keV X-rays. Under this condition the vacuum critical power could be approached or attained with a single joule. For a 10 PW laser with 250 J input energy it

corresponds to only 0.4% efficiency. It is quite fascinating to imagine that filaments could be generated in vacuum analogous to those produced in air [61]. Their sizes would be limited by "vacuum breakdown" or pair creation as the intensity approaches $10^{29}\,\mathrm{W/cm^2}$ corresponding to a filament of 10^{-5} cm diameter.

In conclusions modern high-peak-power laser producing PW and 10 PW pulses with top hat distribution, combined with Thin Film Compressor will be capable to produce 100 PW with single femtosecond duration in the form of ultrarelativistic λ^3 pulses. It is predicted that their interaction with solid will generate attosecond or even zeptosecond multi exawatt pulses.

3. – LWFA scaling

The basic principle and more in-depth studies have accumulated [3,62,63]. Meanwhile, a large body of works toward its experimental realization has been performed. We list here some of the major milestones toward the realization of LWFA. An indirect observation of laser wakefield excitation was carried out through the observation of THz radiation by [64, 65] that conducted an experiment to form a plasma channel.

Nakajima and his colleagues carried out the ultrahigh gradient electron acceleration from Self-Modulated (SM) LWFA [66, 67]. This was the first experimental realization of laser wakefield acceleration of electrons. The observation of SMLWFA electrons around 40 MeV was reported by Modena *et al.* [68]. Direct observation of laser wakefields in ultrafast time scales was conducted [69, 70]. Later Dewa *et al.* [71] observed 100 MeV electrons from LWFA. In 2004 three simultaneous reports of first quasi-monoenergetic 100 MeV level electron acceleration by LWFA were ensued [72-74]. The guiding of relativistic laser in preformed channel was demonstrated by Geddes *et al.* [75]. Leemans *et al.* reported the first 1 GeV level electron acceleration by LWFA [76]. Optical injection of electrons to LWFA was carried out by Faure *et al.* [77]. Matlis *et al.* have done the first direct visualization of LWFA [78]. The stable self-guided LWFA at 1 GeV level was demonstrated by Hafz *et al.* [79]. Schmid, *et al.* carried out stable injection of electrons into LWFA by density jump for more control of the injection process. Buck *et al.* [80] did on-line measurement of the magnetic signal of LWFA. The first demonstration of multistage LWFA was achieved by Liu *et al.* and Pollock *et al.* [81, 82]. To meet the future collider applications and other higher-fluence LWFA applications, Mourou *et al.* [40] developed a new high-rep-rated high-efficiency laser based on fiber technology. The first 3 GeV level acceleration with LWFA was reported by Kim *et al.* [83]. Further extension of energies is duly expected from around the world labs.

These many works represent a series of rock-solid effort of the laser acceleration community that carried out the establishment of realization of LWFA and its rapid energy exponentiation with the energy increment rivaling that of the semiconductor leap of Moore's law. Here, we leave introductory discussions for the above references and rather do not repeat those and concentrate only on the discussion of how to scale up its energy gain.

3˙1. *State-of-the-art of electron laser plasma accelerators.* – One way for us to look for implementing acceleration of 100 GeV electron beams by means of LWFA is to adopt a multi-PW laser. In 1979, Tajima and Dawson [3] proposed harnessing electric fields of high-amplitude plasma density waves driven by intense laser pulses. They showed that for nearly 100% density modulation, acceleration gradients of electric fields due to the

charge separation can exceed 100 GV/m for plasma densities around $10^{18}\,\mathrm{cm}^{-3}$. Recently there is a growing interest in rapid progress on laser-driven plasma-based accelerators by exploiting petawatt-class lasers, whereby high-quality electron beams can be accelerated to multi-GeV energies in a centimeter-scale plasma thanks to laser wakefield acceleration mechanism, as reported so far, *e.g.* 1.8 GeV driven by 130 TW at SIOM [84], 2 GeV driven by 620 TW at TEXAS [85], 3 GeV driven by 210 TW at GIST [83], and 4.2 GeV driven by 230 TW at LBNL-BELLA [86]. Endeavors to accelerate further high-energy electron beams beyond 10 GeV are underway worldwide at large-scale laser and particle accelerator facilities. The BELLA (Berkeley Lab Laser Accelerator) project [87] at LBNL is aimed at developing 10 GeV laser wakefield accelerators for high-quality electron beam production in the conventional accelerator paradigm, *i.e.*, staged accelerator comprising an injector and accelerator driven by 1.5 PW laser at 1 Hz. The FACET (Facility for Accelerator science and Experimental Test Beams) project [88] at SLAC is aimed at accelerating 40 GeV electron beams by plasma wakefield acceleration driven by 20 GeV high-current electron bunches delivered from 2 km SLAC linac. The AWAKE (Proton-driven Plasma Wakefield Accelerator) project [89] at CERN is planned for producing $\sim$ GeV-level energy gain of externally injected electron beams by means of plasma wakefield generated by 450 GeV self-modulated proton bunches from CERN-SPS proton synchrotron.

To date most of the experiments on laser plasma accelerators have been carried out by employing ultrashort pulse lasers with duration $\tau_L = 30$–80 fs, focused onto a short-scale plasma target such as a mm-scale gas jet and a cm-scale plasma channel at plasma densities in the range of $n_e = 10^{18}$–$10^{19}\,\mathrm{cm}^{-3}$, where very large-amplitude plasma waves of the order of 100 GV/m are excited and trap energetic electrons to be efficiently accelerated in a wake to high energies of the order of 1 GeV. Here we overview the scaling-up the LWFA experiments on laser wakefield acceleration from the methodological point of view in optical guiding, characterized as self-guiding and channel guiding.

Self-guided laser wakefield accelerators: The self-guiding of relativistically intense ($a_0 \geq 1$) ultrashort ($c\tau_L \cong \lambda_p$) laser pulses in the blowout (bubble) regime has been investigated with three-dimensional particle-in-cell (3D PIC) simulations. When such a laser pulse with power $P > P_c$ enters an underdense plasma ($\omega_p < \omega_L$), the plasma electrons at the head of the pulse are completely blown out radially during the rise time of the pulse in the first plasma period, as shown in fig. 11 [90]. Most of the laser pulse resides inside the electron density depression and thereby can be guided. However, due to the inertia of the electrons, the density or refractive index channel forms on a longitudinal scale length of the order of a plasma skin depth c/ω_p. Hence, the very front of the laser pulse continuously erodes away due to diffraction so that the degree of guiding the remaining pulse is varying along the laser pulse. An estimate of the erosion rate is equated as c/ω_p per the Rayleigh length Z_R which would limit the distance over which such an ultrashort pulse can be self-guided to a few Rayleigh lengths. However, when the spot radius is matched to the bubble radius R_B so that $r_l \sim R_B \cong 2a_0^{\frac{1}{2}}/k_P$, in spite of diffractive erosion, self-guiding and wake excitation is possible over tens of Z_R in the bubble regime [91, 92]. The nonlinear pump depletion length is given by $L_{\mathrm{pd}} \cong (c\tau_L)\omega_0^2/\omega_p^2 = (c\tau_L)n_c/n_e$. Beyond the pump depletion limit, the pulse is so severely etched that it is no longer intense enough to excite a wake and thereby no longer guided.

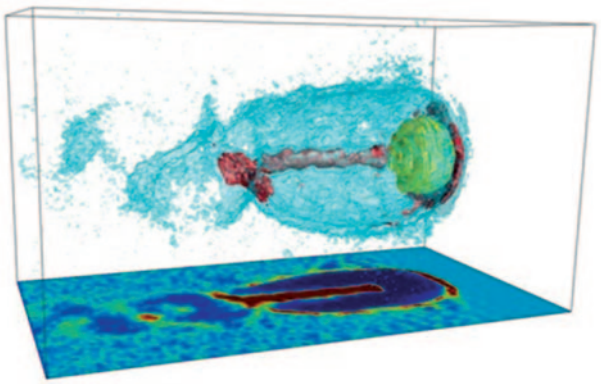

Fig. 11. – Electron density distribution of a laser wake in the bubble regime, computed with the 3D PIC simulation. From [90].

Channel-guided laser wakefield accelerators: For guiding intense laser pulses over many Rayleigh lengths without diffraction that limits the acceleration distance to a few mm in a uniform plasma, a preformed plasma density channel with a parabolic radial distribution has been developed. Plasma waveguides for guiding ultraintense short laser pulses in plasmas are produced by a number of methods, including laser-induced hydrodynamic expansion, pulsed discharges of an ablative capillary or a gas-filled capillary. However, the length of such a plasma channel has been limited to about 10 cm and the plasma density has been created for $n_e \geq 10^{17}\,\mathrm{cm}^{-3}$. Plasma density channels stabilize propagation of relativistically intense laser pulses under the matched condition, preventing laser-plasma nonlinear instabilities, such as filamentation and hosing that often occur in the self-guiding.

3˙2. *Scaling laws for Laser Wakefield Accelerators*. – Over the last two decades, a number of laser-plasma accelerator experiments have been carried out under various conditions. Comparing these data with theoretical laser wakefield acceleration models, it may be useful to find a correct scaling law capable of predicting energy gain, accelerated electron charge and the required laser-plasma conditions [93-97]. Since the maximum energy gain scales as $\Delta E_b \propto n_c \propto \lambda_L^{-2}$ for a given a_0, most of the previous experiments employ the chirped-pulse amplification lasers with wavelength $\lambda_L = 800\,\mathrm{nm}$ and pulse duration $\tau_L \leq 80\,\mathrm{fs}$, except for the case using a PW-class laser with wavelength $\lambda_L = 1057\,\mathrm{nm}$ and $\tau_L \sim 150\,\mathrm{fs}$. The validity of the energy scaling formulas based on the present analysis, may be verified by comparison with these experimental results. Figure 12 shows the comparison of measured electron beam energies with the energy scaling formulas in terms of a_0 and n_e as follows:

For electron beam acceleration up to the maximum beam energy E_b, a scaling formula for self-guided Laser Wakefield Accelerators is given by

$$E_b = \frac{2}{3} m_e c^2 a_0 \frac{n_c}{n_e} = 0.38[\mathrm{GeV}] a_0 \left(\frac{1\,\mu\mathrm{m}}{\lambda_L}\right)^2 \left(\frac{10^{18}\,\mathrm{cm}^{-3}}{n_e}\right), \tag{3.1}$$

where $a_0 \cong 0.855 \times 10^{-9} (I_L[\mathrm{W/cm}^2])^{1/2} \lambda_L[\mu\mathrm{m}]$, $n_c = \pi/(r_e \lambda_L^2)$, λ_L is the laser wave-

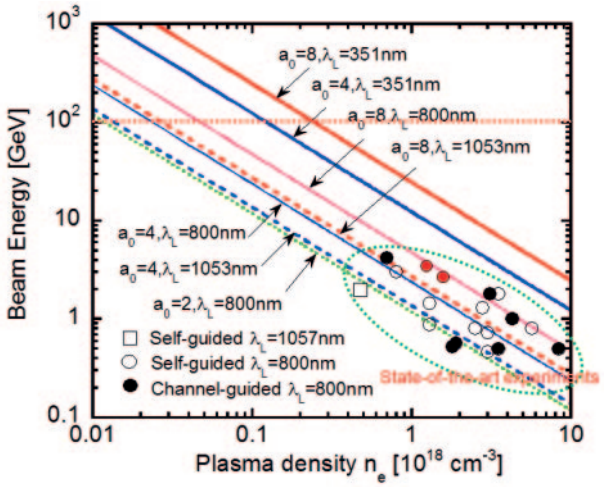

Fig. 12. – Beam energy scaling for self-guided LWFAs and the electron energy plots measured by GeV-class LWFA experiments.

length and n_e is the operating plasma density. The accelerator length $L_{\rm acc}$ reaching energy E_b is set to be a dephasing length, *i.e.*,

$$L_{\rm acc} = L_{\rm dp} = \frac{2}{3\pi}\sqrt{a_0\lambda_L}\left(\frac{n_c}{n_e}\right)^{3/2} = 7.9[\mathrm{mm}]\sqrt{a_0}\left(\frac{1\,\mu\mathrm{m}}{\lambda_L}\right)^2\left(\frac{10^{18}\,\mathrm{cm}^{-3}}{n_e}\right)^{3/2}, \tag{3.2}$$

Since the self-guided (pump depletion) length is given by $L_{\rm pd} \approx c\tau_L(n_c/n_e)$, the required pulse duration for $L_{\rm pd} \geq L_{\rm dp}$ should be

$$\tau_L \geq \frac{2}{3\pi}\sqrt{a_0}\frac{\lambda_L}{c}\left(\frac{n_c}{n_e}\right)^{1/2} = 24[\mathrm{fs}]\sqrt{a_0}\left(\frac{10^{18}\,\mathrm{cm}^{-3}}{n_e}\right)^{1/2}. \tag{3.3}$$

The energy scaling is capable of predicting results of GeV-class laser wakefield acceleration experiments as shown in fig. 12.

It is obvious that the higher a_0, *i.e.*, focused laser intensity I_L and the shorter wavelength λ_L produce the higher energy gain, which scales as $\propto a_0\lambda_L^{-2}$. For a given a_0, this is attributed to the longer self-guided length, correspondingly to the longer dephasing length due to an increase of the critical density at the shorter wavelength. As a result, the operating plasma density at 351 nm can be increased up to $n_e = 1.2\times10^{17}\,\mathrm{cm}^{-3}$ for $a_0 = 4$ and $n_e = 2.4\times10^{17}\,\mathrm{cm}^{-3}$ for $a_0 = 8$, respectively, compared to $n_e = 1.4\times10^{16}\,\mathrm{cm}^{-3}$ for $a_0 = 4$ at 1053 nm. This increase indicates decreasing the threshold of electron self-injection into laser wakefields as well as a decrease of the critical power for self-guiding.

3˙3. *Design for Laser Wakefield Accelerators.* – For a given energy E_b GeV and charge Q_b pC, the parameters of self-guided laser wakefield accelerators can be designed as follows. First, the field reduction factor α_c due to the beam loading is obtained by solving the equation

$$\alpha_c^2 + C\alpha_c^{3/2} - 1 = 0, \tag{3.4}$$

where the coefficient C is given by $C = (Q_b/123)\kappa_c^{1/2}\lambda_L^{-1}E_b^{-1/2}(k_p\sigma_p)^{-2}$. Then, the operating plasma density is determined from eq. (3.1), taking into account relativistic correction κ_c of the group velocity of the laser pulse at wavelength $\lambda_L\,\mu$m, as

$$n_e[\mathrm{cm}^{-3}] \approx 3.8 \times 10^{17}\kappa_c a_0 \lambda_L^{-2}(E_b/\alpha_c)^{-1}, \tag{3.5}$$

where a correction factor of the group velocity is defined as

$$\kappa_c = (a_0^2/8)\Big/\left[\sqrt{1+a_0^2/2} - 1 - \ln\left(\sqrt{1+a_0^2/2}+1\right) + \ln 2\right]. \tag{3.6}$$

The accelerator length equal to the dephasing length, *i.e.*, $L_{\mathrm{acc}} = L_{\mathrm{dp}}$, becomes

$$L_{\mathrm{acc}}[\mathrm{cm}] \approx 3.6 a_0^{-1}\kappa_c^{-1/2}\lambda_L(E_b/\alpha_c)^{3/2}, \tag{3.7}$$

while the pump depletion length due to pulse-front erosion is given by $L_{\mathrm{pd}} \approx c\tau_L n_c/n_e$. Since the dephasing length should be less than the pump depletion length, *i.e.*, $L_{\mathrm{pd}} \geq L_{\mathrm{dp}}$, the pulse length is set to be

$$\tau_L[\mathrm{fs}] \geq 38\kappa_c^{-1/2}\lambda_L(E_b/\alpha_c)^{1/2}. \tag{3.8}$$

The analyses of the wave equation with the standard paraxial form provide the matched spot radius r_L under the condition for the beam propagating with a constant spot size, *i.e.*, $R_m \equiv k_p r_L$, given by

$$R_m^2 = \ln(1+a_0^2/2)\Big/\left[\sqrt{1+a_0^2/2} - 1 - 2\ln\left(\sqrt{1+a_0^2/2}+1\right) + 2\ln 2\right]. \tag{3.9}$$

For the matched propagation of the laser pulse, the spot radius is set to be

$$r_L[\mu\mathrm{m}] \approx 8.7 R_m(a_0\kappa_c)^{-1}\lambda_L(E_b/\alpha_c)^{1/2}. \tag{3.10}$$

The corresponding matched power P_L is given by $P_L = (k_p^2 r_0^2 a_0^2/32)P_c$, where $P_c = 17 n_c/n_e$ [GW] is the critical power for the relativistic self-focusing at the plasma density n_e. Thus, the matched peak power is calculated as

$$P_L[\mathrm{TW}] \approx 1.6 a_0\kappa_c^{-1}R_m^2(E_b/\alpha_c). \tag{3.11}$$

The required pulse energy is

$$U_L[\mathrm{J}] = P_L\tau_L \geq 0.06 a_0\kappa_c^{-1/2}R_m^2\lambda_L(E_b/\alpha_c)^{3/2}. \tag{3.12}$$

Figure 13 shows the diagrams of the design parameters at wavelength $\lambda_L = 351\,\mathrm{nm}$, operating plasma density n_e [$10^{15}\,\mathrm{cm}^{-3}$], accelerator length $L_{\mathrm{acc}} \cong L_{\mathrm{dp}}$ [m], required pulse duration τ_L [fs], matched spot radius r_L [μm], matched peak power P_L [PW] and required pulse energy U_L [kJ] as a function of energy gain E_b [GeV] for the self-guided bubble regime laser plasma accelerator with $a_0 = 2, 4, 8$, assuming the beam loading field reduction factor $\alpha_c = 0.9$ for all cases.

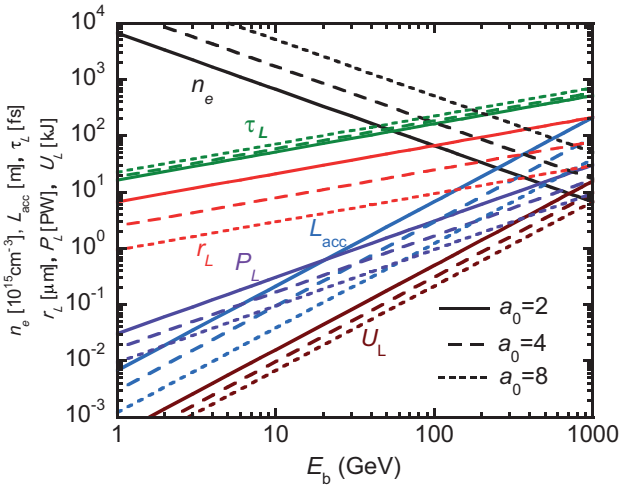

Fig. 13. – Parameters for the self-guided case in the bubble regime with $a_0 = 2$ (solid line), $a_0 = 4$ (dashed line), $a_0 = 8$ (dotted line), $\alpha_c = 0.9$ for $\lambda_L = 351\,\text{nm}$: operating plasma density n_e [$10^{15}\,\text{cm}^{-3}$], accelerator length $L_{\text{acc}} \cong L_{\text{dp}}$ [m], required pulse duration τ_L [fs], matched spot radius r_L [μm], matched peak power P_L [PW] and required pulse energy U_L [kJ], respectively, as a function of electron beam energy E_b [GeV].

Table I shows the design parameters of 40 and 100 GeV laser plasma accelerators in comparison with the results of 3D PIC simulations from the Lorentz-boosted frame OSIRIS code [98] at $\lambda_L = 800\,\text{nm}$. The design parameters for 40 GeV laser plasma accelerators are approximately in good agreement with the Lorentz-boosted frame PIC simulation.

TABLE I. – *Design parameters for the* 40 *and* 100 GeV *self-guided LWFAs in comparison with the results of 3D PIC simulations, the Lorentz-boosted frame OSIRIS code* [98].

Case	A	B	Ref. [98]	C	D	E	F
E_b [GeV]	40	40	38	100	100	100	100
n_e [$10^{15}\,\text{cm}^{-3}$]	3.2	17	2.2	1.2	6.7	17	51
L_{dp} [m]	4	1.7	5	12	6.7	3.0	1.2
λ_L [nm]	800	351	800	1053	351	351	351
a_0	2	2	2	3	2	4	8
r_0 [μm]	95	42	100	110	67	25	9.3
τ_L [fs]	224	103	160	500	163	185	225
P_L [PW]	1.2	1.2	1.4	2.1	3.0	1.7	0.95
U_L [kJ]	0.26	0.125	0.22	1.03	0.50	0.31	0.21
Q_b [pC]	127	56	300	250	89	78	64

3˙4. *Electron injectors*. – Electron beams can be produced and accelerated in the injector stage driven by the same laser pulse as that in the accelerator stage, relying on the self-injection mechanism such as an expanding bubble self-injection mechanism or the ionization-induced injection scheme in a short gas cell filled with a mixed gas. The injector comprising a gas jet or a variable length gas cell attached to the head of the accelerator stage will function as a thin plasma lens, where plasma density can be controlled separately from the accelerator stage.

To date, successfully demonstrated are several injection schemes that produce high-quality electron beams with small energy spread, low transverse emittance and high stability. For the large-scale LWFA experiment, the e-beam may be produced and accelerated in the injector stage by the same drive pulse as that in the accelerator stage, relying on the robust self-injection mechanism. Here we consider two possible self-injection schemes that are enhanced by expanding plasma bubble [99] or ionization-induced trapping [100].

Expanding bubble self-injection: A short dense plasma slab is produced from a gas jet located at the entrance of a long uniform plasma channel or neutral gas filled with much lower density in the accelerator. A laser pulse propagating on the dense plasma slab is self-focused into the accelerator plasma due to relativistic and ponderomotive focusing nonlinearities. Consequently the focused pulse produces blowout, then diffracts and drives an expanding bubble that traps electrons [99]. After diffraction stabilizes and self-guiding begins, the electron self-injection ceases as a result of the bubble transformed into a first nonbroken bucket of a nonlinear wake that is not fully evacuated. Hence a dense plasma slab is used as an optical element for focusing an intense laser pulse, rather than for self-injection of plasma electrons. Avoiding strong focusing and blowout inside the plasma slab limits its length defined by a thin lens approximation [99],

$$L_{\mathrm{lens}} < \frac{a_{\mathrm{lens}}^2 Z_R}{8}\left(\frac{P}{P_c}\right)^{-1/2}, \tag{3.13}$$

where $Z_R = \pi r_{\mathrm{lens}}^2/\lambda_L$ is the vacuum Rayleigh length corresponding to laser spot radius r_{lens} at the plasma lens. Since efficient focusing high-intensity pulses requires $P/P_c > 20$, this injector scheme is in favor of the LWFA in the bubble regime. The minimum focused spot radius r_{min} and focal length f_{lens} [101] are given by

$$r_{\mathrm{min}} = r_{\mathrm{lens}}\left(\frac{1-\delta^2}{1+(P/P_c-1)\delta^2}\right)^{1/2}, \tag{3.14}$$

and

$$f_{\mathrm{lens}} = L_{\mathrm{lens}}\frac{P/P_c}{1+(P/P_c-1)\delta^2}, \tag{3.15}$$

where $\delta = (L_{\mathrm{lens}}/Z_R)(P/P_c-1)^{1/2}$ is the normalized lens thickness. The lens plasma density is chosen so as to suppress Raman instabilities and energy depletion due to wakefield excitation. For case C, setting $a_{\mathrm{lens}} = a_0/2 = 1.5$ and $r_{\mathrm{lens}} = 2r_0 \approx 220\,\mu\mathrm{m}$ at the plasma lens with length $L_{\mathrm{lens}} \sim 1\,\mathrm{mm}$, one can design the lens plasma density $n_{e\mathrm{lens}} \approx 2.3\times10^{18}\,\mathrm{cm}^{-3}$ and the focal length $f_{\mathrm{lens}} \approx 6\,\mathrm{cm}$.

TABLE II. – *Plasma lens parameters for electron injection into* 100 GeV *accelerator stage.*

Case	C	D	E	F
$L_{\rm lens}$ [mm]	1	1	1	1
λ_L [nm]	1053	351	351	351
τ_L [fs]	500	163	185	225
a_0	3	2	4	8
$a_{\rm lens}$	1.5	1.34	1.	0.74
r_L [μm]	110	67	25	9.3
$r_{\rm lens}$ [μm]	220	100	100	100
$n_{e\rm lens}$ [$10^{15}\,{\rm cm}^{-3}$]	2.3	0.39	2.4	11.6
P/P_c	274.6	7.72	26.7	71.1
$f_{\rm lens}$ [mm]	60	7.7	24.6	44.0
G	18.5	5.85	16.1	43.1

The electron injection scenario is explained as follows: As a result of plasma lens focusing, the laser intensity increases at the focus position inside the accelerator plasma, where the radiation pressure expels all electrons outside the laser pulse and forms a dense electron sheath. As the laser diffracts after the nonlinear focus, the bubble expands rapidly enough and some of the sheath electrons lag behind the moving bubble boundary, staying inside the bubble. During the self-focusing process in the dense plasma slab, the strong relativistic laser-plasma interactions cause Raman forward scattering (RFS), of which the growth (number of e-foldings) for the most important three-wave RFS-side scattering [101] is given by

$$G = 2\sqrt{\frac{r_{\rm lens}}{r_{\rm min}}\omega_{p\rm lens}\tau_L} \approx 0.475\left[\frac{r_{\rm lens}}{r_{\rm min}}\left(\frac{\tau_L}{1\,{\rm fs}}\right)\left(\frac{n_{e\rm lens}}{10^{18}\,{\rm cm}^{-3}}\right)^{1/2}\right]^{1/2}. \tag{3.16}$$

For cases D, E and F at $\lambda_L = 351\,{\rm nm}$, provided that a laser pulse is focused onto spot radius at the plasma lens $r_{\rm lens} = 100\,\mu{\rm m}$, parameters for the plasma lens (gas jet) with length $L_{\rm lens} \sim 1\,{\rm mm}$ are calculated in table II.

Ionization-induced injection: According to theoretical considerations on the ionization-induced injection [100], for trapping electrons ionized at the peak of the laser electric field, the minimum laser intensity is given by

$$1 - \gamma_p^{-1} \leq 0.64 a_{0\,\rm min}^2, \tag{3.17}$$

where $\gamma_p = (n_c/n_e)^{1/2}$ is the Lorentz factor corresponding to the plasma-wave phase velocity $\beta_p = (1 - \omega_p^2/\omega_L^2)^{1/2}$. For case C (D) at $n_e \approx 1.2\ (6.7) \times 10^{16}\,{\rm cm}^{-3}$, the required minimum laser field is $a_{L\,\rm min} \geq 1.25\ (1.25)$. The maximum number of trapped electrons is saturated to be approximately $N_{e,\rm max} \sim 5\times10^6\,\mu{\rm m}^{-2}$ at the mixed gas length $L_{\rm mix} \approx 1000\lambda_L$ for the plasma density $n_e = 0.001 n_c$ with the nitrogen concentration $\alpha_{\rm N} = 1\%$ and the laser parameters $a_L = 2.0$ and $c\tau_L \approx 15\lambda_0$ due to the beam loading effects and initially trapped particle loss from the separatrix in phase space. From the

PIC-simulation results, the number of trapped electrons scales as

$$N_e[\mu\mathrm{m}^{-2}] \sim 8 \times 10^7 \alpha_N k_p L_{\mathrm{mix}} (n_e/n_c)^{1/2}, \tag{3.18}$$

for $\alpha_{\mathrm{N}} k_p L_{\mathrm{mix}} \leq 2$. The energy spread is also proportional to both the mixed gas length and the nitrogen concentration. For case C, setting $\alpha_{\mathrm{N}} \approx 1\%$ and $L_{\mathrm{mix}} \approx 10[\,\mathrm{nm}](n_e/10^{16}\,\mathrm{cm}^{-3})^{-1/2}/\alpha_{\mathrm{N}} \sim 9\ (4)\,\mathrm{mm}$, the number of electrons trapped inside the bunch with radius $r_b = 1/k_p \approx 53[\,\mathrm{nm}](n_e/10^{16}\,\mathrm{cm}^{-3})^{-1/2}$ is estimated as

$$N_b \sim N_e k_p^2 r_b^2/(4 r_e n_e) \sim 4 \times 10^9 (n_e/10^{16}\,\mathrm{cm}^{-3})^{-\frac{1}{2}} (\lambda_L[\mu\mathrm{m}])^2 \sim 4 \times 10^9 (2 \times 10^8), \tag{3.19}$$

which corresponds to charge $Q_b \sim 640\ (32)\,\mathrm{pC}$. This injector can produce the high-quality beam with the relative energy spread of less than 1%. Technically a gas jet with nozzle width of 9 (4) mm is attached at the upstream position from the entrance of the accelerator plasma, taking into account matching of the laser pulse to the plasma channel.

3˙5. *Plasma waveguides*. – The plasma accelerator comprises an injector stage relying on the aforementioned electron injection schemes and a plasma waveguide, where a propagating laser pulse excites wakefields to accelerate electron beams. For the self-guided LWFA, the injector stage is assembled from a 1 mm long gas jet for plasma lens and a 9 (4) mm long mixed gas cell attached to the accelerator stage comprising a variable length gas cell.

Density channels for guiding ultraintense ultrashort laser pulses in plasmas are produced by a number of methods, including laser-induced hydrodynamic expansion, pulsed discharges of an ablative capillary or a gas-filled capillary. However, the length of such a plasma channel has been limited to less than 10 cm and the plasma density has been created for $n_e \geq 10^{17}\,\mathrm{cm}^{-3}$. For a low-density ($n_e \sim 10^{14}$–$10^{17}\,\mathrm{cm}^{-3}$) large-scale ($\sim$ 1–10 m) plasma waveguide, a RF discharge plasma technique is proposed to create hollow electron density profiles by means of a quadrupole rod antenna. Possible advantages of the RF discharge technique are stability and a meter-scale length in addition to a long lifetime, high production efficiency and high repetition rate over those of laser-induced channels and capillary discharges. One of disadvantages that have not been resolved includes the use of high neutral-gas pressure for producing high-density plasma, where neutral gas remnants may change the density profile due to further ionization at the moment guided high-intensity laser pulses propagate in plasma channels. To guide ultraintense laser pulses, plasma channels must be produced in fully ionized gases with low atomic number Z such as hydrogen or helium.

Shock-driven plasma waveguide: Although presently no robust techniques are proper for production of low-density large-scale plasma channels, we consider a shock-driven plasma waveguide that is conceived by scaling up the laser-induced plasma channel technique called as "igniter-heater method" [102, 103]. In the igniter-heater method, using low-Z gases requires that channel producing laser pulses satisfy two conditions: 1) the igniter pulse is sufficiently intense to create free electrons through barrier suppression ionization (typically $> 2 \times 10^{14}\,\mathrm{W/cm}^2$ for a hydrogen gas); 2) the heater pulse is energetic and long ($> 100\,\mathrm{ps}$) but has relatively low intensity ($< 1 \times 10^{13}\,\mathrm{W/cm}^2$) to efficiently heat plasma through inverse Bremsstrahlung heating.

Here we design the igniter-heater method for the production of shock-driven plasma waveguides utilizing the PETAL laser, where a 3.6 kJ–500 fs output pulse is generated by the two-stage compression system composed of the first-stage air compressor and the second-stage segmented-beam vacuum compressor from 6.4 kJ–1.7 ns input pulse. The first stage compressor can output a 4.4 kJ–350 ps pulse. The igniter pulse is split out from a 500 fs drive pulse after the second compressor, while the heater pulse is split out from a 350 ps pulse on the optical pass between the first and the second compressors. After passing through the delay optics that make proper time delays between the igniter, heater and drive pulses, three pulses are recombined to propagate collinearly and focus on a long gas cell through the off-axis parabolic mirror. The required pulse energy can be estimated as follows.

For case C driven by a 1053 nm (1ω), 500 fs laser pulse, assuming that the igniter and heater pulses propagate a uniform hydrogen gas filled in the gas cell with the required on-axis plasma density $n_e \approx 1.2 \times 10^{16}\,\mathrm{cm}^{-3}$ without nonlinear focusing, the focused spot radius of which the vacuum Rayleigh length corresponds to the accelerator length $L_{\mathrm{acc}} \approx 12\,\mathrm{m}$ is $r_0 = (\lambda_L L_{\mathrm{acc}}/\pi)^{1/2} \approx 2.0\,\mathrm{mm}$ and the spot radius at $z = Z_R = L_{\mathrm{acc}}$ is $r_1 = r_L(1 + z^2/Z_R^2)^{1/2} \approx 2.8\,\mathrm{mm}$. Setting the intensity of the igniter pulse to be $I_{\mathrm{igniter}} \approx 2 \times 10^{14}\,\mathrm{W/cm}^2$, higher than the barrier suppression ionization threshold for hydrogen, $I_{\text{H-BSI}} \approx 1.4 \times 10^{14}\,\mathrm{W/cm}^2$ over the accelerator length requires the peak pulse power $P_{\mathrm{igniter}} = \pi I_{\mathrm{igniter}} r_1^2 \approx 50\,\mathrm{TW}$ and the pulse energy $U_{\mathrm{igniter}} = P_{\mathrm{igniter}}\tau_L \approx 25\,\mathrm{J}$. The heater pulse intensity $I_{\mathrm{igniter}} \approx 2 \times 10^{12}\,\mathrm{W/cm}^2$ requires the peak power $P_{\mathrm{heater}} = \pi I_{\mathrm{heater}} r_1^2 \approx 0.12\,\mathrm{TW}$ and the pulse energy $U_{\mathrm{heater}} = P_{\mathrm{heater}}\tau_{L\mathrm{heater}} \approx 42\,\mathrm{J}$.

For case E driven by a 351 nm (3ω), 185 fs laser pulse in the gas cell with the on-axis plasma density $n_e \approx 1.7 \times 10^{17}\,\mathrm{cm}^{-3}$ and the length $L_{\mathrm{acc}} \approx 3\,\mathrm{m}$, assuming that pulses at $\lambda_L = 351\,\mathrm{nm}$ (3ω) are used for the igniter and heater pulses, focused spot radius is $r_0 = (\lambda_L L_{\mathrm{acc}}/\pi)^{1/2} \approx 0.58\,\mathrm{mm}$ and the spot radius at $z = Z_R = L_{\mathrm{acc}}$ is $r_1 \approx 0.82\,\mathrm{mm}$. The igniter pulse requires $P_{\mathrm{igniter}} \approx 4.2\,\mathrm{TW}$ and $U_{\mathrm{igniter}} \approx 0.8\,\mathrm{J}$. The heater pulse requires $P_{\mathrm{heater}} \approx 0.01\,\mathrm{TW}$ and $U_{\mathrm{heater}} \approx 3.5\,\mathrm{J}$.

The plasma parameters of shock-driven plasma waveguides are estimated by the self-similar expansion model of a cylindrical blast wave, of which the shock wave velocity is given by [104, 105].

$$V_{\mathrm{shock}}(t) = \zeta_0 (E_{\mathrm{th}}/\rho_0)^{1/4} t^{-1/2}, \tag{3.20}$$

where E_{th} is the thermal energy per unit length initially driving the expansion, ρ_0 is the initial mass density, and $\zeta_0 \cong 0.55$ for an ideal gas, *i.e.*, the specific heat ratio $\gamma = 5/3$. Taking into account plasma heating due to the inverse bremsstrahlung, its absorption coefficient [106] is

$$\kappa_{IB} \cong 7.8 \times 10^{-9} Z n_e^2 \lambda_L^2 \ln\Lambda c^{-2} (k_B T)^{-3/2}, \tag{3.21}$$

where $k_B T$ is the plasma temperature in eV, $\ln\Lambda \sim 8$. In hydrogen plasma with $Z = 1$, $n_e \approx 1.2 \times 10^{16}\,\mathrm{cm}^{-3}$, $T \sim 10\,\mathrm{eV}$ and $\lambda_L = 1.053\,\mathrm{nm}$, the absorption coefficient is $\kappa_{IB} \sim 3.5 \times 10^{-6}\,\mathrm{cm}^{-1}$ and the energy deposited per unit length is $E_{\mathrm{th}} \sim \kappa_{IB} U_{\mathrm{heater}} \sim 0.15\,\mathrm{mJ/cm}$. With $\rho_0 \approx 1.66 \times 10^{-24} n_e \approx 2 \times 10^{-8}$ [g/cm^3], the shock velocity is

$$V_{\mathrm{shock}}(t) \sim 9.1 \times 10^6 (t/1\,\mathrm{ns})^{-1/2}\ [\mathrm{cm/s}], \tag{3.22}$$

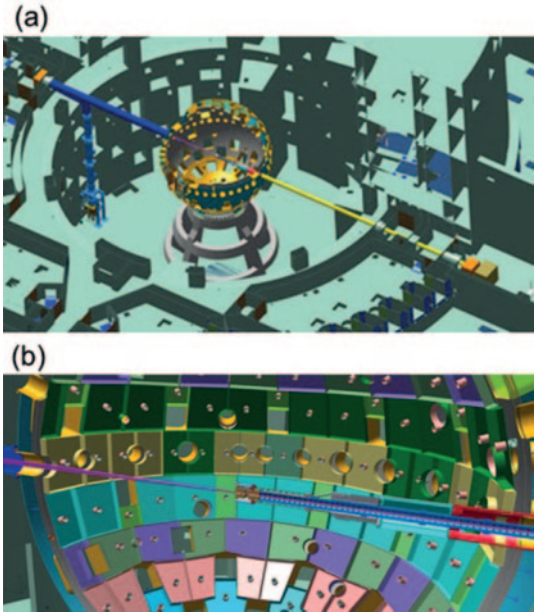

Fig. 14. – A setup design for 100 GeV ascent experiments at the PETAL laser facility. (a) Integrated configuration comprising a multi-PW laser (blue), 10 m diameter LMJ target chamber and laser plasma accelerator (yellow). (b) A cutaway view inside the target chamber, illustrating an electron injector focused by the laser, plasma waveguide and inserter to position and support the laser plasma accelerator.

and the shock radial position is calculated by

$$R_{\rm shock}(t) = \zeta_0 (E_{\rm th}/\rho_0)^{1/4} t^{1/2} \sim 182 (t/1\,{\rm ns})^{1/2}\ [\mu{\rm m}]. \tag{3.23}$$

For case C, the minimum time delay between the heater pulse and the guided drive pulse is given by setting $R_{\rm shock} \sim r_L \approx 110\,\mu$m as $\Delta t_{\text{heater-drive}} \sim 0.4$ ns that requires a delay line length $\Delta L_{\rm delay} \sim 12$ cm. The time delay between the igniter and the heater pulses is adjusted to $\Delta t_{\text{igniter-heater}} \sim 0.5$–1 ns ($\Delta L_{\rm delay} \sim 0.3$ m) during which the plasma density builds up to the maximum value. For case E, with $\kappa_{IB} \sim 7.8 \times 10^{-5}\,{\rm cm}^{-1}$, $E_{\rm th} \sim \kappa_{IB} U_{\rm heater} \sim 0.27\,{\rm mJ/cm}$, $\rho_0 \approx 2.8 \times 10^{-7}$ [g/cm^3], $V_{\rm shock}(t) \sim 5.5 \times 10^6 (t/1\,{\rm ns})^{-1/2}$ [cm/s], $R_{\rm shock}(t) \sim 110 (t/1\,{\rm ns})^{-1/2}$ [μm] $R_{\rm shock} \sim r_L \approx 25\,\mu$m, the minimum time delay between the heater pulse and the guided drive pulse is given as $\Delta t_{\text{heater-drive}} \sim 0.05$ ns that requires a delay line length $\Delta L_{\rm delay} \sim 1.5$ cm.

3˙6. *Possible design for 100 GeV ascent experiments.* – Here we present the possible designs of LWFAs for reaching 100 GeV, exploiting a large-scale laser facility such as the PETAL laser delivering 500 fs, 3.5 kJ pulses and the experimental facility at the Laser Mega Joule (LMJ). The 100 GeV ascent experiment is aimed at the production of 100 GeV electron beams by means of laser plasma accelerator driven by multi-PW laser pulses delivered from the PETAL laser in conjunction with full capabilities of the LMJ target chamber and equipment, including the diagnostics and inserter, as shown in fig. 14.

The objective of this experiment is to demonstrate acceleration of 100 GeV-level electron beams with substantial charge and high-quality properties. Firstly, the experiment is planned to validate 10 s GeV acceleration of electron beams injected by self-injection mechanism in nonlinear laser wakefield, followed by a meter-scale gas cell, which acts as an accelerating plasma medium, based on the modest scaling of laser wakefield acceleration by 1053 nm (1ω) laser pulses. Secondly, we explore energy gain enhancement due to UV drive laser pulses at the wavelength of 351 nm (3ω), which should be able to reach 100 GeV as a result of ~ 10 times higher energy gain than that of the 1ω laser driven LWFA. Thirdly, we will develop channel-guided LPAs using a long-range plasma waveguide produced by picosecond 1ω or 3ω pulses.

In conclusion, all the setup and parameters for achieving our objectives will be uniquely fitted to the LMJ/PETAL facility. The outcome provides us with in-depth insights to lead to the laser particle physics paradigm aiming at creating synergy between three advanced scientific fields: ultrahigh power lasers, relativistic plasma optics and particle acceleration to the TeV-PeV regime.

3˙7. *Prospective application toward High-Energy Frontier Colliders*. – A novel concept of laser acceleration exploiting super-high electromagnetic fields of lasers is motivated by a long-standing feeling that the state-of-the-art high-energy accelerators become too large and costly, and possibly they approach the end of the road, as emblematically reminded the demise of the Superconducting Super Collider (SSC) [2]. As a consequence, the application to high-energy frontier colliders may be one of the supreme goals for laser plasma accelerators, as illustrated with recently vibrant R&D projects such as BELLA [87], FACET [107] and AWAKE [89] to be aimed at laser-plasma–based colliders in the TeV-range energies. In the conventional paradigm of high-energy particle accelerators, an entire accelerator structure of electron-positron colliders with the center-of-mass energy of TeV will comprise multi-stage laser wakefield accelerators, each of which is operated in the quasi-linear wakefield regime rather than the nonlinear wakefield regime, *i.e.*, the bubble regime operated at high normalized laser fields of $a_0 > 4$ [93], taking into account the capability of accelerating both electrons and positrons in transverse focusing wakefield [108]. From the viewpoint of the critical requirements for the luminosity and operational power in the electron-positron collider, the operating plasma density n_e that is the most crucial parameter of laser plasma accelerators must be deliberately designed, based on the following considerations.

For the electron-positron linear collider, a critical requirement is the event rate that is determined by the product of collision cross-section $\sigma(e^-e^+ \to e^-e^+) \propto E_b^{-2}$ and luminosity

$$L = f_c N_b^2/(4\pi\sigma_x\sigma_y), \tag{3.24}$$

where f_c is the collision frequency, N_b is the number of particles per bunch, σ_x and σ_y are the horizontal and vertical rms beam sizes at the collision point, respectively. The luminosity requirement for future TeV range colliders is approximately scaled as $L[10^{34}\mathrm{cm}^{-2}\mathrm{s}^{-1}] \approx 4(E_b[\mathrm{TeV}])^2$ [108]. The required collision frequency is obtained as

$$f_c \cong 5[\mathrm{kHz}](\sigma_x\sigma_y/1\,\mathrm{nm}^2)(E_b/1\,\mathrm{TeV})^2(N_b/10^9)^{-2} \tag{3.25}$$

and the beam power is given by

$$P_b = f_c N_b E_b \approx 0.8[\mathrm{MW}](\sigma_x\sigma_y/1\,\mathrm{nm}^2)(E_b/1\,\mathrm{TeV})^3(N_b/10^9)^{-1}. \tag{3.26}$$

The number of particles per bunch is

$$N_b = Q_b/e \approx 1.49 \times 10^9 \eta_b (1-\eta_b)^{-1} (k_p \sigma_{x0})^2 (E_z/E_0)(n_e/10^{17}\,\mathrm{cm}^{-3})^{-1/2}, \tag{3.27}$$

where Q_b is a bunch charge, $\eta_b = 1 - (E_z/E_M)^2$ the beam loading efficiency that is an energy fraction of the plasma wave with the beam loaded field E_z and the maximum electric field E_M absorbed by particles of the bunch with a radius $r_b = \sqrt{2}\sigma_{x0}$, and $E_0 = m_e c\omega_p/e \cong 96[\mathrm{GV/m}](n_e/10^{18}\,\mathrm{cm}^{-3})^{-1/2}$ the nonrelativistic wavebreaking amplitude of the plasma wave. Thus the required beam power is calculated as

$$P_b \approx 0.54[\mathrm{MW}](1-\eta_b)\eta_b^{-1}(k_p\sigma_{x0})^2(E_z/E_0)^{-1}(\sigma_x\sigma_y/1\,\mathrm{nm}^2)(E_b/1\,\mathrm{TeV})^3(n_e/10^{17}\,\mathrm{cm}^{-3})^{1/2}. \tag{3.28}$$

The average laser power per stage is $P_{\mathrm{avg}} = f_c U_L$ and the total wall-plug power for the collider is $P_{\mathrm{wall}} = 2N_{\mathrm{stage}}P_{\mathrm{avg}}/\eta_L = 2f_c U_L N_{\mathrm{stage}}/\eta_L$, where U_L is the laser energy per stage, η_L the efficiency from the wall-plug to the laser, and N_{stage} the number of stages per beam. For a typical quasi-linear wakefield driven by a laser pulse with $a_0 = 1.4$ and pulse length $k_p\sigma_L = \sqrt{2}$, the average laser power per stage is given by

$$\begin{aligned} P_{\mathrm{avg}} \approx{}& 3.55[\mathrm{kW}](1-\eta_b)^2\eta_b^{-2}(k_p r_L)^2(k_p\sigma_{x0})^{-4}(E_z/E_0)^{-2}(\lambda_L/1\,\mu\mathrm{m})^{-2} \\ &\times(\sigma_x\sigma_y/1\,\mathrm{nm}^2)(E_b/1\,\mathrm{TeV})^2(n_e/10^{17}\,\mathrm{cm}^{-3})^{1/2}, \end{aligned} \tag{3.29}$$

where r_L is a laser spot radius and the wall-plug power yields

$$\begin{aligned} P_{\mathrm{wall}} \approx{}& 0.78[\mathrm{MW}]\eta_L^{-1}(1-\eta_b)^2\eta_b^{-2}(k_p r_L)^2(k_p\sigma_{x0})^{-4}(E_z/E_0)^{-3} \\ &\times(\sigma_x\sigma_y/1\,\mathrm{nm}^2)(E_b/1\,\mathrm{TeV})^3(n_e/10^{17}\,\mathrm{cm}^{-3})^{1/2}. \end{aligned} \tag{3.30}$$

Since the matched beam radius scales as $\sigma_{x0} \propto n_e^{-1/2}$, the number of particles per bunch scales as $N_b \propto n_e^{-1/2}$ and the average laser power per stage scales as $P_{\mathrm{avg}} \propto n_e^{-1/2}$, the wall plug power results in $P_{\mathrm{wall}} \propto n_e^{-1/2}$. The overall efficiency from the wall plug to the beam is given by

$$\eta_{\mathrm{overall}} = 2P_b/P_{\mathrm{wall}} \approx 1.4\eta_L\eta_b(1-\eta_b)^{-1}(\sigma_{x0}/r_L)^2(E_z/E_0)^2. \tag{3.31}$$

Considering constraint on the operational cost of the future linear colliders that limit the wall-plug power to a few 100 MW, the low operating plasma density in the range of 10^{15}–$10^{16}\,\mathrm{cm}^{-3}$ works in favor of the multi-TeV linear collider. Many of the underlying parameters for the design of laser plasma colliders scale with respect to the operating plasma density, as shown in table III [93].

Here we note that the necessity of high repetition, high fluence laser with high efficiency is evident. The International Committee for Ultra-Intense Lasers (ICUIL) and the International Committee for Future Accelerators (ICFA) collaboration inaugurated in 2008 has launched Joint Task Force (JTF) on Laser Acceleration. JTF concluded such need of laser technology [42]. Mourou *et al.* subsequently proposed a new laser technology Coherent Amplification Network (CAN) based on fiber laser [40]. This invention is expected to cover the weakness of the conventional intense laser technology (*i.e.* efficiency and the repetition rate) by improving the intensity of fiber laser that comes with high

TABLE III. – *Scaling dependence of LPA parameters on the operating plasma density.*

Accelerating field E_z	$\propto n_e^{1/2}$
Stage length L_{stage}	$\propto n_e^{-3/2}$
Energy gain per stage W_{stage}	$\propto n_e^{-1}$
Number of stages N_{stage}	$\propto n_e$
Total linac length L_{total}	$\propto n_e^{-1/2}$
Number of particles per bunch N_b	$\propto n_e^{-1/2}$
Laser pulse duration τ_L	$\propto n_e^{-1/2}$
Laser peak power P_L	$\propto n_e^{-1}$
Laser energy per stage U_L	$\propto n_e^{-3/2}$
Synchrotron radiation loss $\Delta\gamma$	$\propto n_e^{1/2}$
Radiative energy spread σ_γ/γ_f	$\propto n_e^{1/2}$
Initial normalized emittance ε_{n0}	$\propto n_e^{-1/2}$
Collision frequency f_c	$\propto n_e$
Beam power P_b	$\propto n_e^{1/2}$
Average laser power P_{avg}	$\propto n_e^{-1/2}$
Wall plug power P_{wall}	$\propto n_e^{1/2}$

efficiency and high repetition rate. Meanwhile, this invention introduced the coherent amplification technique by adding a large number of fiber laser bundles coherently after laser exits the fiber in order to overcome the shortcoming of the fiber laser, as it can carry only a limited intensity (or power) per fiber due to the fiber breakdown. We have been collaborating on this technology strategy with CERN.

4. – Toward high-energy acceleration with nonluminosity paradigms

One advantage of the newly emerging laser acceleration is its unique ability to reach extremely high energies that are far beyond in any other conventional methods, *e.g.* PeV. Fermi was the first to speculate the reach of PeV [109]. If reachable energies are so high that detectable events may be of interest even without the standard collider type of experiments (which may be based on LWFA such as [110], in which luminosity is one of the most important requirements, as discussed in sect. **3**), LWFA may contribute to distinct approaches with non luminosity paradigms. Such high energies are not easy even with laser acceleration, the exciting point is that with LWFA it is at least theoretically possible with existing technology or expected technology advancements such as the recent "short-cut" EW-zeptosecond path (for more discussion on this, see the development of the zeptosecond science in sect. **6**). If and when we do not need high-luminosity beam acceleration discussed in sect. **3**, one of the severest constraints in laser acceleration is lifted. If the physics is not based on collisions of particles, indeed the luminosity requirements for collider and high fluence are no longer requested. Though a huge majority of experimental particle physics relies on colliders, some physics can be studied without a collider. An example may be a study of the property of the vacuum, or the property of extremely high-energy γ-photon propagation in a vacuum. Some theories such

as superstring theory [111] expect granularity in a vacuum in extreme high energies due to the stringy nature of the vacuum texture, which could result in effective slowdown of the γ-photon speed. For such a measurement, luminosity does not matter, but the extreme high energy of photons and accuracy of measurement of the arrival time. Some speculated that astrophysical measurement of γ-photon arrival dispersion in the arrival times might be related to such an effect [112].

We will show an example of this [113] in sect. **4**˙1 by discussing the potential examination of the vacuum property that may be only explainable by such faraway theoretical paradigm as the string theory's implications. This includes the change of the speed of light as the energy of the photon (and thus the wavelength) becomes such that it is beginning to touch such string-theoretic minute scales. Also such an issue will arise in the discussion of the LWFA application to cosmic ray acceleration in sect. **7**.

Another possibility that has been pointed out is that of refs. [114,115], where under a certain theoretical expectation the physics in extremely high energies may show that the cross-section may begin to increase, rather than the customary decrease, as a function of the energy of the beam. This is explained briefly in sect. **4**˙3. (See ref. [114].)

4˙1. *Ballpark parameters of laser electron accelerator toward PeV*. – The scaling law dictates some three orders of magnitude density reduction from most current experimental parameters with the typical density at $10^{18}\,\mathrm{cm}^{-3}$ in order to carry out experiments in the range toward energies of PeV in a single stage. This in turn allows us to extend the laser pulse length by an order of magnitude, typically around the order of ps, instead of tens of fs. In a multi-stage approach, say 10^2–10^3 stages, in order to reach these energies, the density is higher and the pulse length shorter. The preferred laser technology of recent laser acceleration experiments has been that of Ti:sapphire because of its large frequency bandwidth, but for longer pulses a wider range of lasers becomes permissible. (In sect. **6**. we discuss an alternative path to go toward PeV.)

Here we take a few typical numerical examples for the PeV energy acceleration at various initial laser intensities based on the world's largest energy lasers such as NIF and LMJ [113], as we need not worry about rep rate and beam luminosity in such an experiment. We assume that the laser wavelength is $1\,\mu$m and the spot size of the laser is $w_0 \cup \lambda_p$ to make the operation in the 1D regime. We range the number of stages of laser wakefield acceleration. According to eq. (3.1), the required plasma density is calculated and thus other parameters including the laser intensity, or the normalized vector potential a_0, are automatically determined. The number of electrons is calculated based on the formula by Katsouleas *et al.* [116]. The total energy gain is given by just multiplying the single-stage energy gain by the number of stages. If we take the number of stages, $N_{\mathrm{stage}} = 1000$, we need $n_e = 1.8 \times 10^{17}$ to reach 1 PeV total energy gain. Under the current choice of ballpark we suggest that the optimum laser parameters are 4.1 MJ, 42 PW, and 0.098 ps [113]. The acceleration length per stage is $\sim 2\,$m and the total acceleration length is 2 km. The total acceleration length here means the sum of the individual stages without including the necessary matching sections, *i.e.* focusing optics of the electron beam and driving laser. The usual electromagnetic focusing system for electron beams may require substantially longer matching sections. However, it may be possible that the adoption of plasma lens lowers the length to an affordable size. In this choice the required laser pulse may strain the existing laser technology, as we shall discuss below. To ameliorate such a situation, the introduction of the nonuniform plasma density profile with a density initially lower than the value taken here might

bring in some room to maneuver: the laser pulse compression may take place through the nonlinear interaction with the plasma [117] to fit more adequately and gradually increase the density to the value considered here.

4˙2. *Possible experiment and its ramification in comparison with astrophysical data.* – Ellis *et al.* [112, 118] have suggested that the quantum-mechanical fluctuations with wavelengths on the order of quantum gravity origin may amount to the effective slowdown of the photon velocity, if the energy of the photon is high enough and its wavelength short enough to see such small scale lengths of fluctuations. These fluctuations may be directly tied with the length scale inverse of the Planck mass or may be even longer. There are other theories [119-122] that suggest that the photon velocity varies when its energy goes up. Of course, it is of immense importance to examine if such phenomenon appears at all and if such theories are correct (if any) or when such phenomenon begins to manifest. This is a fundamental test of the special theory of relativity and perhaps a prelude to a glimpse into quantum gravity. We envisage that such a test can be one of the candidate experiments that need not demand the high luminosity that a collider would. Thus we wish to consider this sample experiment in some more detail in this section.

At this moment, however, barring our PeV candidate experiment, all we can do is left to astrophysical observations to ask such questions. This is in part due to the fact that it is believed that if such a phenomenon exists at all, it should be so high an energy that is simply much beyond the reach of the present-day accelerator on Earth. On the other hand, we are learning a lot recently about the high-energy gamma ray emission from very fast flares from Active Galactic Nuclei [123, 124] and Gamma Ray Bursts (GRBs) which are known as brightest astrophysical objects [125, 126]. The energy dependence of light velocity has been tested using photon beams from such objects.

GRBs are categorized into two types, long one and short one. It is generally believed that long and short GRBs may be related to the supernova/hypernova collapse, and to the merger of two neutron stars (or some other very compact stars), respectively. In both GRBs there are two components in gamma rays. One is the component described with the band function which ranges between 30 keV and 10 MeV and can be described by two power-law spectra before and after the peak energy around 300 keV; the other is the extra delayed component ranging between 30 keV and 30 GeV (or beyond) and can be described with a simple power-law without a cut-off and break [125, 126]. These two components are believed to have different origins/to arise from different emission regions of GRBs.

Since GRBs are the brightest astrophysical objects and with a short characteristic time envelope, they can serve as an ideal searchlight to explore the deepest Universe. The primordial GRBs have been thus cherished to look for their time history of arrival to the Earth observatories over nearly an entire length of the Universe. If there is any energy dependence in the photon velocity, the larger energy photon would arrive later than the lower-energy ones from the given GRB. Many of the GRBs studies so far [125, 126], in fact, show this tendency. Furthermore, these tendencies seem consistent with each other; in other words, most of these observations show a similar arrival differential as a function of the energy of gammas. Except for the fact that it appears that the latest short GRB observed by the Fermi Observatory [127] might show a less differential time arrival, it shows too that the higher the energy of gammas, the later they arrive.

On the other hand, one may argue that the delayed arrival of higher-energy gammas is not due to the propagation property in the space between the GRB and the Earth, but rather the reflection of the genesis of GRBs and their mechanism of particle acceleration

to high energies at the time of the burst (*e.g.*, [128]). One might argue that the higher the electron energies are, the longer time it takes to get accelerated and thus the emission of gammas with higher energies should appear later. If this is the case, what we are observing is simply the property of GRB and its acceleration mechanism of high energy electrons in the GRB jet. It is not easy to dismiss such an argument when we wish to refer to the property of vacuum for the gamma ray propagation. We would be left to speculate which is more likely at this time.

Thus it would be scientifically valuable to be able to have a controlled terrestrial experiment that can determine the gamma speed as a function of its energy that is not depending upon the genesis of that gamma beam. This may become possible if our accelerated electron reaches as high energies as PeV. Consider the following experimental scenario. The energies of the highest-energy gammas from GRB are typically GeV, while the cosmic distance is on the order of 10^{28} cm. If we take the length of our vacuum tube to be about a km, the time differential we need to ascertain is on the order of sub fs, in order to meet or discriminate against the GRB observations of one second to tens of seconds. We understand that it takes ingenious experimental innovations unexplored so far to measure the arrival time of two gamma photons (or beams of photons) with two different energies, say PeV and 0.1 PeV with ultrafast accuracy. No one seems to have ever looked at PeV gamma arrival detection in such a time differential regime and this remains a challenge.

We have not started systematic experimental research of how to detect ultrahigh energy gamma particles and differentiate the arrival time with ultra-high time resolution. However, we venture at least some attempt into a possible detection technique development here. It has been pointed out by Narozhny some 40 years ago [129] (more recently [130]) that an ultrahigh energy gamma-particle can assist to break down the vacuum with substantially suppressed threshold electric field compared with the well-known Schwinger value. This is the nonlinear QED effect. The probability of the vacuum breakdown is derived as

$$P(E) \propto \exp\left[-\frac{8}{3}\left(\frac{E_s}{E}\right)\left(\frac{mc^2}{\hbar\omega}\right)\right], \tag{4.1}$$

where E_s the Schwinger field, $\hbar\omega$ is the gamma energy, E is the applied electric field in vacuum such as a laser. With a PeV gamma-ray particle, the exponent factor of (4.1) is reduced by the ratio of MeV to PeV ($mc^2/\hbar\omega$) over the expression of Schwinger's without the presence of a gamma particle. This means that the vacuum breakdown field plummets from the value of 10^{16} V/cm to 10^{10} V/cm.

We suggest that by employing time-synchronized somewhat intense laser field (at 10^{10} W/cm^2) at the "goal line" of the gamma-photon arrival, we cause sudden breakdown of vacuum and its avalanched particles of e^-e^+ as soon as one of the high-energy gamma particles arrives [131]. The PeV gamma particle facilitates to trigger the vacuum breakdown. The time scale of breakdown is far faster than fs. The exploitation of this phenomenon should allow an ultrafast signal of the PeV gamma-photon arrival. Since the trigger phenomenon is exponentially sensitive, we could play a game of adjusting the value of the laser field to see and differentiate different types of trigger phenomenology and parameters, depending upon the gamma particle energies.

We obviously need a lot more detailed experimental planning and developments of such an idea in the future. Further, the delay of gamma-photon arrival to the "goal line" due to the presence of low-density electrons is an important factor that determines the

"noise" to our "signal". One of the noises or uncertainties about the time differential may arise from residual gas electrons in our vacuum tube in which gamma particles travel. We may be able to evaluate this time delay as follows.

The dielectric refractive index $n_{\rm ind}$ of the plasma is given by

$$n_{\rm ind} = \left(1 - \frac{\omega_p^2}{\omega^2}\right)^{1/2}, \tag{4.2}$$

where $n_{\rm ind} = kc/\omega = c/v_{ph}$ sets the phase velocity of light and the group velocity

$$v_{gr} = c\left(1 - \frac{\omega_p^2}{\omega^2}\right)^{1/2}. \tag{4.3}$$

The difference between c and v_{gr} is

$$\frac{c - v_{gr}}{c} \cong \frac{1}{2}\frac{\omega_p^2}{\omega^2}. \tag{4.4}$$

This amount is extremely small for high-energy gamma particles with PeV energies. If the gas pressure of the "vacuum" is as low as 10^{-6} Pa, $(c - v_{gr})/c$ is as small as 10^{-44} for PeV gamma photons. On the other hand, the expected (if it ever arises or the margin we try to establish) deviation of the speed of light at extreme high energies ($\hbar\omega$) of PeV in our suggested experiment is as high as $\Delta c(\omega)/c \sim 10^{-10}$ [131]. Therefore, we seem not to be excluded from the possibility to test, feel, and detect the texture of vacuum that may arise from the quantum gravity effects and the subsequent phenomenon of the energy-dependent speed of light in such an experiment.

It is also noted that the precision of the arrival differentiation of PeV gamma-photons in the fs accuracy is not directly (and only indirectly) tied to the laser wakefield acceleration accuracy over multistage. This is because once we accelerate the electron bunches over many stages, only those electrons that fit in the specific phase space bucket are properly accelerated. We then use some of these electrons at the given phase to turn into gamma-photons by magnetic trigger. We can then possibly tag these gamma-photons at birth, which are to be propagated in vacuum over km. Note that the method of detection of PeV gamma-photons suggested in this section is sensitive to a single photon entering the "goal line".

4˙3. *Discussion and conclusions.* – We have presented the possibility that utilizing the existing large-energy lasers or their future extension, we can chart out a scientific path to reach for PeV energies by the laser acceleration. The laser wakefield acceleration (LWFA) is capable of very compact and intense acceleration far beyond the conventional accelerator approach. Reaching such energies as PeV appears only possible by such a new enabling method. We have then established a set of principles and associated parameters that allow us to reach for these energies. By adopting multi-MJ laser capability that exists in National Ignition Facility [132] (and soon completing Laser Mega Joule) and other future outgrowth of these lasers, we employ the (approximately) 1D and strongly nonlinear regime of LWFA to optimize the beam quality, the accelerating gradient, and other physical attributes. Based on this approach and the scalings known from the past

theoretical and experimental investigations, we are led to show that there exists a set (or sets) of parameters that allow us to envision a PeV accelerator.

These ideas and parameters are based on a fundamental principle of this acceleration method and not necessarily scrutinized for engineering details. Thus in the future we need to look for more in-depth studies and experimental investigations to ascertain the possibility for realizing such extreme energies using the LWFA. Nonetheless, it is very encouraging that already today's laser technology is at or near the ballpark of the necessary requirements as to the laser energy. No doubt that we need to learn plenty more on how to accomplish PeV acceleration using this method in the future.

Even though it appears to us not possible to make a PeV accelerator into a collider, because of its too severe requirements for luminosity, we wish to seek other applications at the energy frontier. We have suggested at least one such a candidate. If we use PeV electrons to produce PeV photons (gamma particles), these photons serve us to investigate new physics. We have suggested that with energy varying gamma particles, we can measure the arrival time differentiation of these gamma particles over some distance, say a km at or around PeV. According to some theories on quantum gravity and other alternative theories, the Lorentz transformation with respect to the speed (or the Lorentz factor γ) is no more invariant, but rather dependent on energies of the gamma photons. According to some of these theories, it is possible that when the energies of photons become as large as PeV, such effects may be magnified so much to become observable. This is precisely what we suggest here in this article.

So far it appears that the only way to test such possibilities and theories is through astrophysical observations. Thus astrophysicists have ventured to use primordial Gamma Ray Bursts (GRBs) to observe their arrival differential depending on their energies (frequencies). GRBs are the brightest objects in the Universe and thus we should be able to detect the most ancient and thus the farthest. In fact, the primordial GRBs can make us encompass the entire distance of the cosmos, thereby enabling us to magnify the time differential at maximum. Thereby, astrophysicists, amazingly, seem to have seen some time differentials of gamma particle arrivals from GRBs with statistical significant amounts. These indicate that, by and large, the more energetic gamma photons are, the later they are seen to arrive, in crude agreement with what these quantum gravity theories would predict. However, there remains a large body of discourses as to the nature of these time delays. For example, the time delays may be due to the GRBs source characteristics: the higher the gamma particle energy is, the longer it takes for these particles to get accelerated, wherefrom such time differential, but may not be due to the vacuum property of the photon propagation speeding over the Universe distance. Also there seems to be some statistical debates among various observations to date. These are the nature of the astrophysical observations and cannot be easily eradicated. It is thus ideal if we can come up with controlled experiments. This is what our PeV acceleration should be able to meet. It may be that this would pose the severest terrestrial test of Einstein's Special Theory of Relativity ever.

We have begun to explore an ultrafast optical detection method of the gamma particle arrival differential. This seems not to be out of the bound of physical reality. Although it provides so far only a crude principle to test such grandiose effects, to the first order it seems that we have not encountered fundamental difficulties. Of course, more details of such ideas and methods need to be studied. In addition, we could imagine more applications of PeV electrons (or other particles such as ions) at or near PeVs. We look for more investigations in this direction in the future. Finally, as to ion acceleration in this PeV LWFA, except for the first few GeV booster/injector, ion acceleration is not so

much different from electron acceleration in this linear accelerator. It might have some potential benefits for less stringent orbital requirements, such as the benefit of the lack of betatron radiations. If one has tangible experimental incentives for the PeV hadron sector physics, it would be of interest to pursue this avenue as well.

In addition to these, Caldwell *et al.* have suggested to explore QCD gluon dominant physics processes that tend to increase the cross-section as the beam energies get higher [114] to explore beyond the Standard Model physics. This possibility relies still on the collider approach, but exploits the possibility of rapidly increasing cross-section as energy goes up.

5. – Ion acceleration

In the Introduction (sect. **1**) we have motivated the needed conditions of laser-driven ion acceleration in contrast to the electron acceleration. The principal issue is to trap much heavier ions whose normalized vector potential of the laser fields (now normalized to ion mass) $a_{0i} = (M_i/m_e)\ a_0$ (with a_0 defined for electrons previously) is far smaller than a_0, so that ions are far more difficult to trap than electrons for a given laser fields. Thus we have to introduce the issue of catching ions adiabatically by changing the phase velocity of the accelerating waves from slow to gradually higher. To this purpose we refer the reader to fig. 2 in whose examples such a strategy is compared. One such approach proposed was to control the phase velocity of the waves (or pulse) of the accelerating structure as a function of the distance while ions are accelerated and gain their speed. We can do so, for example, by adopting the accelerating structure as Alfvén wave [29] in which one can gradually (adiabatically) vary either the plasma density from large to small, or the magnetic field from small to large, so that the Alfvén phase velocity increases adiabatically and thus the adiabatic ion acceleration may be achieved.

5˙1. *CAIL regime vs. TNSA.* – We consider the electrostatic sheath that is created behind the ponderomotive drive of the laser pulse and its dynamics in a self-consistent treatment to evaluate the maximal ion energies in the laser-driven foil interaction in which the foil dynamics also counts when the foil is sufficiently thin. When the foil is thick with $\xi \gg 1$, the foil is not moving and this is the in the regime of TNSA. (When the foil is thick and the laser pulse is completely reflected, the ion acceleration may be described by the plasma expansion model for thicker targets [33].) On the contrary, in case of $\xi \ll 1$, the transmission is dominant and the laser passes without too much interaction with the target. However, we will note that there is a regime ($\xi \gg 1$) with thickness still much smaller than that for TNSA for thicker targets. The optimum ion acceleration condition is, as discussed, in the range of $\xi \sim 1$ ($0.1 < \xi < 10$). Some experimental distinctions may be seen in fig. 15. There appears partially transmitted laser pulse, and behind the target energetic electrons still execute the collective motions in the laser field. Electrons quiver with the laser field and are also pushed forward by the ponderomotive force. In the region ahead of the exploding thin target, there are three components of characteristics orbits: a set of orbits in the forward direction (with angle 0°), the second backward (with −180° or 180°), and the third with loci with curved loops [32]. The first two are characteristics observed even in a simple sheath, but also present in the current case, where perhaps the forward one is as vigorous as or more vigorous than the backward one. The third category belongs to the orbits of trapped particles in the laser field or the ponderomotive potential. For a reflexing electron cloud the distribution shows only two components, the forward one and the backward one.

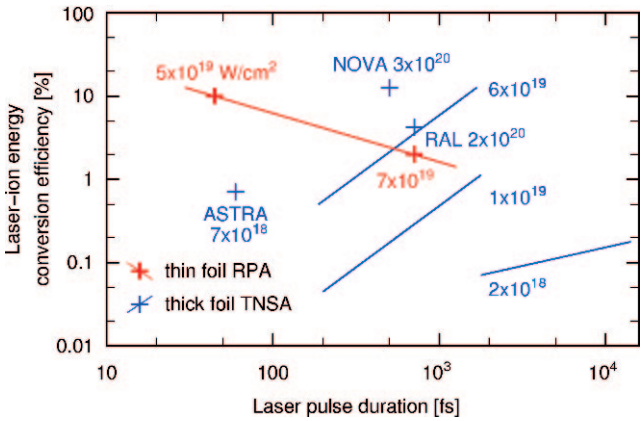

Fig. 15. – Comparison of the conversion efficiency of laser energy to ion energy from thick targets (TNSA mechanism, blue diamonds and lines) with that with ultrathin targets (CAIL, red diamonds and line). For the TNSA mechanism smooth curves from the fluid model by J. Fuchs [20] are shown together with some experimental points: ASTRA [138], NOVA [16], RAL [139]. (from ref. [31]).

In an ultra-thin target, the laser electromagnetic fields largely sustain the coherent motions of the electrons. As partially penetrated laser fields in addition to the laser fields in the target, the electron motion under laser fields is intact and is characterized by the transverse field. The electron energy consists of two contributions, the kinetic energy of (organized) electrons under laser and the ponderomotive potential of the partially penetrated laser fields that help sustain the electron forward momentum. Following the analysis of Mako and Tajima [14], the plasma density can be determined by

$$n_e = 2\int_0^{V_{\max}} g(V_x)\mathrm{d}V_x, \tag{5.1}$$

$$V_{\max} = c\sqrt{1 - m_e^2c^4/(E_0 + m_ec^2)^2}\,, \tag{5.2}$$

where g is the electron distribution function and E_0 is the maximum electron energy in this theoretical distribution and we call this the characteristic electron energy hereon.

The forward current density of electrons J and electron density n_e are related through

$$J(v) = -e\int_v^{V_{\max}} V_x g\,\mathrm{d}V_x, \tag{5.3}$$

$$n_e = \frac{2}{e}\int_0^{V_{\max}} \frac{\mathrm{d}J/\mathrm{d}v}{v}\mathrm{d}v. \tag{5.4}$$

At a given position in the reflexing electron cloud where the potential is ϕ, the total particle energy (disregarding the rest mass energy) is given by

$$E = (\gamma - 1)m_ec^2 - e\phi. \tag{5.5}$$

The current density can be determined from the 1D simulations results.

In the regime between the TNSA and the RPA [25] and its sisters [133-136] there sits a regime in which ion acceleration is more coherent with the electron dynamics than the TNSA but it is not totally synchronous as in the RPA. In this regime the acceleration of charged particles of ions produces a propensity to gain energies more than thermal effects would, as is the case for TNSA (and thus entailing the exponential energy spectrum) with heavier relative weight in the greater energy range in its energy spectrum characteristics. The power spectrum is one such example. On the other hand, in this regime the ponderomotive force and the induced electrostatic bucket behind it are not strong enough to trap ions, in contrast to the relativistic PRA. In RPA the laser's ponderomotive drive, the electrostatic bucket following it, and ions trapped in it are all moving in tandem along the laser. In the RPA the train of bow shock of electrons preceding the laser pulse and the following electrostatic bucket that can stably trap ions are stably formed. This structure is not so unlike the wave train of laser wakefield acceleration (LWFA) [3]. In LWFA since particles to be accelerated are electrons, it is when the amplitude of the laser becomes relativistic (*i.e.* $a_0 = eE_l/m\omega_0 c \sim O(1)$, about $10^{18}\,\mathrm{W/cm^2}$), that the electron dynamics is sufficiently relativistic so that trapping of electrons with the phase velocity c is possible and a process of coherent electron acceleration and thus a peaked energy spectrum is possible. For the ion acceleration for RPA wave structure, that is speeding at nearly $\sim c$, to trap ions in the electrostatic bucket, it is necessary for ions to become nearly relativistic, *i.e.* $a_0 \sim O(M/m)$, or $\sim 10^{23}\,\mathrm{W/cm^2}$. Otherwise, the phase velocity of the accelerating structure for ions has to be adiabatically (*i.e.* gradually) increased from small value to nearly c. Only an additional slight difference is that the LWFA excites an eigenmode of plasma, which is the plasma oscillations as a wake of the electrostatic charge separation caused behind the laser pulse, while the electrostatic bucket for the ion acceleration is not exciting eigenmodes of the plasma. Thus the more direct comparison of the RPA structure is the ponderomotive acceleration as discussed in [137]. In any case the spectrum of RPA can show (in its computer simulations such as in [25]) some isolated peak of the energy spectrum for the trapped ion bucket. Here we recall that in the experimental history of even the LWFA, till the so-called self-injection of electrons by the LWFA bucket's 3D structure was realized by short enough (and strong enough) laser pulse [72-74], the energy spectrum had not shown isolated peaked distribution.

In this section, we focus on the regime between the TNSA and RPA, having a power energy spectrum. In this sense the power-law spectrum is a symbol for this regime between TNSA and RPA. Here, it is instructive to pose the power-law dependence of the electron current as a function of the electron energy: The power-law dependence may be characterized by two parameters, the characteristic electron energy E_0 and the exponent of the power-law dependence on energy E:

$$J(E) = -J_0(1 - E/E_0)^{\alpha}. \tag{5.6}$$

The "coherence" index α here designates the steepness of the energy dependence on electrons and is a measure of coherence of the electron motion. In other words the greater α is, the more electrons in coherent motion are contributing to the overall current of electrons. Thus we may call α the coherence parameter of electrons. Usually the most energetic electrons are lost from the system and have minor contribution to the ion acceleration [35]. The maximum electrostatic potential is smaller than the laser ponderomotive potential or the characteristic electron energy E_0. In the high laser intensity case the relativistic electrons are dominant so that the integral is carried out with the

relativistic kinematics as

$$n_e = \frac{2}{e}\int_0^{V_{\max}} \frac{\mathrm{d}J(v)/\mathrm{d}v}{v}\mathrm{d}v = \frac{2}{ec}\int_{-e\phi}^{E_0} \frac{\mathrm{d}J(E)}{\mathrm{d}E}\mathrm{d}E \tag{5.7}$$
$$= -\frac{2J_0}{ec}(1 + e\phi/E_0)^{\alpha} = n_0(1 + e\phi/E_0)^{\alpha},$$

where n_0 is the initial plasma density and $J_0 = en_0c/2$.

5˙2. *Self-similar evolution of ion dynamics.* – The system's evolution needs to be tracked self-consistently with electrons, ions and the interacting electrostatic potential in time. These consist of a highly nonlinear coupled system of equations. We treat electrons as discussed in sect. **5˙1**, while we describe ions in nonrelativistic nonlinear equations in this section.

The nonrelativistic fluid equations are used to describe the response of the ions to the electrostatic field as follows:

$$\frac{\partial n_i}{\partial t} + \frac{\partial}{\partial x}(v_i n_i) = 0, \tag{5.8}$$

$$\frac{\partial v_i}{\partial t} + v_i\frac{\partial v_i}{\partial x} = -\frac{Qe}{M}\frac{\partial \phi}{\partial x}, \tag{5.9}$$

where the laser ponderomotive force for ions is neglected.

In order to solve the equations self-consistently, the self-similar condition is invoked by using the fluid equations and electron distribution with the self-similar parameter

$$\zeta = x/(v_0 t), \tag{5.10}$$

$$v_0 = (Qe\phi_0/M)^{1/2}, \tag{5.11}$$

$$e\phi_0 = E_0, \tag{5.12}$$

which is the characteristic electron energy. We introduce the dimensionless parameters:

$$U = v_i/v_0, \qquad \mathfrak{R} = n_i/n_0, \qquad \Psi = \phi/\phi_0. \tag{5.13}$$

Equation (5.8) and (5.9) now take the form

$$\mathfrak{R}'(U - \zeta) + \mathfrak{R}U' = 0, \tag{5.14}$$

$$U'(U - \zeta) + \frac{\mathrm{d}\Psi}{\mathrm{d}\mathfrak{R}}\mathfrak{R}' = 0, \tag{5.15}$$

$$\mathfrak{R} = (1 + \Psi)^{\alpha}, \tag{5.16}$$

In deriving eq. (5.16) the quasi-neutrality condition is imposed.

The conservation of energy is assessed with the boundary condition on the surface of the target:

$$U^2/2 + \Psi = 0 \quad \text{at } \zeta = 0. \tag{5.17}$$

The solutions to the set of eqs. (5.14)—(5.16) are

$$\mathfrak{R} = \left\{ \frac{\alpha}{(2\alpha+1)^2} \left(\zeta - \sqrt{2(2\alpha+1)} \right)^2 \right\}^{\alpha}, \tag{5.18}$$

$$U = \frac{2\alpha+2}{2\alpha+1}\zeta - \sqrt{\frac{2}{2\alpha+1}}, \tag{5.19}$$

$$\Psi = \frac{\alpha}{(2\alpha+1)^2} \left(\zeta - \sqrt{2\alpha+1} \right)^2 - 1. \tag{5.20}$$

Equations (5.18)–(5.20) also read in usual units as

$$n_i = n_0 \left\{ \frac{\alpha}{(2\alpha+1)^2} \left(\zeta - \sqrt{2(2\alpha+1)} \right)^2 \right\}^{\alpha}, \tag{5.21}$$

$$\upsilon_i = \left(\frac{QE_0}{M} \right)^{1/2} \left(\frac{2\alpha+2}{2\alpha+1}\zeta - \sqrt{\frac{2}{2\alpha+1}} \right), \tag{5.22}$$

$$\phi = \phi_0 \frac{\alpha}{(2\alpha+1)^2} \left(\zeta - \sqrt{2\alpha+1} \right)^2 - \phi_0. \tag{5.23}$$

The maximum energy is assessed when the ion density vanishes. This yields from eq. (5.18)-(5.19):

$$\varepsilon_{\max,i} = (2\alpha+1)QE_0. \tag{5.24}$$

In eq. (5.24) we see that the ion energy is greater if the coherence parameter of electrons is greater. Here E_0 takes the following form: $E_0 = mc^2(\sqrt{(1+a_0^2)} - 1)$ [31].

A more general expression for the time-dependent maximum kinetic energy at the ion front from eq. (5.22) is

$$\varepsilon_{\max,i}(t) = (2\alpha+1)QE_0((1+\omega t)^{1/2\alpha+1} - 1), \quad (t \leq 2\tau). \tag{5.25}$$

Here τ is the laser pulse duration and ω is the laser frequency. At the beginning the ion energy $\varepsilon_{\max,i}(0) = 0$ and the ion energy approaches infinity as long as the time $t \to \infty$. Normally as the maximum pulse duration of a CPA (Chirped Pulse Amplification) laser is less than picoseconds, the final ion energy from eq. (5.25) is only about $\varepsilon_{\max,i}(t = 1\,\mathrm{ps}) = 2(2\alpha+1)QE_0$.

The above theory of CAIL has been developed to analyze the experiment [30]. Along with this theory computational simulation has been also carried out [31,32]. These three are well agreeing with each other. See fig. 16. It is further noted that while the linearly polarized (LP) laser irradiation process is well described such as the maximum energies by the CAIL, when the polarization is switched to the circular polarization (CP), the energy spectrum of the accelerated ions show a quasi-monoenergetic feature [30]. This latter tendency is interpreted as the CP's ability to accelerate electrons and thus ions more adiabatically [30]. This insight indicates a potentially very important path toward improving the laser-driven ion acceleration. The more recent experiment by a Korean group also shows a similar tendency. They have adopted a far higher intensity of laser (up to $6\times10^{20}\,\mathrm{W/cm^2}$) than in [30] and also obtained much higher energies of accelerated ions [140] than in [30]. More importantly, their cut-off energy seems to agree with the

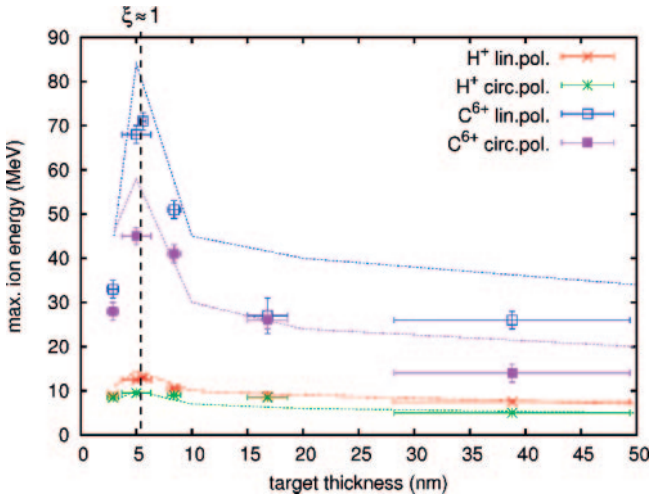

Fig. 16. – Maximum ion cut-off energies as a function of target thickness in the regime of CAIL experiments [30]. Theoretical curves are from the CAIL theory as discussed here [31,32]. Observed values and theory (CAIL) are in good agreement over a broad parameter range. (from ref. [31]).

CAIL. Also importantly, their results [140] show that the CP irradiation shows some preliminary evidence that its acceleration process is more adiabatic (accompanying a slightly isolated high-energy population, which does now show up in the LP case. This tendency, though still very preliminary, is consistent with the earlier finding of [30].

5˙3. *Single-Cycled Laser Acceleration of ions.* – The latest laser compression innovation as introduced in sect. **2˙1** allows us to access a new ion acceleration regime. In the method of Thin Film Compression, it is now possible to obtain a single-cycle (or nearly so) laser pulse. This method brings in two advantages over the longer pulse driven RPA [25]: i) as discussed in sect. **2**, the pulse intensity is enhanced, as the pulse length is reduced for a given energy laser (due to the high efficiency of TPC); ii) the elimination of compensatory oscillations enhances the efficiency, coherence, and stability of the ponderomotive acceleration. Due to these we find that the ion acceleration under the single-cycle laser pulse becomes far more robust, stable, and intense over the acceleration with multiply oscillatory longer pulse cases. We call this new regime as the Single-Cycled Laser Acceleration (SCLA) [53].

In the limit of single-cycled laser pulses, the electron acceleration becomes more direct and coherent as the ponderomotive acceleration term $\langle \boldsymbol{v} \times \boldsymbol{B} \rangle$ no longer needs averaging. In the case of multi-cycled laser pulses, the electron acceleration by the ponderomotive force must be averaged over the number of cycles. The former single-cycle situation introduces more coherent electron acceleration and sharper electron layer formation. This Single-Cycle Laser Acceleration (SCLA) regime permits a thinner optimal target thickness and leads to a more coherent ion layer following the accelerated electron layer. Our regime takes far smaller laser energy than that required in the known regimes mentioned above. In the present regime, when a single-cycle Gaussian pulse with intensity $10^{23}\,\mathrm{W/cm^2}$ is incident on a 50 nm planar CH foil, the ponderomotive force of the laser pulse pushes forward an isolated relativistic electron bunch and, in turn, the resultant longitudinal electrostatic field accelerates the protons. With a thin target, our

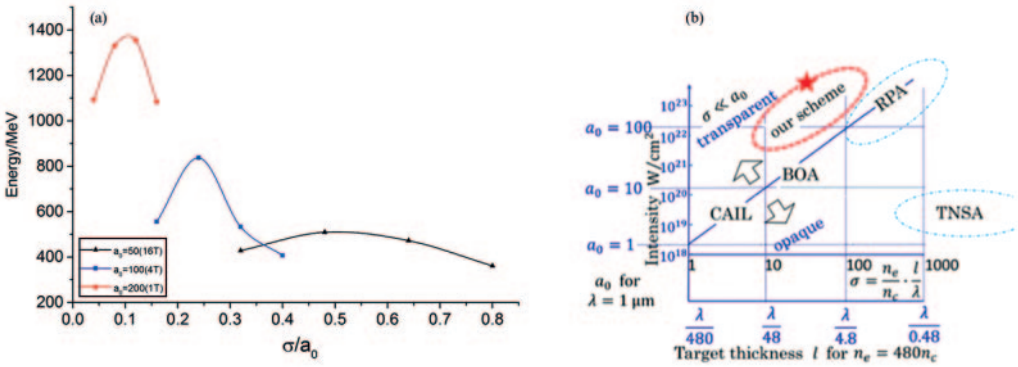

Fig. 17. – Proton cut-off energy. (a) The resulting proton energies with varying σ/a_0, the black line indicates laser pulse with $a_0 = 50$, and pulse duration $\tau = 16T$, the blue and red lines indicate laser pulses with $a_0 = 100$ ($\tau = 4T$), and $a_0 = 200$ ($\tau = 1T$), respectively; (b) identifies the location of the single-cycle regime within the laser ion acceleration map. After [53].

mechanism can coherently and stably accelerate ions over a significant distance without suffering from the typical transverse instabilities that arise under previously considered conditions. This uniquely stable acceleration structure is capable of maintaining a highly monoenergetic ultrashort ($\sim$ fs) GeV proton bunch.

In fig. 17(a), by keeping the total laser energy constant, we scan the normalized laser vector potential $a_0 = 50$; 100; and 200, and correspondingly the pulse duration $\tau = 16T$; $4T$; and $1T$ (black curve, blue curve, and red curve), respectively, where T is the laser oscillation period. In each curve, under the specific laser vector potential and pulse duration, we scan the foil thickness l to get the proton cut-off energy. Here, we take the normalized electron areal density $\sigma = n_e l/n_c\lambda$ as the target parameter reference.

From the three curves we see that with different pulse durations the acceleration efficiency of ions varies sharply. The shorter pulse duration (larger laser vector potential) yields the higher proton cut-off energy. For instance, the proton energy is increased by shortening the pulse duration from the $\tau = 16T$ (black curve) case to $\tau = 4T$ (blue curve) case. In particular, with the single-cycle pulse (red curve), the cut-off energy of the ions is increased by a significant amount. Another important new point we observe in fig. 17 is that under the single-cycle pulse condition, the optimal ratio between the normalized electron areal density and normalized laser vector potential σ/a_0 is about 0.1, which is much smaller than the optimal value of this ratio in the traditional RPA acceleration where ($\sigma_{\rm opt} \sim a_0$) [141] or ($\sigma_{\rm opt} \sim 0.4a_0 + 3$) [26] (as the black dashed line indicates in fig. 17(b)). We know that in an ideal RPA light sail regime, the resultant maximum ion energy is inversely proportional to the total mass of the accelerated target. In a simple picture, the optimum thickness is achieved by decreasing it, namely, the lower the total mass, the higher the final maximum energy. However, other physical processes, such as transverse instabilities, will strongly affect the actual acceleration process and prevent it from reaching the optimum acceleration, particularly with current state-of-the art multi-cycle ultra-intense laser pulses. While for shorter pulse durations, especially for single-cycle pulses, the duration is too short for those instabilities to develop and the constraints caused by instabilities are strongly suppressed, which gives us more opportunity to approach to the ideal case. So compared to the traditional RPA, the optimal target thickness becomes smaller in our regime.

To compare the SCLA regime to other laser-driven ion acceleration regimes, here in fig. 17(b), we give the simplified laser ion acceleration map, which is adapted from [53, 141]. The acceleration regimes we mentioned above are shown in the laser intensity I_0 (amplitude a_0), target thickness l (areal density σ) plane. The red dashed ellipse in fig. 17(b) identifies where the SCLA scheme lies within the laser ion acceleration map. Specifically, the scheme is located more in the transparent area ($\sigma \ll a_0$), which means smaller $\sigma_{\rm opt}$ value in the single-cycle acceleration, as we also indicated above.

By introducing SCLA here, we now see various attempts of laser acceleration of ions that have been considered historically summarized in fig. 17. The first experimentally realized laser ion acceleration was TNSA [16-18]. As discussed in sect. **1** and here in sect. **5**˙1, in this mechanism the target was thick, electrons penetrated through the thick target and ions were not adiabatically trapped and accelerated. Rather ions were accelerated on the surface of the fixed target over the sheath. See fig. 4(a). In order to increase the adiabaticity and thus prolong the time of acceleration of ions, one way was to reduce the mass of the target (see fig. 17), which is to reduce σ such as in CAIL [32] and BOA (Breakout Afterburner) [142]. This is far different from the TNSA regime, as seen in fig. 17(b). The Radiation Pressure Acceleration [25] was to increase a_0 and also somewhat decrease σ compared with TNSA. SCLA by the virtue of the decreased pulse length of the laser, also reduces σ and increases a_0. Thus the coherence of ion acceleration has increased in SCLA (and RPA) by increasing a_0 and decreasing σ away from TNSA.

6. – Zeptosecond science

The call for high intensity laser for the purpose of LWFA brought in the realization of such laser technology of CPA [6] by compressing the laser pulse by many orders without not necessarily increasing the need of increasing the laser energy:

$$I = E/(\tau A), \tag{6.1}$$

where I is the intensity, E is the laser energy, τ the laser pulse duration, and A is the laser focus area (which is limited by the diffraction limit of $\pi\lambda^2$ (with λ being the laser wavelength)). This is simply a metric (or geometric) relation and is not the same as eq. (4.2), which was discovered to represent the media's nonlinear response [46]. Thus LWFA and CPA have introduced high field science [39, 143] as a new scientific discipline, which sprang beyond these two elements of invention. Because of these revolutions, the laser that started as a tool of eV photons and thus as that of atomic physics has evolved into a tool of relativistic physics and higher energies [6]. In this section we survey some aspects of such evolution of laser science.

6˙1. *Pulse Duration-Intensity Conjecture toward zeptoseconds.* – If we want to go even shorter, we need to resort to even higher intensities and leave the nonlinear bound electron regime to go into the *relativistic* regime which is for 1 μm wavelength greater than 10^{18} W/cm^2. This type of intensity is today commonly available using Chirped Pulse Amplification [38] and also Optical Parametric Chirped-Pulse Amplification [144] systems.

In the relativistic regime electrons oscillating in the laser field become relativistic and change their "mass" during their oscillations by a factor proportional to the Lorentz factor γ, which in turn is also proportional to the normalized vector potential a_0. If a laser pulse can produce this intensity at the target surface, the enormous ponderomotive laser

pressure makes the electron critical surface oscillate in and out at relativistic velocity. As a consequence, the light impinged on this oscillating mirror is modulated periodically, resulting in high harmonics [60, 145]. Relativistic High Harmonic Generation gives the prospect of a much broader harmonic spectrum, higher efficiency with no cut-off defined by the plasma frequency [60,146]. This has been experimentally verified [43,44] using the long-pulse duration (300 fs) of the Vulcan laser and observing the 3200th harmonic order.

A related scheme was shown based on a few cycle pulse, focused on one λ^2 —this is the so called λ^3-regime [43, 44]— the relativistic mirror ceases to be planar and deforms due to the indentation created by the focused Gaussian beam. As it moves, PIC simulation shows, it simultaneously compresses the pulses but also broadcasts them in specific directions. This technique provides an elegant possibility to both compress but also isolate individual attosecond pulses. The predicted pulse duration scales like $T = 600$ (attosecond)$/a_0$. Here a_0 is again the normalized vector potential, which is about unity at $10^{18}\,\mathrm{W/cm^2}$ and scales as the square root of the intensity. For intensity of the order of $10^{22}\,\mathrm{W/cm^2}$ the compressed pulse could be of the order of only a few attoseconds. The same authors have simulated the generation of thin sheets of electrons with γ of few tens with attosecond duration [147] (and preceding idea such as the relativistic oscillating mirrors [60]). They could provide a way to produce by coherent Thomson scattering efficient beams of X-rays or even γ-rays. A similar concept called "relativistic flying mirror" has been advocated and demonstrated [131], using a thin sheet of accelerated electrons. Reflection from this relativistic mirror leads to a high efficiency and pulse compression.

When one wishes to go beyond coherent X-rays to gamma rays, the "mirror" that compresses the laser into gamma rays has to be of extremely high density ($\sim 10^{27}\,\mathrm{cm^{-3}}$) so that the laser may be coherently reflected into gamma photons. We suggest here that this may be achieved by a combination of the relativistically flying mirror just mentioned above with the implosion of this flying mirror so that its density may be enhanced by ten times in each dimension (thus thousand-fold in its density). We surmise that this may be achieved by a large energy pulse ($\sim$ MJ) at the ultra-relativistic (even ions become relativistically moving in the optical fields) intensity of $10^{24}\,\mathrm{W/cm^2}$ on a partial shell of a concave spherical target. This imploding ultrarelativistic flying mirror [147] is capable of coherently backscattering an injected 10 keV coherent X-ray pulse mentioned above [44], producing a possibility of coherent gamma rays of 100 ys duration.

We have learned that: matter exhibits nonlinearities when strong enough laser is irradiated; manifested nonlinearities vary depending on the strength of the "bending" field (and thus the intensity). The stronger we "bend" the constituent matter, the more rigid the "bending" force we need to exert; the more rigid the force is, the higher the restoring frequency (or the shorter the time scale) is. The nonlinearities of matter may vary, but this response is universal, ranging over molecular, atomic, plasma electronic and ionic, and even the stiffest of all vacuum, nonlinearities. Thus we have witnessed a sweep of nature's display of the universal behavior of direct correlation between the pulse shortness and the intensity of its driving laser over the widest intensity range our laboratory has to ever offer. See fig. 18 as it shows a clear trend of

$$\tau = fI^{-1}, \tag{6.2}$$

where f is the constancy of fluence ($\mathrm{J/cm^2}$) and is about unity from fig. 18, τ in s, I is the laser intensity in $\mathrm{W/cm^2}$. Once again, we emphasize that this equation, eq. (6.2), is not the same as eq. (6.1) [46].

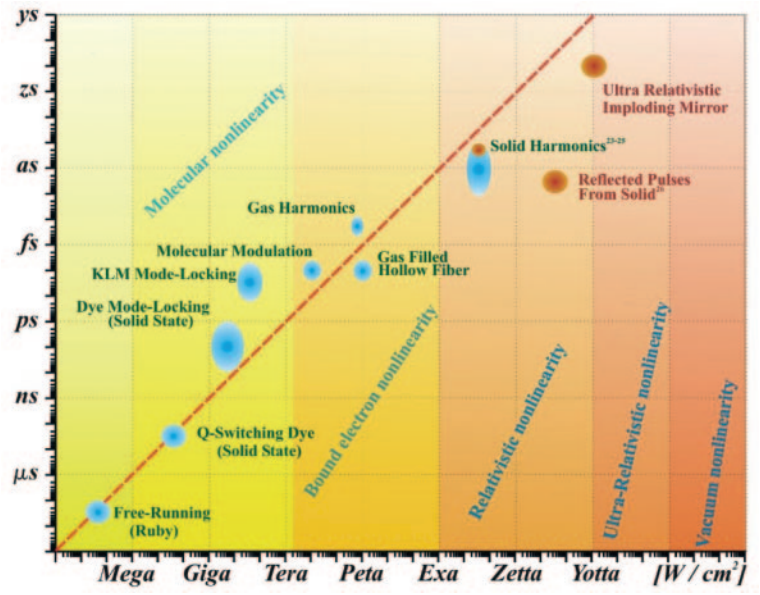

Fig. 18. – The Pulse Intensity-Duration Conjecture is shown. An inverse linear dependence exists between the pulse duration of coherent light emission and its intensity of the laser driver in the generation volume over 18 orders of magnitude. These entries encompass different underlying physical regimes, whose nonlinearities are arising from molecular, bound atomic electron, relativistic plasma, and ultra-relativistic, and further eventually from vacuum nature. The blue patches are from the experiments, while the red from the simulation or theory. From [46].

In conclusion evidences over more than 18 orders of magnitude of the Pulse Intensity-Duration Conjecture have been accumulated experimentally and with simulation. It shows that the pulse duration goes inversely with the intensity from the millisecond to the attosecond and zeptosecond, using values from experiments and simulation. Most notably it predicts that the shortest coherent pulse in the zeptosecond-yoctosecond regime should be produced by the largest laser, like ELI or NIF and the Megajoule, if they are reconfigurated [61] in femtosecond pulse systems. This conjecture may provide an invaluable guide for future ultra-intense and short-pulse experiments. It fosters the hope that zeptosecond and perhaps yoctosecond pulses could be produced using kJ-MJ systems. It opens up the possibility to take snapshots of nuclear reactions and to peek into the nuclear interior in the same way that Zewail [148] examined chemical reactions or Corkum and Krausz [58] probed atoms. The other exciting prospect is the possibility to study the nonlinear optical properties of vacuum. This conjecture ties the three distinct disciplines of science, *i.e.* ultrafast science, high field science, and large-energy laser science together with a single stroke.

6˙2. *Adoption of single-cycles X-ray pulse for LWFA.* – The recent invention of single-cycled optical laser compression through the TFC [37] (see sect. **2**) by combining with the relativistic mirror compression [43] allows us to create a single-cycled (coherent) X-ray laser pulse. We consider the utilization of such X-rays now. This new invention will further extend the reach of the above Duration-Intensity Conjecture [46] into higher intensity (EW and ZW) and shorter pulse (attoseconds and zeptoseconds). Such lasers as

well as the CAN laser [40] (mentioned in sect. **3**) can open up radically different vista for frontiers of science in ultrafast and ultraintense fields. As we discuss below, this development enables us to evolve from the LWFA in gas plasma with optical laser now realizable to the LWFA in solid density with X-ray laser [45, 263]. In addition such lasers (perhaps in combination with the high fluence laser of CAN [40]) also may possibly introduce new pathways to do fundamental physics research using unique intense, coherent, and ultrafast properties of photons. These include: the laser detection of dark matter (and even dark energy) [149, 150], and the laser detection of neutrino [151] with the discovery of a loophole in the Landau-Yang theorem.

Here we take advantage of the high frequency of the photons in order to drive wakefields in solid density matter, following [45]. In LWFA the higher the density of the medium (plasma) is the greater the acceleration gradient is. However, the higher the density for the fixed frequency of laser, the lower the energy gain by LWFA [3]. The high intensity LWFA energy gain is given by

$$\varepsilon_e = a_0^2 mc^2 (n_c/n_e), \tag{6.3}$$

where a_0 is the normalized vector potential of the laser electric field, n_c is the critical density of the plasma at the laser frequency, n_e the electron density [2].

In order to avoid this lowering of the energy by increasing density, the increase of the critical density helps. For 1 eV optical photons, n_c is about $10^{21}\,\mathrm{cm}^{-3}$, while for photons of 10 keV X-rays n_c is about $10^{29}\,\mathrm{cm}^{-3}$. Thus to use the X-rays as the driver of LWFA introduces the tremendous energy multiplication according to eq. (6.3). We now can afford to use the solid density electrons. We thus introduce the LWFA into a solid with this high-energy X-rays in [37]. The typical solid density of electrons is $10^{23}\,\mathrm{cm}^{-3}$. The accelerating length L_{ac} is

$$L_{\mathrm{acc}} \sim a_X (c/\omega_p)(\omega_X/\omega_p)^2, \tag{6.4}$$

where ω_X is the X-ray frequency, ω_p is the plasma frequency of the solid seen by the X-ray photons (which depends on the photon frequency and on how much the bind electrons may be regarded as the "plasma electrons" for the X-ray photons). Here a_X is the normalized vector potential of the X-rays, corresponding to the optical laser's a_0. The crystal LWFA energy gain is thus

$$\varepsilon_X = a_X^2 mc^2 (n_c/n_e), \tag{6.5}$$

if we do not focus the X-rays below the radius of the optical laser focal size, $a_X \sim a_0$ (ω_0/ω_X), where ω_0 is the optical photon frequency. However, as the diffraction limit of the X-ray focal size can be as small as the X-ray wavelength (which is possible in principle), the value of maximum possible a_X is not so small as the above value of $a_X \sim a_0\ (\omega_0/\omega_X)$, but the reduction of a_X is by a factor of (ω_0/ω_X) from a_0, while it remains as $a_X \sim a_0$ in the extreme optimal case of the X-ray focus. If we take as an example the focal size of the X-rays between these two extremes (1 μm and 0.1 nm), say the size of the focal size to be 10 nm, the focal intensity of the X-rays is approximately at the Schwinger intensity, if the X-rays generated by the mechanism of Naumova *et al.* [43] is taken. Here due to the Naumova's mechanism the optical laser renders severe surface grazing and compression that results in the compression of the single oscillating laser

pulse reflected off with single oscillation higher frequency coherent photon pulse with the pulse length given as

$$\tau_X \sim 600/a_0, \tag{6.6}$$

where τ_X is given in the unit of as (attosecond) [43]. In other words, the X-ray pulse power goes up by this compression of X-rays approximately by a factor of a_0^2 over that of the original optical laser power divided by the conversion efficiency of, say 0.1. If this is the case, the original nearly 200 J optical laser at 2 fs now becomes a coherent X-ray laser at 10 EW. In this example, the energy gain by the LWFA mechanism in the solid crystal of the electronic density (that is seen by the X-rays at 10 keV) of $10^{23}\,\mathrm{cm}^{-3}$ is from eq. (6.5) as $\varepsilon_X \sim$ (several to) 10 PeV and $L_{\mathrm{acc}} \sim 1$ m. The first PIC simulation of LWFA in the solid density employing nanomaterials (with nanoholes) has been investigated recently [152]. This work in fact reveals the above fundamental scalings of LWFA in the solid density regime, indicating the possibility of TeV/cm accelerating gradient, the favorable containment of the wakefield in the nanotube, and the avoidance of accelerated electrons colliding into solid electrons. It is important to note that many of these processes are ultrafast in the domain of attoseconds (or even in zeptoseconds) including the acceleration and radiation. These are much faster processes than the atomic processes in the solid (or nanomaterials). This means that the solid material damage time scales are far longer than the above LWFA physics time scales in the solid regime.

Reference [152] also indicates the more quantum-mechanical radiating processes such as QED influenced betatron radiation etc., which might eventually be influencing emittance reduction [153]. Here we assume that the electron energy loss by various mechanisms including Bremsstrahlung and betatron radiation by electrons can be negligible. In reality these radiations become very important [93, 154]. In addition, a host of other quantum-mechanical processes becomes important, such as the pair creation. Therefore, a more accurate assessment where the saturation of the electron acceleration arises, needs a thorough research in the future. However, it is known that the betatron radiation can contribute to the cooling of the transverse emittance and helps to potentially enhance the luminosity [154].

In order to overcome these potentially large electron (and positron) energy loss in the crystal, we suggest to adopt the nanohole (or even a narrower tube, as narrow as an ångstrom) in the crystal through which we conduct the transmission of electrons and positrons, while the X-rays, as in the above example indicated, propagate over a radial cross-section of typically 10 nm [45, 152]. However, if we can manage to focus X-rays onto even smaller radius, the corresponding value of a_X becomes greater than the value we used in the above estimate of $a_X \sim 10^2$ and thus the values of the gained energy and accelerating distance in eqs. (6.3) and (6.2) become much greater than the values we estimated above. Again here applies the caution that the radiation energy loss processes etc. may become substantially greater and may become central. If these processes may be restricted by the technique of the hollow crystal with nanohole (or 0.1 nm hole), it may not be impossible to look at truly astrophysical parameters of energy gains such as 10^{19} eV over 30 m.

It may be argued that at the Schwinger intensity (or even below that value) of the X-rays (or optical) lasers the pair creation process becomes so dominant that no field intensity above this value may be realizable. If this is the case, the enhanced energy gain beyond the value we estimated may not be surpassed. However, we suggest here

that this seeming ultimate limit of the laser field intensity at the Schwinger value may be lifted by noting the following. Because the Poincaré invariants $E^2 - B^2$ and $\boldsymbol{E} \cdot \boldsymbol{B}$ remain Lorentz invariant if there is only one EM wave in a plane 1D geometry, such a wave cannot break down the vacuum. Thus we may be able to conduct the transmission of the above Schwinger wave without much breakdown of the vacuum if we satisfy the above condition (or approximately that condition). The kind of estimate we mentioned above (in two paragraphs above) for the 10 nm focus, for example, may allow near 1D geometry so that the case under study may be close to such situation. If so, the field above Schwinger intensity is attainable, at least theoretically. Here we note that the self-focusing condition in a vacuum (for example, see [6]) is fulfilled if the power of the laser P exceeds the critical power defined by

$$P_{cr} = (45/14)cE_S^2\lambda^2\alpha^{-1}, \tag{6.7}$$

where $E_S = 2\pi m^2c^3/eh$ is the Schwinger field and α is the fine-structure constant. This value is as high as a few times 10^{24} W for optical lasers. However, for 10 keV X-rays, it is merely 25 PW because of the square dependence of the wavelength of the driver in eq. (6.7). Thus it is possible to realize the self-focus of our X-rays laser pulse. This could further enhance our parameters estimated above.

6˙3. *Zeptosecond streaking*. – Atomic physics is characterized by the size of the Bohr radius a_B (~ 0.5 Å), the energy scale of the Rydberg energy W_B, and the timescale of $\tau_B = a_B/\alpha c$ (tens of as), where α is the fine-structure constant. The latter implies that for time-resolving dynamical processes in atoms, it is essential to have techniques that offer attosecond temporal resolution. The advent and experimental implementation of Attosecond Streaking (AS) [155-157] as well as the attosecond tunneling spectroscopy (ATS) [158], in which the sub-fs variation of the electric field of waveform reproducible light pulses is combined with an ultrashort attosecond triggering has made it now possible to map out electron dynamics, the fastest dynamics in nature outside the nucleus. Here the AS approach introduces an EUV (extreme ultraviolet) photon whose energy is beyond the ionization potential, while the ATS is below that.

In a recent work it has been proposed that with the increase of laser intensity such as ELI [46, 159] we can improve the pulse shortening through the premise of the Pulse Duration-Intensity Conjecture [46] (see sec. **6**˙1). This points us to the direction in which we can further shorten the laser-driven radiation pulses from attoseconds to zeptoseconds. Several other proposals over the last decade are suggesting this possibility [160, 161]. Beyond the attosecond barrier (the zeptosecond regime as we shall see below) the relevant time scale now shifts from the dynamics of atoms to that of the vacuum. Just like in atomic physics, it has been customary to explore the vacuum (Dirac's vacuum), for example, by the appropriate energy γ photon (shooting through the neighborhood of a charged particle, and thus ultimately by another photon) via the photon-photon interaction creating a pair of electron and positron. This is the process akin to the multi-photon interaction of electron(s) in an atom through the multi-photon process [162]. However, for field amplitudes higher than the Keldysh field E_K (or frequency lower) and the Keldysh parameter γ_K less than unity, the photon interaction with the atomic electron becomes nonperturbative [163]. This nonperturbative Keldysh process may be facilitated and greatly eased by the introduction of a higher energy photon (such as an EUV photon) in the presence of an intense laser field (EUV-assisted strong-field ionization), in AS and ATS, as already mentioned above.

In the vacuum physics of QED, in close analogy to atomic physics, we have the spatial scale of the Compton length $\lambda_C = \alpha a_B$, the energy scale of $mc^2 = \alpha^{-2} W_B$, and the temporal scale of the Compton time $\hbar/mc^2 = \alpha^2 \tau_B$ (on the order of zs). In other words, with strong enough laser fields we can polarize the vacuum and even "ionize" it to produce a pair of electron and positron (the Schwinger Process [164]) if the electric field applied exceeds the Schwinger field E_S (which is related to the Keldysh field simply as $E_S = \alpha^{-2} W_B/\alpha a_B = \alpha^{-3} E_K$).

Just like an atomic ionization may be helped by the presence of an EUV photon in the presence of a strong laser field (EUV-assisted strong-field ionization) (the experimental setup of ref. [156, 157]), the vacuum breakdown may be assisted by the presence of a high-energy gamma photon in the presence of intense laser fields. This process has been studied by Nikishov-Ritus and others [165, 166] and they give the electron-positron production by the presence of the gamma photon (with frequency ω_γ) and the coherent radiation fields E as eq. (6.1).

As mentioned earlier, this process is much akin to the nonperturbative Keldysh process with the EUV photon assistance to ionize the atom by the presence of intense laser field [162]. Here the corresponding parameter in vacuum to the Keldysh parameter is now $\gamma_V = 1/a_0 = mc\omega_\ell/eE$. Only a slight but important difference is the following. For the current vacuum process the dictated Lorentz invariance reflects first in eq. (6.1) (The electric field in the denominator of the exponent in eq. (6.1) is enhanced by the factor $\hbar\omega/mc^2$). Second, it demands more than one photon to initiate this process, as a single photon cannot satisfy the Lorentz-invariant four-momentum transfer. On the other hand, the atomic system's AS needs neither photons due to the lack of the Lorentz invariance in the nonrelativistic dynamics.

We thus suggest the longitudinal amplification of the streaking laser field and compression of the time scale of the fractional laser phase of as to zs by virtue of the colliding high-energy gamma photon $\hbar\omega_\gamma$ and the intense laser $\hbar\omega_\ell$. In order to probe the nonlinear property of the vacuum and its dynamics, we need to have the electric field approaching the Schwinger field, which is by itself beyond our grasp at this time. By adopting the colliding gamma photon and the laser, according to eq. (6.1), we can effectively enhance the electric field of the laser and compress the laser period when the collision of the two colliding EM waves is viewed on the center-of-mass frame and this effect in a sense has contributed to reducing the needed field E_S on the order of the Schwinger field down to $(mc^2/\hbar\omega_\gamma)E_S$. On the other hand, we need the streaking time much shortened from the fraction of the laser period (10–100 as) down to the dynamical time scale of the vacuum, the Compton time λ_C/c, which is α^2 times the former time scale ($a_B/\alpha c$), by some five orders of magnitude. This compression is accompanied by the collision of the above two kinds of photons.

We describe this collision on the center-of-mass frame of reference, on which the frame is moving along the direction of the gamma photon with $\gamma_{cm} = 1/2\sqrt{(\omega_\gamma/\omega_\ell)}$, while the laser is countermoving with the same Lorentz factor γ_{cm} (from now on we write γ_{cm} simply as γ). Here we define the crossing angle θ between the gamma photon and the laser. The polarization of the laser is in the x-direction, while it propagates in the negative z-direction. The normalized vector potential of the laser is $a_0 = eE/m\omega_\ell c$, where E is the laser electric field in the laboratory frame. We let the laser field amplitude sufficiently large to warp the vacuum and reach the Schwinger-Nikishov field $E = (m^2c^3/e\hbar)(mc^2/\hbar\omega_\ell)$. This amounts to the Schwinger-Nikishov amplitude

$$a_0^{SN} = (mc^2/\hbar\omega_\ell)(mc^2/\hbar\omega_\gamma). \tag{6.8}$$

This is Lorentz invariant.

Let us examine what happens in the center-of-mass frame of reference with this amplitude of laser interacting with the gamma photon. Since it reaches the Schwinger-Nikishov field, the vacuum emits ample pairs of an electron and a positron. Let the momentum of the electron p_0 in the laboratory frame. With the crossing angle in the the x-z plane, the generated electron momentum in the x-direction is $p_{0x} = p_0 \tan\theta \sim p_0\theta$. Note that the perpendicular momentum p_{0x} is Lorentz invariant. So is the vector potential of laser A_x. In the CM frame the electron momentum in the z-direction is much less than p_0 (*i.e.* on the order of $mc \ll p_0$). In addition to this systematic momentum of p_{0x}, the electron acquires some random momentum at birth (so does the positron). In this frame, the electron at birth has the momentum p_{0x} (in addition to the above random momentum of p_x, p_z) and the laser has the electric field of $E' = \gamma E$. In this frame of reference the electron dynamic is then identical to the situation of the attosecond streaking camera [156, 157]. Now that the high-energy photon has played its role of generating electron and positron pair and gives the proper frame of reference, we only look at the electron at birth in the intense field of laser that is Lorentz boosted in its field as E' and ω'_ℓ. According to ref. [156] the time resolution for streaking on this CM frame is given as

$$\Delta t' = T_0{}'/2\pi\sqrt{[(\hbar\omega_\ell{}'m)/(ep_{0x}{}'A_x{}'(t'))]}, \tag{6.9}$$

where all the primed quantities refer to those in the CM frame and specifically t' is the time of the electron-positron birth out of vacuum on the CM frame and $T_0{}'$ is the laser period in the CM frame. This quantity in eq. (6.9) may be rewritten as $\Delta t' = T_0/2\pi\gamma\sqrt{[(\hbar\omega_\ell{}'/p_0c)/a_0\theta]}$, noting the Lorentz invariance of p_{0x} and A_x and the Lorentz transformation of other quantities. We now require that this time resolution eq. (6.9) be the Compton time

$$\Delta t' = \hbar/mc^2. \tag{6.10}$$

This time resolution requirement leads to the normalized vector potential amplitude as

$$a_0^{res} = (mc^2/\hbar\omega_\ell\gamma^2\theta). \tag{6.11}$$

The optimal condition of streaking thus should be obtained when we equate $a_0^{res} = a_0^{SN}$. This condition sets the geometry of the collision, *i.e.* the crossing angle (see fig. 19), as

$$\theta = 4\hbar\omega_\ell/mc^2. \tag{6.12}$$

We observe the electron emission accelerated (streaked by $A_x(t)$ in the laboratory frame, though the physics is the same in the CM frame). The positron emission is coincidental with the electron so that it allows us to effectively discriminate the signal from noise. The differentiated time-of-flight in the laboratory frame is at and around the narrow angle θ from the z-axis. This way the streaking may be the angle-sweep in the downstream direction of the original gamma photon (similar to the traditional streaking camera pattern), or it may be directed sideway by a magnet to show a streaking pattern similar to [156, 157].

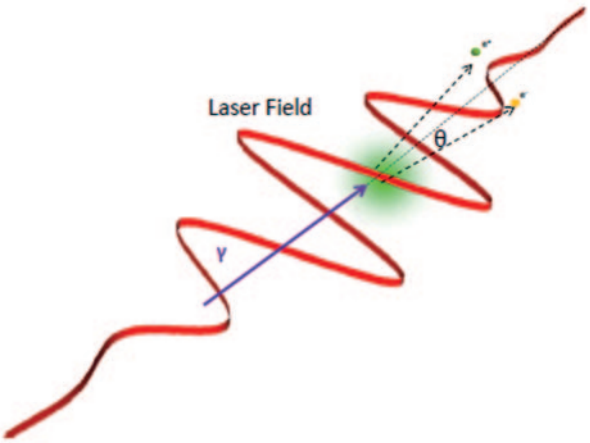

Fig. 19. – The configuration of the zeptosecond streaking method.

Let us study some examples of the experimental parameters. As we see above, once we choose the energy of the gamma photon, the other parameters are determined accordingly. A first example is to take a 1 GeV gamma photon. In this case the laser intensity required by eq. (6.8) is approximately $10^{23}\,\mathrm{W/cm^2}$. According to eq. (6.8) we can generally have the required laser intensity as inversely proportional to the gamma photon energy squared, $I \sim 10^{23}(\omega_G/\omega_\gamma)^2\,\mathrm{W/cm^2}$, where $\hbar\omega_G$ is in GeV. The crossing angle is $\theta \sim 10^{-5}$ rad from eq. (6.12).

In other words, in the example in which we have considered with the gamma photon energy of the order of GeV, the laser intensity of $10^{23}\,\mathrm{W/cm^2}$, and the crossing angle between gamma and laser of 10^{-5} rad, we are capable of resolving the Compton time scale of 1 zs on the CM frame of reference. This time scale is about 30 as in the laboratory frame. The zs scale streaking ability is endowed by the introduction of quite intense laser irradiation at $10^{23}\,\mathrm{W/cm^2}$, which is about several orders of magnitude greater than the typical intensity for the as streaking. This is again approximately in line with the Intensity-Pulse Length Conjecture [46] prediction.

We have seen that the introduction of the longitudinal streaking method of the colliding high-energy gamma photon with an intense laser pulse has brought in the following salient features in the current zs streaking method:

(1) to reduce the Schwinger intensity to break down the vacuum by 6 orders of magnitude to about $10^{23}\,\mathrm{W/cm^2}$ (with the Schwinger-Nikishov intensity);

(2) to reduce the laser period by a factor γ, approximately 3×10^4 in this example;

(3) to allow us to access the Compton time (zs) spectroscopy resolution; under the condition that the proper crossing angle θ is taken, as discussed.

More detailed experimental realizations and other conditions need to be mapped out in the future.

7. – Ultra-High-Energy Cosmic Ray acceleration

In this section we will learn that the Nature also entertains LWFA and displays a whole set of phenomena that are associated with the wakefield genesis and related particle acceleration in the highest energies we witness. A broader field of plasma astrophysics was reviewed in [167] so that we will not repeat it here.

7˙1. *Introduction.* – We are finding more evidence that the wakefield acceleration mechanism plays increasingly more important roles in accelerating particles to ultra-high energies in Nature. This is based on two factors: i) As we look for the genesis of increasingly high-energy cosmic rays, the so far seemingly almighty Fermi accelerating mechanism runs into the severe limit due to the synchrotron radiation energy loss through the stochastic acceleration assisted by randomly encountered magnetic fields approaching $\sim 10^{19}$ eV. ii) We are beginning to find that the Nature and astrophysical plasma are not just unstable and turbulent, but there are sufficient guiding principles and circumstances that generate coherent accelerating processes that permit wakefield acceleration. Among the most important guiding principles is our observation that the waves (or disturbances) with phase velocity sufficiently high (such as c) compared with the bulk plasma thermal velocity remain robust in the interaction with plasma and in return the plasma does not easily tend to become turbulent or get destroyed [3,113,168].

The origin of Ultra-High-Energy Cosmic Rays (UHECRs) with energies 10^{20} eV remains a puzzle of astrophysics. It is generally believed to be extragalactic (Kotera and Olinto [169], and references therein). The production of UHECRs has been discussed mainly in the framework of the Fermi acceleration [170], in which charged particles gain energy through a number of scatterings by the magnetic clouds. One of the necessary conditions of Fermi acceleration is the magnetic confinement: the Hillas criterion sets a constraint on the product of the magnetic field strength B and extension R of the candidate objects (Hillas criterion) [171]: $W \leq W_{\max} \sim z(B/1\,\mu\mathrm{G})(R/1\,\mathrm{kpc})\,\mathrm{EeV}$, where z is the charge of the particle. The possible candidate objects (but only marginally satisfying the Hillas criterion for 10^{20} eV production) are neutron stars, active galactic nuclei (AGN), gamma-ray bursts (GRBs), and accretion shocks in the intergalactic space. However, the acceleration of 10^{20} eV particles even in those candidate objects is not easy for the Fermi mechanism because of 1) the large number of scatterings necessary to reach highest energies, 2) energy losses through the synchrotron emission at the bending associated with scatterings, and 3) the difficulty in the escape of particles which are initially magnetically confined in the acceleration domain [169].

In the present paper we point out that there is an alternative way to accelerate charged particles (protons, ions, and electrons) to ultrahigh energies in cosmic conditions, in particular in the conditions of AGN, through the electromagnetic (EM) wave-particle interaction. Along this path two conditions are necessary: a) the accelerating structure (wave) should have a *relativistic propagation velocity* (phase velocity) very close to the speed of light c; b) the wave should have a *relativistic amplitude* (*i.e.* so large an amplitude that the particle acquires relativistic momentum in one oscillation period of the wave, $e_jE/\omega > m_j$, where E and ω are the wave electric field and frequency, e_j and m_j are the charge and mass of the j-th particle). The condition b) is needed because the electromagnetic field acceleration can yield acceleration in the direction of the wave propagation only from the nonlinear force of $v \times B/c$, called the ponderomotive force, and this term becomes significant only when the amplitude becomes relativistic [3]. We note that these two conditions may be fulfilled in a number of astrophysical settings (as

well as in many modern terrestrial laboratories [63]). When the conditions a) and b) are fulfilled, this acceleration mechanism for UHECR generation has advantages over the Fermi mechanism, for the following reasons:

1. The ponderomotive field provides an extremely high accelerating field.

2. It does not require particle bending, which would cause severe synchrotron radiation losses in extreme energies.

3. The accelerating fields and particles move in the collinear direction at the same velocity, the speed of light, so that the acceleration has a built-in coherence called "relativistic coherence" [2]; in contrast, the Fermi acceleration mechanism, based on multiple scatterings, is intrinsically incoherent and stochastic.

4. No escape problem [161] exists. Particles can escape from the acceleration region since the accelerating fields naturally decay out.

5. Whenever and wherever intense electromagnetic waves (with sufficiently high frequencies) are excited, such waves tend to exhibit coherent dynamics (see later for details).

Takahashi *et al.* [128] and Chen *et al.* [172] demonstrated that intense Alfvén waves produced by a collision of neutron stars can create wakefields to accelerate charged particles beyond 10^{20} eV. Although such a neutron star collision is believed to be related to short gamma-ray bursts [173], it is rather rare for two neutron stars to hit each other directly: It requires the same masses, otherwise the tidal field of the more massive star destroys the less massive one to form an accretion disk. Chang *et al.* [174] conducted a one-dimensional numerical simulation showing that whistler waves emitted from an AGN produce wakefields to accelerate UHECRs. (See also [29].) Earlier [175] considered acceleration and consequent gamma-ray bursts arising from the disk instabilities. This was a preliminary model, which evolved into more comprehensive model of [176]. Here we present this theory and its implications to some of the astrophysical observations such as gamma ray bursts from blazars.

The accreting supermassive black hole, the central engine of an AGN, is one of the candidates for wakefield acceleration. The accretion disk repeats transitions between a highly magnetized (low-beta) state and a weakly magnetized (high-beta) state [177]. In fact, O'Neil *et al.* [178] have found that magnetic transitions with 10–20 orbital periods are predominant in the inner disk through their 3D simulation. Strong pulses of Alfvén waves excited in the accretion disk at the transition can create intense ponderomotive potential in the relativistic jet launched from the innermost region of the accretion disk. Our analysis finds that this ponderomotive force naturally accelerates protons and nuclei up to extreme energies of ZeV (10^{21} eV). A quantitative evaluation of the genesis of UHECRs beyond 10^{20} eV from the system of an accreting black hole which consists of the black hole itself, an accretion disk, and relativistic jets (fig. 20) is considered below.

7˙2. *Intense ponderomotive mechanism.* – An accretion disk is formed around a black hole when gas accretes onto it. Since the angular velocity is higher in inner orbits, there arises a strong shear flow between gases circulating at different radii in the disk. Since the gas is almost fully ionized and Ohmic loss is negligible, magnetic fields are

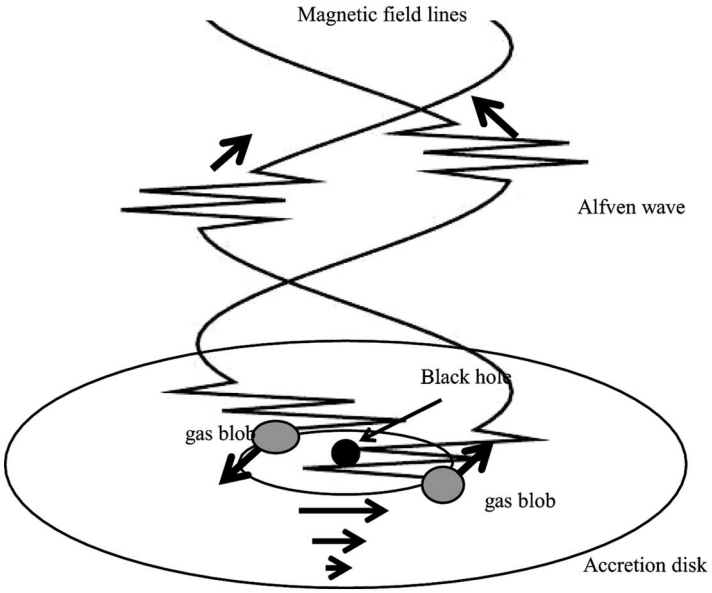

Fig. 20. – MRI (magneto-rotational instability) triggers disk disturbance [179]. This triggers gas blobs to accrete toward the central black hole, which launches massive excitation of a pulse of magnetic disturbances in the jet [176].

stretched and amplified by the shear motion. The resultant toroidal magnetic field acts as an enhanced friction between gases circulating in the different orbits and transfers the angular momentum outward, while gas is pushed inward because of the reaction of the momentum exchange.

The inner edge of the accretion disk is located around $R = 3R_{\rm g}$, where

$$R_{\rm g} = 2GM/c^2 = 3.0 \times 10^{13}(m/10^8)\,{\rm cm} \tag{7.1}$$

is the gravitational radius of the black hole. Here, m is the mass of the black hole in the unit of solar mass (2.0×10^{33} g). An ergosphere appears just outside of the causality horizon of the black hole. The gas inside the ergosphere and outside the horizon can extract rotational energy from the black hole, if it is magnetized. This energy then drives relativistic jets in the two axial directions of the accretion disk [158]. The Lorentz factor Γ of the bulk motion of the jet is observed as 10–30 in the case of active galactic nuclei.

According to Shibata, Tajima, and Matsumoto [177], the accretion disk makes transitions between two states: In the weakly magnetized state, magnetic fields are amplified by a strong shear flow, grow up to a certain point, and decay out; in other words, the disk makes transitions between these two states repeatedly. As a result, strong fluctuations are induced in the innermost region of the accretion region ($R < 10R_{\rm g}$). The physical parameters in this innermost region ($R < 10R_{\rm g}$) are estimated according to Shakura and

Sunyaev [181]:

$$\varepsilon_{\rm D} = 6.6 \times 10^6 (m/10^8)^{-1}\,{\rm erg\,cm^{-3}}, \tag{7.2}$$

$$n_{\rm D} = 2.9 \times 10^{14} (\dot{m}/0.1)^{-2} (m/10^8)^{-1}\,{\rm cm^{-3}}, \tag{7.3}$$

$$Z_{\rm D} = 2.2 \times 10^{13} (\dot{m}/0.1)(m/10^8)\,{\rm cm}, \tag{7.4}$$

$$B_{\rm D} = 1.8 \times 10^3 (m/10^8)^{-1/2}\,{\rm G}, \tag{7.5}$$

where $\dot{m}$ is the accretion rate normalized to the critical accretion rate ($\dot{M}_c = L_{\rm edd}/0.66c^2$) [14]. The viscosity parameter α is assumed to be 0.1 in the present paper. From the definition of m and $\dot{m}$, the total luminosity of the accreting black hole is given by

$$L_{\rm tot} = 1.3 \times 10^{45} (\dot{m}/0.1)(m/10^8)\,{\rm erg\,s^{-1}}. \tag{7.6}$$

The wavelength $\lambda_{\rm A}$ of Alfvén waves emitted from the accretion disk is calculated as [179]

$$\begin{aligned} \lambda_{\rm A} &= (V_{\rm AD}/C_{\rm sD})(\Omega/A) Z_{\rm D} = B_{\rm D} Z_{\rm D}/3(4\pi\varepsilon_{\rm D})^{1/2} \\ &= 5.8 \times 10^{12} (\dot{m}/0.1)(m/10^8)\,{\rm cm}, \end{aligned} \tag{7.7}$$

where $V_{\rm AD}$ is the Alfvén velocity in the accretion disk, which is calculated as

$$V_{\rm AD} = B_{\rm D}/\sqrt{4\pi m_{\rm H} n_{\rm D}} = 2.4 \times 10^7 (\dot{m}/0.1) \tag{7.8}$$

and $C_{\rm sD}$ is the sound velocity in the accretion disk:

$$C_{\rm sD} = \sqrt{\varepsilon_{\rm D}/m_{\rm H} n_{\rm D}}, \tag{7.9}$$

where $m_{\rm H}$ is the proton mass. We assume magnetic field in the accretion disk as $B_{\rm D}$ and the Keplerian rotation of gas inside the disk, *i.e.* $\Omega/A = 4/3$. The magnetic energy E_B stored in the innermost region of the accretion disk ($R < 10R_{\rm g}$) is estimated as

$$E_{\rm B} = (B_{\rm D}^2/4\pi)\pi(10R_{\rm g})^2 Z_{\rm D} = 1.6 \times 10^{48} (\dot{m}/0.1)(m/10^8)\,{\rm erg}. \tag{7.10}$$

The Alfvén waves excited in the accretion disk propagate along the global magnetic field of the jet. The normalized vector potential a, which is the Lorentz-invariant strength parameter of the wave [63], is calculated as

$$a = eE/m_e \omega_{\rm A} c, \tag{7.11}$$

where m_e and e are the electron mass and charge, and we used $E = (V_{\rm AD}/c)^{1/2}$ and $\omega_A = 2\pi V_{\rm AJ}/\lambda_{\rm A} \simeq 2\pi c/\lambda_{\rm A}$. The former comes from the conservation of Alfvén energy flux, *i.e.*, $\phi_{\rm AJ} (= cE \times B/4\pi) = \phi_{\rm AD} (= V_{\rm AD} B_{\rm D}^2/4\pi)$. We find that a is much greater that unity for a large class of AGN disks. We also find that the Alfvén velocity, in the jet (except in the very vicinity of the black hole) is close to c, and thus these Alfvén waves exert an intense ponderomotive force on electrons and ions. In this $a \gg 1$ regime, the longitudinal ponderomotive acceleration dominates the transverse acceleration. As we have mentioned in the introduction (sect. **1**˙1), the Tajima-Dawson acceleration [3] requires the conditions: a) the relativistic phase velocity and b) the relativistic amplitude.

Ashour-Abdalla *et al.* [182] studied this acceleration mechanism in the astrophysical context, where the condition b) is overwhelmingly satisfied. It was found [182] that while the ponderomotive force accelerates particles ahead of the EM pulse, it causes a density cavity in and behind the pulse (which is the cause of the trailing wakefields). In more recent works with conditions closer to the terrestrial acceleration experiments, refs. [25,183-185] found qualitatively similar results to Ashour-Abdalla's, although details vary due to parameter differences. Mourou *et al.* [6] called the EM pulse "relativistic" when $m_{\rm H}/m_e > a > 1$, and "ultrarelativistic" when $a > m_{\rm H}/m_e > 1$. No terrestrial experiments so far have been performed in the "ultra-relativistic" regime. Only a limited number of theoretical works have been devoted to this regime. Therefore, the details of the dynamics of this regime remain to be investigated in the future. Within 1D, Ashour-Abdalla *et al.* [182] find that the greater a is in the "ultra-relativistic" regime, the more the charge separation force is dominated by the EM ponderomotive force, although it is expected that this effect may be mitigated in 2D and 3D. Thus this regime should be dominated by ponderomotive acceleration. A more recent simulation study [137] shows the importance of the ponderomotive acceleration on the large a_0 regime.

The Alfvén flux inside the jet is assumed to be inversely proportional to πb^2, and b to the square root of the distance D : $b = 10R_{\rm g}(D/3R_{\rm g})^{1/2}$. This scaling is consistent with the VLBI observation of the jet of M87, the closest AGN [186]. In such a case, the value of a for the wave propagating in the jet is calculated as

$$a(D) = a_0(D/3R_{\rm g})^{-1/2}, \tag{7.12}$$

where D is the distance from the black hole along the jet, and a_0 is the value of a at the disk inner edge ($D = 3R_{\rm g}$), which is estimated as

$$a_0 = 2.3 \times 10^{10}(\dot{m}/0.1)^{3/2}(m/10^8)^{1/2}. \tag{7.13}$$

The Lorentz factor γ of the quivering motion of particles in the wave is of the order of a, *i.e.*, $\gamma \sim a$.

The Alfvén pulse generation, its collinear propagation feature, and its ponderomotive acceleration all lead to coherent dynamics. In other words, the phase between the specific wave and the particles to be accelerated are tightly locked because the phase velocity of these waves (including the Alfvén pulse in the jet under consideration) is very close to the speed of light, and because of the longitudinal nature (*i.e.*, the direction parallel to the propagation of the Alfvén wave which propagates along the direction parallel to the magnetic fields embedded in the jet) of the ponderomotive force. Further, note that the acceleration dynamics in one dimension is robust because of the relativistic coherence [2]. The mechanism known as dephasing (along with the pump depletion [3,63]) determines the maximum energy gain as well as the spectrum ([172, 187]). We focus on the wave modes propagating parallel to the jet magnetic field, since these modes are effective for the linear acceleration to highest energies. The angular frequency of the Alfvén wave is

$$\begin{aligned} \omega_{\rm A} &= 2\pi V_{\rm AJ}/\lambda_{\rm A} \cong 2\pi c/\lambda_{\rm A} \\ &= 3.2 \times 10^{-2}(\dot{m}/0.1)^{-1}(m/10^8)^{-1}\,{\rm Hz}, \end{aligned} \tag{7.14}$$

where $V_{\rm AJ} = B_{\rm J}/\sqrt{4\pi m_{\rm H} n_{\rm J}}$ is the Alfvén velocity in the jet. If we assume the conserva-

tion of magnetic flux in the jet, then the magnetic field $B_{\rm J}$ in the jet is scaled as

$$B_{\rm J} = \phi B_{\rm D}(b/10R_{\rm g})^{-2} = \phi B_{\rm D}(D/3R_{\rm g})^{-1}; \tag{7.15}$$

the plasma density $n_{\rm J}$ in the jet is calculated through the kinetic luminosity $L_{\rm J}$ of the jet,

$$L_{\rm J} = n_{\rm J} m_{\rm H} c^3 \Gamma^2 \pi b^2 = \xi L_{\rm tot}, \tag{7.16}$$

from which one infers that

$$n_{\rm J} = 2.6 \times 10^3 (\dot{m}/0.1)(m/10^8)^{-1}(\xi/10^{-2})(\Gamma/20)^{-2}(D/3R_{\rm g})^{-1}\,{\rm cm}^{-3}. \tag{7.17}$$

The effective plasma frequency ω'_p is calculated as

$$\omega'_{\rm p} = (4\pi n_{\rm J} e^2/m_e \gamma \Gamma^3)^{1/2} \tag{7.18}$$

$$= 2.1 \times 10^{-1}(\Gamma/20)^{-5/2}(\xi/10^{-2})^{1/2}(\dot{m}/0.1)^{-1/4}(m/10^8)^{-3/4}(D/3R_{\rm g})^{-1/4}\,{\rm Hz}. \tag{7.19}$$

On the other hand, the effective cyclotron frequency is derived as

$$\omega'_{\rm c} = eB_{\rm J}/m_e c\gamma = 2.3 \times 10^0(\phi/2.0)(\dot{m}/0.1)^{-3/2}(m/10^8)^{-1}(D/3R_{\rm g})^{-1/2}\,{\rm Hz}. \tag{7.20}$$

As an Alfvén wave pulse propagates along the jet, the density and magnetic fields decrease, and accordingly the ratios $\omega'_{\rm p}/\omega_{\rm A}$ and $\omega'_{\rm c}/\omega_{\rm A}$ plummet. As $\omega'_{\rm p}$ approaches $\omega_{\rm A}$, the whistler branch of the Alfvén pulse turns into the electromagnetic wave [174] and starts to excite the ponderomotive and wakefield potentials. The distance D_1 at which $\omega'_{\rm c} = \omega_{\rm A}$ is calculated as

$$D_1/3R_{\rm g} = 1.7 \times 10^3(\Gamma/20)^{-10}(\xi/10^2)^2(\dot{m}/0.1)^3(m/10^8). \tag{7.21}$$

On the other hand, the distance D_2 at which $\omega'_{\rm c} = \omega_{\rm A}$ is calculated as

$$D_2/3R_{\rm g} = 5.1 \times 10^3(\dot{m}/0.1)^{-1}(\phi/2.0)^2, \tag{7.22}$$

independently of $\dot{m}$ and m. As D increases, $\omega'_{\rm c}$ approaches ω_A. In spite of the cyclotron resonance at $\omega'_{\rm c}$, most of the wave energy is likely to tunnel from the whistler branch to the upper branch beyond the right-hand cut-off frequency

$$\omega_{\rm c}^{\rm rh} = \left[\left(\omega_{\rm c}'^2 + 4\omega_{\rm p}'^2\right)^{1/2} + \omega'_{\rm c}\right] \Big/ 2, \tag{7.23}$$

which is located above the cyclotron resonance $\omega'_{\rm c}$ in the case of the cold linear limit [188].

7˙3. *Highest-energy cosmic rays*. – The phase velocity of Alfvén wave in the jet is close to the light velocity because of the small $n_{\rm J}$ compared to $n_{\rm D}$. In such a case, the particles are accelerated by the ponderomotive force parallel to the direction of the propagation of the wave. The maximum energy $W_{\rm pm}$ in the observer's frame of the particles' gain in the region is calculated as

$$W_{\rm max} = z\int_0^{D_3} F_{\rm pm}{\rm d}D \tag{7.24}$$

$$= 4.6\times10^{19} z(\Gamma/20)(\dot{m}/0.1)^{1/2}(m/10^8)^{1/2}(D_3/3R_{\rm g})^{1/2}\,{\rm eV}$$

$$= 2.9\times10^{22} z(\Gamma/20)(\dot{m}/0.1)^{4/3}(m/10^8)^{2/3}\,{\rm eV}, \tag{7.25}$$

where

$$F_{\rm pm} = \Gamma m_e c a \omega_{\rm A} \tag{7.26}$$

is the ponderomotive force of the wave. The acceleration length is assumed to be

$$Z_{\rm acc} = {\rm ca}/\omega_{\rm A}. \tag{7.27}$$

This is consistent with Ashour-Abdalla *et al.* [161]. Further, Barezhiani and Murushidze [189] obtained an exact nonlinear longitudinal plasma wave excited by a relativistic laser pulse, neglecting the quiver motion of protons. They found that the acceleration length is increased by a factor of a in a fashion similar to eq. (7.27). This nature of acceleration lengthening can be expected to remain even in the case that proton quiver motion is not negligible, *i.e.*, $a > 10^3$. They also found that the plasma density is significantly reduced in the relativistic laser pulse because the plasma is evacuated by the strong ponderomotive force. Equation (7.25) holds as far as $Z_{\rm acc}$ is greater than D. The distance D_3 is where the acceleration finishes, defined by the equation

$$D_3 = Z_{\rm pd} = ac/\omega_{\rm A}. \tag{7.28}$$

We find that particles arrive at D_1 before D_3, in other words:

$$D_3/3R_{\rm g} = 3.9\times10^5(\dot{m}/0.1)^{5/3}(m/10^8)^{1/3} > D_1/3R_{\rm g}. \tag{7.29}$$

The energy spectrum of the accelerated charged particles has the power-law with the index of -2 in the 1D model due to the multiple dephasing occurrences when particles ride on and off different peaks of the ponderomotive or wakefield hills when the waves contain multiple frequencies (but with again the same phase velocity $\sim c$; [172]), *i.e.*, $f(W) = A(W/W_{\rm min})^{-2}$. As noted earlier, when the driving Alfvén waves and their driven ponderomotive fields hold a broad band of frequencies, their phase velocities and group velocities, respectively, are again close to the speed of light, providing the basis for the robust accelerating structure. When Alfvén waves have two- or three-dimensional features, the dephasing is more prompt, leading to higher index of the spectrum (less than -2). Let κ be the energy conversion efficiency of the acceleration (including the mode convergence efficiency mentioned earlier), $\kappa E_{\rm B} = AW_{\rm min}^2\ln(W_{\rm max}/W_{\rm min})$, *i.e.*

$$A = 1.6\times10^{33}\kappa\dot{m}m^2[W_{\rm min}^2\ln(W_{\rm max}/W_{\rm min})]^{-1}. \tag{7.30}$$

TABLE IV. – *Major features of ponderomotive acceleration in an accreting supermassive black hole.*

	Values	Units
$2\pi/\omega_{\rm A}$	$2.0\times10^{2}(\dot{m}/0.1)(m/10^{8})$	s
$1/\nu_{\rm A}$	$1.0\times10^{6}\eta^{-1}(m/10^{8})$	s
D_3/c	$1.2\times10^{9}(\dot{m}/0.1)^{5/3}(m/10^{8})^{4/3}$	s
$W_{\rm max}$	$2.9\times10^{22}z(\Gamma/20)(\dot{m}/0.1)^{4/3}(m/10^{8})^{2/3}$	eV
$L_{\rm tot}$	$1.2\times10^{45}(\dot{m}/0.1)(m/10^{8})$	erg s^{-1}
L_A	$1.2\times10^{42}\eta(\dot{m}/0.1)(m/10^{8})$	erg s^{-1}
L_γ	$1.2\times10^{41}(\eta\kappa/0.1)(\dot{m}/0.1)(m/10^{8})$	erg s^{-1}
$L_{\rm UHECR}$	$1.2\times10^{40}(\eta\kappa\zeta/10^{-2})(\dot{m}/0.1)(m/10^{8})$	erg s^{-1}
$L_{\rm UHECR}/L_{\rm tot}$	$1.0\times10^{-5}(\eta\kappa\zeta/10^{-2})$	–
$L_{\rm UHECR}/L_\gamma$	$1.0\times10^{-1}(\zeta/0.1)$	–

$\xi = L_{\rm J}/L_{\rm tot}$, $\eta = \nu_{\rm A}Z_{\rm D}/V_{\rm A}$, $\kappa = E_{\rm CR}/E_{\rm A}$, and $\zeta = \ln(W_{\rm max}/10^{20}\,{\rm eV})/\ln(W_{\rm max}/W_{\rm min})$.

The recurrence rate $\nu_{\rm A}$ of the Alfvén pulse burst is evaluated as

$$\nu_{\rm A} = \eta V_{\rm AD}/Z_{\rm D} = 1.0\times10^{2}\eta m^{-1}\,{\rm Hz}, \tag{7.31}$$

where η is episode-dependent, and on the order of unity. This is consistent with the 3-dimensional simulations conducted by O'Neill [178]. They found magnetic fluctuations, called Long Period Quasi Periodic Oscillations (LPQPO) with the period 10–20 times the Kepler rotation period. The luminosity $L_{\rm UHECR}$ of ultra-high-energy cosmic rays is

$$L_{\rm UHECR} \sim \kappa\zeta E_{\rm B}\nu_{\rm A} = 1.6\times10^{33}(\kappa\zeta/0.01)\eta\dot{m}m\,{\rm erg\,s^{-1}}, \tag{7.32}$$

where $\zeta = \ln(W_{\rm max}/10^{20}\,{\rm eV})/\ln(W_{\rm max}/W_{\rm min})$.

The ponderomotive fields in the jets accelerate both ions and electrons and therefore the AGN jet is likely to be a strong gamma-ray source as well. Although the radiation loss of protons and nuclei is negligible as far as they are accelerated parallel to the magnetic field [190], that of electrons is likely to be significant, when electrons encounter magnetic fluctuations. The gamma-ray luminosity is, therefore, found to be as

$$L_\gamma \sim \kappa E_{\rm B}\nu_{\rm A} = 1.6\times10^{34}(\kappa/0.1)\eta\dot{m}m\,{\rm erg\,s^{-1}}. \tag{7.33}$$

We summarize the major features of ponderomotive/wakefield acceleration in an accreting supermassive black hole in table IV [180].

7˙4. *Astrophysical implications and blazar characteristics.* – Radio galaxies belong to one category of AGN, which has radio lobes connected to the nucleus by relativistic jets. Their central engines are accreting supermassive ($m = 10^{6}$–10^{10}) black holes. Urry and Padovani [191] pointed out that there are parent (or misaligned) populations of blazars, which show rapid time variations in many observational bands across radio to gamma rays (10 GeV) with distinct optical and radio polarizations because of their relativistic

jet pointing almost toward us. The recent observation by the Fermi satellite reveals that many blazars emit strong gamma-rays in the GeV energy range [192-194].

We find that radio galaxies are most likely to be sources of UHECRs and their features fit well with the present theory based on the Tajima-Dawson acceleration. First, according to Ajello *et al.* [195] and Broderick [196], the local gamma-ray luminosity density of blazars is estimated as $10^{37\text{–}38}\,\mathrm{erg\,s^{-1}}$ $(\mathrm{Mpc})^{-3}$, taking into account the beaming effect of the relativistic jet. Assuming $L_{\mathrm{UHECR}}/L_\gamma \sim \zeta \sim 0.1$ (see table IV), our theoretical estimate of UHECR particle flux, averaged over the sky, becomes

$$\overline{\Phi_{\mathrm{UHECR}}} = 7.6 \times 10^{-2} l_{\gamma 37} (\zeta/0.1)(\tau_8/1.5)\ \mathrm{particles}/(100\,\mathrm{km^2\,yr\,sr}). \tag{7.34}$$

Equation (7.34) is consistent with observed flux of UHECR. Here, $l_{\gamma 37}$ is the local gamma-ray luminosity density of blazars (in units of $10^{37}\,\mathrm{erg\,s^{-1}}$ $(\mathrm{Mpc})^{-3}$) and τ_8 is the life time of UHECR particles (in units of $10^8\,\mathrm{yr}$), which is determined by GZK process: Greisen [197] and Zatsepin and Kuzmin [198] predicted that cosmic-ray spectrum has a theoretical upper limit around $5 \times 10^{19}\,\mathrm{eV}$, because of the opening of the channel to produce Δ^+ particles, which decay into pions (π^0 and $\pi^\pm$) and further into photons, electrons, protons, neutrons, and neutrinos. The flux of the cosmogenic neutrinos, produced by the GZK process, is as high as

$$\overline{\Phi_{\mathrm{UHE}\nu}} = 5.4 \times 10^{-1} l_{\gamma 37} (\zeta/0.1)(\tau/100)\ \mathrm{particles}/(100\,\mathrm{km^2\,yr\,sr}), \tag{7.35}$$

assuming the conversion efficiency of UHECR to UHEν to be 10%. This is consistent with the previous works for the case of $W_{\max} = 10^{21.5}$ (*e.g.* Kotera *et al.* [199]). The recently observed PeV neutrinos with Ice Cube experiment [200] are also consistent if we assume the power-law spectrum of the index of -2.2 in the energy region from PeV to ZeV [205]. This level of UHEν flux may be detected by a next generation space borne detector of UHECR, like JEM-EUSO, which can achieve an integrated exposure of $10^6\,\mathrm{km^2\,str\,yr}$ [201-204]) as well as next-generation neutrino facilities in the Antarctica, such as ANITA [205], ARA [206], and ARIANNA [207].

Second, blazars are also known for being highly variable at all wavelengths and all time scales. In the most extreme cases, the timescales of gamma-ray variability can be as short as a few minutes at very high energies ($\sim 100\,\mathrm{GeV}$; VHE). Such variability has been detected in several BL Lacertae objects [193, 200, 208-211]. On the other hand, our ponderomotive acceleration mechanism predicts the rapid time variability with all the time scales from the Alfvén frequency ($2\pi/\omega_{\mathrm{A}} \sim 100\,\mathrm{s}$), through the repetition period of the pulses ($1/\nu_{\mathrm{A}} \sim$ days), and to the propagation time in the jet (D_2/c, 1–10^2 years). This time variability is both for ion acceleration variability for UHECRs as well as electron variability as observed in gamma rays (electron energies are limited by the radiation energy loss by PeV [154, 212]). The finer structure of time variability is anticipated from our mechanism, as the magnetic structure may contain finer structure of braiding within the above-quoted Alfvén pulse. These observed blazer variabilities are the natural consequences deeply embedded in our model. Further, the coincidence of the pronounced luminosity peak and the reduced spectrum index observed by the Fermi satellite [213] for BL Lacs has so far no known explanation, but it is consistent with our theory [214].

Third, the multiple epoch observation of VLBA provides strong evidence that gamma-ray emission comes from a parsec scale jet [215-217]. Since the lifetime of high-energy electrons is much shorter than the propagation time, they must be locally accelerated. This is consistent with the picture of the ponderomotive acceleration, since a swarm of

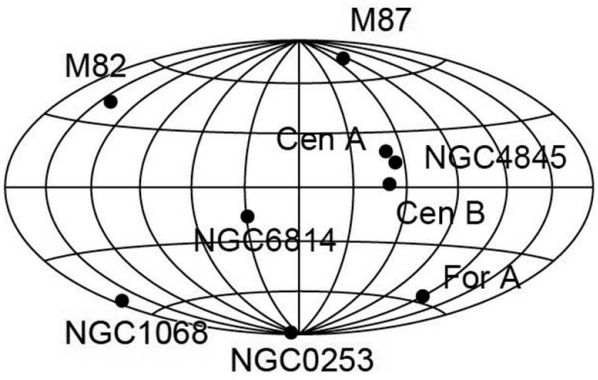

Fig. 21. – Distribution of the nine gamma-ray emitting AGNs [194] in the sky.

electrons is accelerated locally in the ponderomotive force propagating in the jets. They are likely to emit highly variable and polarized gamma-rays due to their high gamma-factor.

Our calculation yields the UHECR flux of gamma-ray emitting galaxies as

$$\Phi_{\mathrm{UHECR}} = 3.5\times10^{-3}(\zeta/0.1)(\phi_\gamma/10^{-10}\ \mathrm{photons\,cm^{-2}\,s^{-1}}) \times(\overline{E_\gamma}/1\,\mathrm{GeV})\ \mathrm{particles}/(100\,\mathrm{km^2\,yr}), \tag{7.36}$$

if the radiation pattern of UHECRs is the same as that of gamma rays. Here, Φ_γ is the gamma-ray flux and $\overline{E_\gamma}$ is the average gamma-ray energy. We found nine gamma-ray emitting AGNs [194] within the GZK horizon (≤ 70 Mpc; table V). The spectral indices are in the range from -2 to -2.8, which are consistent with our theory. Figure 21 shows the distribution of these gamma-ray emitting AGNs in the sky. This flux value is large enough to allow identification of individual sources via a clustering of events in the JEM-EUSO detector, as well as by [191-194].

7˙5. *Astrophysical evidence and implications.* – We have introduced the ponderomotive acceleration mechanism arising from the Alfvénic pulse incurred by an accretion disk around a supermassive black hole, the central engine of an AGN. This provides a natural account for UHECRs, and also for accompanying gamma-rays and their related observational characteristics, such as their luminosities, time variations, and structures. The severe physical constraints in the extreme ZeV energies by the Fermi acceleration have been lifted by the present mechanism. We have identified a number of areas of future research in need of further studies, including the cavity dynamics of superintense Alfvén pulses in 1–3 dimensions. We have presented a number of emerging astrophysical phenomena that are not easy to explain by existing theories, but are in line with natural consequences of the present acceleration mechanism. We point out that it is a natural consequence of our theory of wakefield and its application to AGN system that wakefield acceleration of UHECR ions in the jets of an AGN accompanies that of electrons simultaneously (just in a different (negative) part of the wavecrest of the wakefield). Of course, accelerated electrons (and positrons) are very emissive due to the wakefield bending forces as well as the jets' magnetic fields, so that nearly all of their energies are converted into γ-rays instantly. These gamma rays should be pointed toward the direction of the EM

TABLE V. – *Nearby gamma-ray emitting AGNs detected by Fermi satellite* [194].

Counterpart	LII	BII	Redshift	Flux (1 GeV–100 GeV) $10^{-10}\,\mathrm{erg\,cm^{-2}}$	Spectral index
NGC 0253	97.39	−87.97	0.001	6.2 ± 1.2	2.313
NGC 1068	172.10	−51.04	0.00419	5.1 ± 1.1	2.146
For A	240.15	−56.70	0.005	5.3 ± 1.2	2.158
M82	141.41	40.56	0.001236	10.2 ± 1.3	2.280
M87	283.78	74.48	0.0036	17.3 ± 1.8	2.174
Cen A Core	309.51	19.41	0.00183	30.3 ± 2.4	2.763
NGC 4945	305.27	13.33	0.002	7.5 ± 1.7	2.103
Cen B	209.72	1.72	0.012916	18.6 ± 3.5	2.325
NGC 6814	29.35	−16.02	0.0052	6.8 ± 1.6	2.544

pulse in the jet, which is also that of the jet. This consideration leads to a conclusion that if we look into the direction of the AGN jet, we should see bright γ-ray emission. We thus anticipate that blazars should show bright high-energy γ-rays. Further, these γ-rays should show the time variability that is embedded in the genesis of the γ-rays. That is, the wakefield acceleration process in the jet and how the wakefields are generated by the MRI-triggered accretion and its created magnetic shock structures should reflect the temporary profiles of these processes. In concrete it is predicted that the rise time of the bursts of γ-rays emission from a blazar should be related to the wakefield period, which in turn is tied to the Alfvén period, which is also related directly to the magnetic pulse length and again to the accreting blob size. Thus the burst rise time is now tied to the (multiple of, say, 10) MRI growth time. Meanwhile, the time separation between the episodes of bursts should be related to the magnetic buildup time in (a multiple of, say 10–100) the accretion disk rotation period. From the theory [176] the rise time and episodic period are predicted quantitatively and they are proportional to the mass of the AGN BH. When we look at the γ-burst data [213, 218, 219] they show qualitatively such characteristics and even quantitative resemblances. Or alternatively, from these quantities observed, we can in fact predict the mass of the central AGN BH (black hole). This is valuable, as usually it is difficult to determine the mass of the AGN (or blazar) BH. A recent general relativistic MHD simulation [220] also shows features consistent with the theory [166]. The MRI related rise time and episodic magnetic burst separation time scales are consistent with the theory and also eerily similar to what blazar gamma observations show. Ebisuzaki *et al.* [176] extended its theory of the current process by AGN to the process by microquasars [178].

8. – Application of LWFA to X-rays and Gamma-ray sources

Laser acceleration provides unprecedented opportunities to make the beam energies very high in a very compact size, while at the same time to provide beam properties such as the pulse length ultrashort, extreme small emittance etc. Because of both of these properties it is expected that LWFA brings in very compact X-ray and γ-ray sources. For example, LFWA excited betatron radiation in high frequencies, including X-ray

regime [221-223]. The laser Compton X-rays and γ-rays [6, 224-227] are also a very important method to generate an easily energy selective spectrum of X-rays and γ-rays with a high brilliance that surpasses far beyond in the high-photon-energy regime when synchrotron X-rays begin to lose their brilliance (*i.e.* $> 100\,\mathrm{keV}$). They are also capable of generating extremely narrow bandwidth of X-rays and γ-rays. Because of this property it is believed to play an important role in nuclear photonics [228]. Also LWFA-driven electron beams have been used to collide with another laser to induce all optical laser-Compton X-rays [229, 230]. In addition to these it is also possible to accelerate electrons by LWFA to inject into magnetic undulator to cause FEL X-rays. Meanwhile, such an undulator may be provided by high-amplitude electromagnetic waves, *i.e.* another laser pulse. In this section we only review in depth the LWFA-driven FEL processes below and leave others to be discussed in other references.

8˙1. *SASE FEL for EUV light source.* – Extreme Ultra-Violet ("EUV") with wavelengths below about 50 nm and more specifically around and below 13.5 nm can be used in microlithography processes to enhance the resolution of optical systems that are determined by the diffraction limit of light accompanying miniaturization of semiconductor integrated circuits. This technology called as extreme ultraviolet lithography (EUVL) is capable of providing resolution below 30 nm that had been impossible with conventional optical lithography utilizing deep ultraviolet (DUV) light sources with wavelengths of 248 nm or 193 nm.

The current technologies for generating high power EUV radiation at 13.5 nm, referred to as laser produced plasma (LPP), employs the deposition of laser energy into a source material such as molten tin (Sn) droplets, creating ionized gas microplasma at electron temperatures of several tens of electron volts. The current LPP radiation sources have a serious obstacle on the way to a high-volume manufacturing (HVM) source such as small efficiency of the radiation source, a limited set of discrete wavelengths and the mitigation of the plasma debris required for the protection of the EUV optics. Free-Electron Laser (FEL) based radiation sources have evident advantages in wavelength tunability, high efficiency and high output power, compared to current LPP radiation sources. The problem of debris mitigation does not exist at all. There is no need to use a multilayer coated reflective collector, of which reflectivity is limited to about 70%.

A proposed FEL [231] producing a kW-level average output power of EUV radiation utilizes high-energy electron beams of the order of 1 GeV generated from a radio-frequency–based linear accelerator (RF linac). The RF linac may consist of a high-brightness electron injector, a several-stage magnetic bunch compressor system to compress a bunch length and a main linac composed of a series of room-temperature or superconducting RF cavities with the accelerating gradient of the order of 10 MV/m as well as a beam transport system, lastly followed by undulators with a 30 m total length. The alternating magnetic fields of the undulator force relativistic electrons in a bunch to emit EUV radiation coherently on a sinusoidal trajectory due to the microbunching process, called as self-amplified spontaneous emission (SASE) FEL. The overall size of a RF linac-driven FEL-based EUV light source may require a 250 m long facility for a linac-based light source or a 120 m long, 60 m wide area for a recirculator-based light source. The costs for construction and operation of such facility may turn out incredibly so large as to hinder the FEL-based EUV light sources from industrial realization of the next generation lithography technology. Large costs of 200 M€, for facility construction including accelerator, cryogenic for super conducting RF (SRF), undulator, civil engineering etc. and operation costs of 20 M€/year for electricity, klystrons, optical components,

detectors, general maintenance, repair and helium supply for SRF, etc.

A design of FEL based EUV light source can be made by the one-dimensional FEL theory [232] as follows: The FEL amplification takes place in the undulator with the undulator period λ_u and the peak magnetic field B_u at the resonant wavelength λ_X given by

$$\lambda_X = \lambda_u(1 + K_u^2/2)/(2\gamma^2), \tag{8.1}$$

where $\gamma = E_b/m_e c^2$ is the relativistic factor of the electron beam energy E_b, $K_u = 0.934 B_u[\mathrm{T}]\lambda_u[\mathrm{cm}] = \gamma\theta_e$ is the undulator parameter, which is related to the maximum electron deflection angle θ_e. In the high-gain regime required for the operation of a SASE FEL, an important parameter is the Pierce parameter ρ_{FEL} given by

$$\rho_{\mathrm{FEL}} = (2\gamma)^{-1}(I_b/I_A)^{1/3}[\lambda_u K_u A_u/(2\pi\sigma_b)]^{2/3}, \tag{8.2}$$

where I_b is the beam current, $I_A = 17\,\mathrm{kA}$ is the Alfvén current, σ_b is the r.m.s. transverse size of the electron bunch, and the coupling factor is $A_u = 1$ for a helical undulator and $A_u = J_0(\Xi) - J_1(\Xi)$ for a planar undulator, where $\Xi = K_u^2/[4(1 + K_u^2/2)]$ and J_0 and J_1 are the Bessel functions of the first kind. Another important dimensionless parameter is the longitudinal velocity spread Λ of the beam normalized by the Pierce parameter

$$\Lambda^2 = \rho_{\mathrm{FEL}}^{-2}\left\{(\sigma_\gamma/\gamma)^2 + (\varepsilon_n^4/\sigma_b^4)[2(1 + K_u^2/2)]^{-2}\right\}, \tag{8.3}$$

where σ_γ/γ is the relativistic r.m.s. energy spread, ε_n the normalized emittance. A e-folding gain length L_{gain} over which the power grows with propagation distance z exponentially according to $\exp(2z/L_{\mathrm{gain}})$ is given by

$$L_{\mathrm{gain}} = \lambda_u(1 + \Lambda^2)/\left(4\sqrt{3}\pi\rho_{\mathrm{FEL}}\right). \tag{8.4}$$

In order to minimize the gain length, one needs a large Pierce parameter ρ_{FEL} and a normalized longitudinal velocity spread Λ sufficiently low compared to 1 that means a sufficiently small energy spread σ_γ/γ and $\varepsilon = \varepsilon_n/\gamma$. This expression applies to moderately small beam size σ_b such that the diffraction parameter $B \gg 1$ where B is defined as

$$B = 16\sqrt{2}\pi^2\gamma^{3/2}A_u K_u \sigma_b^2 (I_b/I_A)^{1/2}\lambda_u^{-2}(1 + K_u^2/2)^{-3/2}. \tag{8.5}$$

A saturation length L_{sat} required to saturate the amplification can be expressed as

$$L_{\mathrm{sat}} = L_{\mathrm{gain}} \ln\left[(P_{\mathrm{sat}}/P_{\mathrm{in}})(\Lambda^2 + 3/2)/(\Lambda^2 + 1/6)\right], \tag{8.6}$$

where P_{in} and P_{sat} are an input and a saturated power. The input P_{in} and saturated power P_{sat} are related to an electron beam power P_b according to

$$\begin{aligned} &P_b = \gamma I_b m_e c^2 = I_b E_b, \qquad P_{\mathrm{sat}} \cong 1.37\rho_{\mathrm{FEL}} P_b \exp(-0.82\Lambda^2), \\ &P_{\mathrm{in}} \cong 3\sqrt{4\pi}\rho_{\mathrm{FEL}}^2 P_b [N_{\lambda_X} \ln(N_{\lambda_X}/\rho_{\mathrm{FEL}})]^{-1/2}, \end{aligned} \tag{8.7}$$

where N_{λ_X} is the number of electrons per wavelength given by $N_{\lambda_X} = I_b\lambda_X/(ec)$.

8˙2. *LWFA-driven EUV FEL.* – We present a design example of the LWFA-based FEL for EUV radiation source at $\lambda_X = 13.5\ (6.7)\,\mathrm{nm}$ wavelength using an undulator with period $\lambda_u = 15\,\mathrm{mm}$ and gap $g = 3\,\mathrm{mm}$, *i.e.*, with gap-period ratio $g/\lambda_u = 0.2$. For a EUV light source based on FEL, a planar undulator comprising alternating dipole magnets is used, *e.g.*, a pure permanent magnet (PPM) undulator with $Nd_2Fe_{14}B$ (Nd-Fe-B) blocks or a hybrid undulator comprising PPMs and ferromagnetic poles, *e.g.*, a high-saturation cobalt steel such as vanadium permendur or a simple iron. For a hybrid undulator, the thickness of the pole and magnet is optimized in order to maximize the peak field. The peak field B_u of the gap is estimated in terms of the gap g and period λ_u according to $B_u = a[\mathrm{T}]\exp[b(g/\lambda_u) + c(g/\lambda_u)^2]$ for the gap range $0.1 < g/\lambda_u < 1$, where $a = 3.694\,\mathrm{T}$, $b = -5.068$, $c = 1.520$ for the hybrid undulator with vanadium permendur [232]. A hybrid undulator comprising Nd-Fe-B materials with grade N52 and ferromagnetic materials such as tempered Co-Fe alloys (vanadium permendur) provide the peak magnetic field $B_u \approx 1.425\,\mathrm{T}$. The corresponding undulator parameter becomes $K_u = 0.1331\lambda_u = 2.0$ for $\lambda_u = 20\,\mathrm{mm}$. Thus, the electron beam energy E_b required for producing EUV radiation at $\lambda_X = 13.5\ (6.7)\,\mathrm{nm}$ is given as $\gamma = 1290\ (1830)$ and $E_b = 659\ (935)\,\mathrm{MeV}$ by eq. (8.1). The laser plasma accelerator can provide a high-peak current bunched beam, *e.g.*, $I_A = 50\,\mathrm{kA}$ for electron charge $Q_b = 0.5\,\mathrm{nC}$ and bunch duration $\tau_b \sim 10\,\mathrm{fs}$.

Most of laser plasma acceleration experiments that successfully demonstrated the production of quasi-monoenergetic electron beams with narrow energy spread have been elucidated in terms of self-injection and acceleration mechanism in the bubble regime [91, 233], where a drive laser pulse with wavelength λ_L, peak power P_L, intensity I_L and focused spot radius r_L is characterized by the normalized vector potential $a_0 \cong 8.55 \times 10^{-10}(I_L[\mathrm{W/cm^2}])^{1/2}\lambda_L[\mu\mathrm{m}]$ given for the linear polarization. In these experiments, electrons are self-injected into a nonlinear wake, often referred to as a bubble, *i.e.*, a cavity void of plasma electrons consisting of a spherical ion column surrounded with a narrow electron sheath, formed behind the laser pulse instead of a periodic plasma wave in the linear regime. The phenomenological theory of nonlinear wakefield in the bubble (blowout) regime [91] describes the accelerating wakefield $E_z(\xi)/E_0 \approx (1/2)k_p\zeta$ in the bubble frame moving in plasma with velocity ν_B, *i.e.*, $\zeta = z - \nu_B t$, where $k_p = \omega_p/c = (4\pi r_e n_e)^{1/2}$ is the plasma wave number evaluated with plasma frequency ω_p, the unperturbed on-axis electron density n_e and the classical electron radius $r_e = e^2/mc^2$, and $E_0 = mc\omega_p/e$ is the nonrelativistic wave-breaking field approximately given by $E_0 \approx 96[\mathrm{GV/m}](n_e/10^{18}[\mathrm{cm^{-3}}])^{1/2}$. In the bubble regime for $a_0 \geq 2$, since an electron-evacuated cavity shape is determined from balancing the Lorentz force of the ion sphere exerted on the electron sheath with the ponderomotive force of the laser pulse, the bubble radius R_B is approximately given as $k_p R_B \approx 2a_0^{1/2}$ [233]. Thus, the maximum accelerating field is given by $E_{z0}/E_0 = (1/2)\alpha k_p R_B$, where α represents a factor taking into account the accelerating field reduction due to the beam loading effects.

Here we consider the self-guided wakefield accelerator, where a drive laser pulse propagates in homogeneous density plasma. The equations of longitudinal motion of an electron with the normalized energy $\gamma = E_b/mc^2$ and longitudinal velocity $\beta_z = \nu_z/c$ is approximately written as [94]

$$\mathrm{d}\gamma/\mathrm{d}z = (1/2)\alpha k_p^2 R_B(1-\xi/R_B) \quad \text{and} \quad \mathrm{d}\xi/\mathrm{d}z = 1-\beta_B/\beta_z \approx 1-\beta_B \approx 3/(2\gamma_g^2), \tag{8.8}$$

where $\xi = z - \nu_B t$ $(0 \leq \xi \leq R_B)$ is the longitudinal coordinate of the bubble frame moving at the velocity of $\nu_B = c\beta_B \approx \nu_g - \nu_{\mathrm{etch}}$, taking into account the diffraction at

the laser pulse front that etches back at the velocity of $\nu_{\rm etch} \sim ck_p^2/k^2$ [233] with laser wave number k, and $\gamma_g = (1-\beta_g^2)^{-1/2} \approx k/k_p \gg 1$ is assumed. Integrating eqs. (8.8), the energy and phase of the electron can be calculated as [94]

$$\gamma(z) = \gamma_0 + (1/3)\alpha\gamma_g^2 k_p^2 R_B \xi(z)[1 - \xi(z)/(2R_B)] \quad \text{and} \quad \xi(z) = 3z/(2\gamma_g^2), \tag{8.9}$$

where $\gamma_0 = \gamma(0)$ is the injection energy. Hence, the maximum energy gain is obtained at $\xi = R_B$ as

$$\Delta\gamma_{\max} = \gamma_{\max} - \gamma_0 \approx (1/6)\alpha\gamma_g^2 k_p^2 R_B^2 \approx (2/3)\alpha a_0 \gamma_g^2 = (2/3)\alpha\kappa_c a_0 (n_c/n_e), \tag{8.10}$$

where κ_c is the correction factor of the relativistic factor for the group velocity in a uniform plasma for self-guided pulse, *i.e.*, $\gamma_g^2 = (1-\beta_g^2)^{-1} \approx \kappa_c k^2/k_p^2 = \kappa_c n_c/n_e$, obtained from

$$\kappa_c = \frac{a_0^2}{8}\left(\sqrt{1+a_0^2/2} - 1 - \ln\frac{\sqrt{1+a_0^2/2}+1}{2}\right)^{-1}, \tag{8.11}$$

and $n_c = m\omega_L^2/4\pi e^2 = \pi/(r_e\lambda_L^2) \approx 1.115\times 10^{21}[{\rm cm}^{-3}]\lambda_L^{-2}$ is the critical plasma density. The dephasing length $L_{\rm dp}$ for self-guided bubble regime is given by

$$k_p L_{\rm dp} \approx (2/3)k_p R_B \gamma_g^2 = (4/3)\sqrt{a_0}\kappa_c (n_c/n_e). \tag{8.12}$$

For a given energy gain $E_b\,{\rm GeV}$, the operating plasma density is determined from eq. (8.10) as

$$n_e[{\rm cm}^{-3}] \approx 3.8\times 10^{17}\kappa_c a_0 \lambda_L^{-2}(E_b/\alpha)^{-1}. \tag{8.13}$$

The accelerator length equal to the dephasing length becomes

$$L_{\rm acc} = L_{\rm dp}[{\rm mm}] \approx 35(\kappa_c^{1/2}a_0)^{-1}\lambda_L(E_b/\alpha)^{3/2}, \tag{8.14}$$

while the pump depletion length due to pulse-front erosion $L_{\rm pd} = c\tau_L n_c/n_e$ is given by

$$L_{\rm pd}[{\rm mm}] \approx 25(\kappa_c a_0)^{-1}(\tau_L/30\,{\rm fs})(E_b/\alpha). \tag{8.15}$$

The dephasing length should be less than the pump depletion length, *i.e.*, $L_{\rm pd} \geq L_{\rm dp}$. Thus, the required pulse duration for self-guiding of the drive laser pulse is given by

$$\tau_L[{\rm fs}] \geq 40\kappa_c^{1/2}\lambda_L(E_b/\alpha)^{1/2}. \tag{8.16}$$

The matched spot radius becomes

$$r_m[\mu{\rm m}] \approx 8.7 R_m \lambda_L(\kappa_c a_0)^{-1/2}(E_b/\alpha)^{1/2}, \tag{8.17}$$

where $R_m \equiv k_p r_L$ is the dimensionless matched spot radius given by [94]

$$R_m = \left\{\frac{\ln(1+a_0^2/2)}{\sqrt{1+a_0^2/2} - 1 - 2\ln[(\sqrt{1+a_0^2/2}+1)/2]}\right\}^{1/2}. \tag{8.18}$$

The corresponding matched power $P_L = (k_p^2 r_L^2 a_0^2/32)P_c$ with $P_c[\mathrm{TW}] = 0.017 n_c/n_e$ is calculated as

$$P_L[\mathrm{TW}] \approx 1.56(a_0 R_m^2/\kappa_c)(E_b/\alpha). \tag{8.19}$$

The required pulse energy $U_L = P_L \tau_L$ becomes

$$U_L[\mathrm{mJ}] \geq 63(a_0 R_m^2/\kappa_c^{1/2})\lambda_L (E_b/\alpha)^{3/2}. \tag{8.20}$$

In laser wakefield acceleration, an accelerated electron beam induces its own wakefield and cancels the laser-driven wakefield. Assuming the beam loading efficiency $\eta_b \equiv 1 - E_z^2/E_M^2$ defined by the fraction of the plasma wave energy absorbed by particles of the electron bunch with the root mean square (r.m.s) transverse size σ_b, the beam-loaded field is given by $E_z = \sqrt{1-\eta_b} E_M = \alpha E_M$, where E_M is the accelerating field without beam loading, given by $E_M \approx a_0^{1/2} E_0$ for the bubble regime $a_0 \geq 2$. Thus, a loaded charge is calculated as [93]

$$Q_b \cong \frac{e}{4k_L r_e} \frac{\eta_b k_p^2 \sigma_b^2}{1-\eta_b} \frac{E_z}{E_0} \left(\frac{n_c}{n_e}\right)^{\frac{1}{2}} \approx 76[\mathrm{pC}] \frac{\eta_b a_0^{1/2} k_p^2 \sigma_b^2}{\sqrt{1-\eta_b}} \left(\frac{n_e}{10^{18}\,\mathrm{cm}^{-3}}\right)^{-1/2}. \tag{8.21}$$

Using the plasma density eq. (8.13), the loaded charge is given by

$$Q_b[\mathrm{pC}] \approx 123(1-\alpha^2) k_p^2 \sigma_b^2 \lambda_L (\alpha^3 \kappa_c)^{-1/2} E_b^{1/2}. \tag{8.22}$$

Therefore, the field reduction factor α for accelerating charge Q_b pC up to energy E_b GeV is obtained from solving the equation

$$\alpha^2 + C\alpha^{3/2} - 1 = 0, \tag{8.23}$$

where the coefficient C is defined as

$$C \equiv (Q_b/123)\kappa_c^{1/2} (k_p^2 \sigma_b^2 \lambda_L)^{-1} E_b^{-1/2}. \tag{8.24}$$

A laser pulse with wavelength $\lambda_L = 1\,\mu$m after compression is focused on the entrance of the gas cell at the normalized laser field $a_0 = 2$ corresponding to the laser intensity $I_L = 5.5 \times 10^{18}\,\mathrm{Wcm}^{-2}$. The self-guided propagation of such laser pulse in the gas cell requires the group velocity correction factor $\kappa_c = 1.19$ and the matched spot radius $R_m \equiv k_p r_m = 3.2$. The wakefield reduction factor α due to loaded charge Q_b is calculated from eq. (8.23) for the electron beam radius $k_p \sigma_b = 1$, where the coefficients are $C = 5.5$ (4.6) as $\alpha = 0.302$ (0.335).

For the FEL operation, the coupling factor $A_u(\Xi) = J_0(\Xi) - J_1(\Xi)$ are $A_u = 0.8083$ with $\Xi = K_u^2/[4(1+K_u^2/2)] = 0.3329$. The r.m.s. transverse size of the electron bunch is set to $\sigma_b = 25\,\mu$m in the undulator and is usually much larger than the normalized transverse emittance ε_n of the order of $1\,\mu$m for a laser plasma accelerator produced electron beam. For the peak current $I_b = 50\,$kA with the number of electrons per wavelength $N_{\lambda_X} = 1.4 \times 10^7$ and the diffraction parameter $B \gg 1$, main LPA and FEL parameters are obtained from eqs. (8.13)–(8.24) and eqs. (8.1)–(8.7), respectively, as shown in table VI. Here, the longitudinal velocity spread Λ is $\Lambda \approx 1$ for setting $\sigma_\gamma/\gamma \approx \rho_{\mathrm{FEL}}$,

as given by eq. (8.3). Thus, the e-folding gain length is $L_{\rm gain} = \lambda_u/(2\sqrt{3}\pi\rho_{\rm FEL})$, saturated power $P_{\rm sat} \cong 0.6\rho_{\rm FEL}P_b$ and saturation length $L_{\rm sat} = L_{\rm gain}\ln(15P_{\rm sat}/7P_{\rm in})$, where $P_{\rm sat}/P_{\rm in} = 0.056\rho_{\rm FEL}[(N_{\lambda_X}/\rho_{\rm FEL})\ln(N_{\lambda_X}/\rho_{\rm FEL})]^{1/2}$. The spectral bandwidth of radiation is given by $\Delta\lambda_X/\lambda_X \sim 1/N_u$ for the total number of the undulator periods N_u. The r.m.s. radiation cone angle is obtained as $\theta_X = (1 + K_u^2/2)^{1/2}/(2\gamma\sqrt{N_u})$. The average power at the repetition frequency $f_{\rm rep}$ is estimated as $P_{\rm av} \sim P_{\rm sat}\tau_X f_{\rm rep}$, assuming the radiation duration $\tau_X \approx \tau_b \sim 10\,{\rm fs}$.

The repetition rate $f_{\rm rep}$ to be required for generating the average EUV power $P_{\rm EUV}$ yields $f_{\rm rep} \approx P_{\rm EUV}/(P_{\rm sat}\tau_X)$. For the production of the EUV power $P_{\rm EUV}$, one needs the average laser power $P_{L{\rm av}} \approx U_L f_{\rm rep}$. The minimum average laser power takes place for the case of the undulator period 15 mm as compared with the cases of the undulator period of 5 mm, 10 mm, 20 mm and 25 mm [95]. As the average beam power is given by $P_{b{\rm av}} = Q_b E_b f_{\rm rep}$, the efficiency of the electron beam acceleration is

TABLE VI. – *Parameters for laser plasma accelerator-based EUV FEL light sources.*

Case	A	B
Drive laser		
Wavelength [μm]	1	1
Average laser power [MW]	1.19	2.60
Repetition rate [MHz]	0.315	0.473
Laser energy per pulse [J]	3.79	5.51
Peak power [TW]	59	75
Pulse duration [fs]	65	73
Matched spot radius [μm]	27	30
Laser plasma accelerator		
Electron beam energy [MeV]	659	935
Plasma density [$10^{17}\,{\rm cm}^{-3}$]	4.2	3.2
Accelerator length [mm]	51	74
Charge per bunch [nC]	0.5	0.5
Bunch duration [fs]	10	10
Energy spread [%]	~ 1.6	~ 1.1
Transverse beam size [μm]	25	25
Peak current [kA]	50	50
Average beam power [kW]	104	221
Free Electron Laser		
Undulator period (Gap) [mm]	15 (3)	15 (3)
Radiation wavelength [nm]	13.5	6.7
Peak magnetic field [T]	1.425	1.425
Undulator parameter K_u	2.0	2.0
Pierce parameter [%]	1.60	1.125
Gain length [mm]	86	123
Saturation length [cm]	102	144
Number of periods	68	96
Spectral bandwidth [%]	1.5	1.0
r.m.s. Radiation cone angle [μrad]	82	48
Input power [MW]	5.3	5.3
Saturated power [GW]	317	317
Duration of EUV pulse [fs]	10	10
Average EUV power [kW]	1	1.5

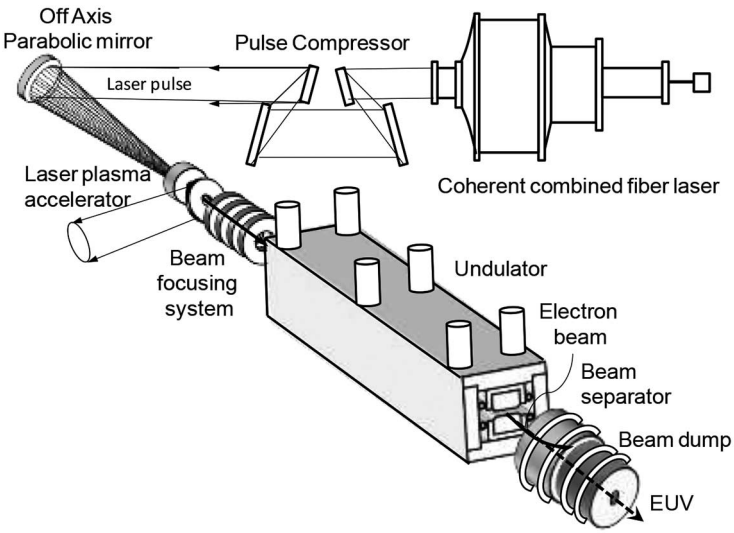

Fig. 22. – A schematic illustration for the EUV light source based on a compact Free-Electron-Laser–driven by a fibre laser-based [40] plasma accelerator.

$\eta_{\text{laser}\to\text{beam}} = P_{b\text{av}}/P_{L\text{av}} \approx Q_b E_b/U_L$. The efficiency of the production of EUV radiation yields $\eta_{\text{laser}\to\text{EUV}} \approx P_{\text{EUV}}/P_{L\text{av}}$.

Table VI summarizes design examples of main LPA and FEL parameters for the FEL EUV radiation source with the radiation power of 1 kW at wavelength of 13.5 nm (case A) and 6.7 nm (case B), using the undulator with the period of 15 mm and the gap of 3 mm, assuming a FWHM electron bunch duration of ~ 10 fs, a relative energy spread of $\Delta E/E_b \sim 1\%$ high-repetition rate, high-average power laser, such as the coherent combining fibre-based chirped-pulse amplification (CPA) laser [40]. The bunch duration of electron beam in the injector stage at plasma density $n_e \approx 10^{18}\,\text{cm}^{-3}$ is assumed to be ~ 10 fs in full width at half maximum (FWHM), based on the measurement of the electron bunch duration in the recent laser wakefield acceleration experiment [80]. The relative energy spread of an accelerated electron beam with on injection energy of $0.1E_b$, where E_b is the final beam energy in the accelerator stage, is assumed to be of the order of 10% in the injector stage. After acceleration up to 10 times higher energy in the accelerator stage, the relative energy spread at the final beam energy is reduced to $\Delta E/E_b \sim 1\%$, due to adiabatic damping in the longitudinal beam dynamics. The transverse beam size is tuned by employing the beam focusing system. Figure 22 illustrates schematically the EUV light source, based on a compact FEL driven by a fibre laser-based plasma accelerator.

8˙3. *LWFA-driven hard X-ray FEL.* – Here we consider feasibility of a compact hard X-ray FEL capable of reaching a wavelength of $\lambda_X = 0.1$ nm, which requires the electron beam energy of the multi-GeV range in case of a modest undulator period of the order of a few centimeters. One of the prominent features of laser-plasma accelerators is to produce 1 fs-level bunch duration, which is unreachable by means of the conventional accelerator technologies. The X-ray FELs rely on SASE, where the coherent radiation builds up in a single pass from the spontaneous (incoherent) undulator radiation. In an undulator the

radiation field interacts with electrons snaking their way when overtaking them so that electrons are resonantly modulated into small groups (micro-bunches) separated by a radiation wavelength and emit coherent radiation with a wavelength equal to the micro-bunch period length. This process requires an extremely high-current beam with small energy spread and emittance in addition to a long precisely manufactured undulator. Therefore, the conventional accelerator-based FELs need a long section of the multi-stage bunch compressor called as a "chicane" that compresses a bunch from an initial bunch length of a few picoseconds to the order of 100 fs to increase the current density of the electron beam up to the order of the kilo-ampere level before injecting it to the undulator, whereas the laser-plasma-accelerator–based FELs would have no need of any bunch compressor. Although the present LWFAs need further improvements in the beam properties such as energy, current, qualities and operating stability, the beam current of 100 kA level (*i.e.* 100 pC electron charge within 1 fs bunch duration) allows a drastic reduction to the undulator length of several meters for reaching the saturation of the FEL amplification. In addition to inherently compact laser and plasma accelerator, a whole FEL system will be operational on the table-top scale. The realization of laser-driven compact table-top X-ray FELs will benefit science and industry over a broad range by providing new tools enabling the leading-edge research in small facilities, such as universities and hospitals.

The SASE FEL driven by an electron beam with energy γ requires the transverse normalized emittance $\varepsilon_n < \gamma\lambda_x$, where λ_x is a FEL wavelength of radiation from the undulator with period λ_u, given by eq. (8.1) and K_u is the undulator parameter with the magnetic field strength on the undulator axis B_u, *i.e.*, $K_u = 0.934\lambda_u[\mathrm{cm}]B_u[\mathrm{T}]$. For lasing a hard X-ray region $\lambda_x \approx 0.1\,\mathrm{mm}$ (photon energy $E_{\mathrm{photon}} = 12.4\,\mathrm{keV}$) from the undulator of $\lambda_u = 1.5\,\mathrm{cm}$ with the magnetic field of $B_u = 1.425\,\mathrm{T}$ ($K_u = 2.0$) at the beam energy $E_b = 7.665\,\mathrm{GeV}$ ($\gamma = 1.5 \times 10^4$), the normalized emittance should be $\varepsilon_n < 1.5\,\mu\mathrm{m\,rad}$. In addition, it is essential for SASE FELs to inject electron beams with a very high peak current of the order of 100 kA. This requirement imposes a charge of $\sim 200\,\mathrm{pC}$ on the laser plasma accelerator design in the case of accelerated bunch length of 2 fs.

Here we present a design example of 0.1 nm hard X-ray FEL driven by 7.665 GeV electron beam delivered from a self-guided laser wakefield accelerator driven by a laser pulse with wavelength $\lambda_L = 0.8\,\mu\mathrm{m}$ and normalized vector potential of $a_0 = 2$, which has the group velocity correction factor $\kappa_c = 1.19$ and the matched spot radius $R_m = 3.2$. The wakefield reduction factor α due to loaded charge $Q_b = 200\,\mathrm{pC}$ is calculated from eq. (8.23) for the electron beam radius $k_p\sigma_b = 1$, where the coefficients are $C = 0.8$ and $\alpha = 0.72$. The r.m.s. transverse size of the electron bunch is set to $\sigma_b = (\bar{\beta}_u\varepsilon_n/\gamma)^{1/2} = 10\,\mu\mathrm{m}$ in the undulator, assuming the average beta function in the undulator $\bar{\beta}_u = 1\,\mathrm{m}$ and the normalized emittance $\varepsilon_n = 1.5\,\mu\mathrm{m\,rad}$. For the peak current $I_b = 100\,\mathrm{kA}$ with the number of electrons per wavelength $N_{\lambda_X} \sim 2000$, the main LPA and FEL parameters are obtained from eqs. (8.13)–(8.24) and eqs. (8.1)–(8.7), respectively, as shown in table VII.

In the saturation regime, the photons flux of X-ray radiation is

$$N_{\mathrm{photon}} = P_{\mathrm{sat}}/(eE_{\mathrm{photon}}) \approx 0.6\rho_{\mathrm{FEL}}E_bI_b/(eE_{\mathrm{photon}}) \approx 7.4 \times 10^{26}\,\mathrm{s}^{-1}, \tag{8.25}$$

for $E_b = 7.665\,\mathrm{GeV}$, $E_{\mathrm{photon}} = 12.4\,\mathrm{keV}$ ($\lambda_X = 0.1\,\mathrm{nm}$), $\rho_{\mathrm{FEL}} = 0.0032$ and $I_b = 100\,\mathrm{kA}$

$$\begin{aligned} B_{\mathrm{peak}} &= N_{\mathrm{photon}}\gamma^2/(4\pi^2\varepsilon_n^2)/(10^3\Delta\lambda_X/\lambda_X) \\ &\approx 4.7 \times 10^{32}\,\mathrm{photons/s/mm^2/mrad^2/0.1\%\,BW}, \end{aligned} \tag{8.26}$$

TABLE VII. – *Parameters for LWFA-based hard X-ray FEL light sources.*

Drive laser	
Wavelength λ_L	$0.8\,\mu$m
Laser energy per pulse U_L	23 J
Peak power P_L	287 TW
Pulse duration τ_L	80 fs
Laser spot radius	$47\,\mu$m
Laser plasma accelerator	
Electron beam energy E_b	7.665 GeV
Plasma density n_e	$1.3 \times 10^{17}\,\mathrm{cm}^{-3}$
Accelerator length L_{acc}	45 cm
Charge per bunch Q_b	0.2 nC
Bunch duration τ_b	2 fs
Energy spread (r.m.s) σ_γ/γ	$\sim 0.3\%$
Transverse beam size σ_b	$10\,\mu$m
Peak beam current I_b	100 kA
Free Electron Laser	
Undulator period λ_u (Gap g)	15 (3) mm
Radiation wavelength λ_X	0.1 nm
Peak magnetic field B_u	1.425 T
Undulator parameter K_u	2.0
Pierce parameter ρ_{FEL}	0.32%
Gain length L_{gain}	0.43 m
Saturation length L_{sat}	3.8 m
Number of periods	254
Spectral bandwidth $\Delta\lambda_X/\lambda_X$	0.4%
r.m.s. Radiation cone angle θ_X	$3.6\,\mu$rad
Input power P_{in}	0.51 GW
Saturated power P_{sat}	1.47 TW
Duration of X-ray pulse τ_X	2 fs
Photon flux N_{photon}	$7.4 \times 10^{26}\,\mathrm{s}^{-1}$
Peak brilliance B_{peak}	4.7×10^{32} photons/(s mm^2 mrad^2 0.1% BW)

where $\Delta\lambda_X/\lambda_X \sim 1/N_u \approx 0.004$ is the spectral bandwidth of the X-ray radiation. This peak brilliance is comparable to large-scale X-ray FELs based on the conventional linacs [234].

8˙4. *All-optical gamma beam source for detection for Nuclear Resonance Fluorescence.* – A high-quality gamma-beam generated from inverse Compton scattering off relativistic electron beams interacting with an intense laser pulse arouses interest in photonuclear physics and nuclear astrophysics research, characterization of nuclear materials or radioactive waste and so on. Here, we present a table-top all-optical laser plasma accelerator-based Gamma beam source comprising a high power laser system with synchronous dual outputs, a GeV-class laser plasma accelerator, and a scatter optics whereby the laser pulse is focused onto the electron beam to generate a Gamma-beam via inverse

Compton scattering with photon energy of 2–20 MeV.

In Compton scattering of a laser photon with energy $\hbar\omega_L$ ($\hbar\omega_L[\mathrm{ev}] = 1.240/\lambda_L[\mu\mathrm{m}]$ for laser wavelength $\lambda_L\,\mu$m) off an electron, the maximum energy of scattered photon is given by $E_{\gamma\,\max} = 4\gamma_e^2 a\hbar\omega_L$, where $\gamma_e = E_b/m_e c^2$ is the relativistic factor of the electron beam energy E_b with the electron rest mass $m_e c^2 \cong 0.511\,\mathrm{MeV}$, and the factor $a = [1 + 4\gamma_e(\hbar\omega_L/m_e c^2)]^{-1}$. In the laboratory frame, the differential cross-section of Compton scattering [235] is given by

$$\frac{\mathrm{d}\sigma}{\mathrm{d}\kappa} = 2\pi a r_e^2 \left\{ 1 + \frac{\kappa^2(1-a)^2}{1-\kappa(1-a)} + \left[\frac{1-\kappa(1+a)}{1-\kappa(1-a)}\right]^2 \right\}, \tag{8.27}$$

where $\kappa = E_\gamma/E_{\gamma\,\max}$ is energy of a scattered photon normalized by the maximum photon energy and $r_e^2 \cong 79.4\,\mathrm{mb}$ with the classical electron radius r_e. In the laboratory frame, the scattering angle θ of photon is given by $\tan\theta = \gamma_e^{-1}[(1-\kappa)/a\kappa]^{1/2}$. Integrating the differential cross-section over $0 \le \kappa \le 1$, the total cross-section of Compton scattering becomes

$$\sigma_{\mathrm{total}} = \pi r_e^2 a \left[\frac{2a^2 + 12a + 2}{(1-a)^2} + a - 1 + \frac{6a^2 + 12a - 2}{(1-a)^3} \ln a \right]. \tag{8.28}$$

This total cross-section leads to the cross-section of Thomson scattering $\sigma_{\mathrm{Thomson}} = 8\pi r_e^2/3 = 665\,\mathrm{mb}$ for the electron beam energy $E_b \to 0$. The fractional cross-section for the photon energy range $E_{\gamma\,\max} - \Delta E_\gamma \le E_\gamma \le E_{\gamma\,\max}$ is given by

$$\begin{aligned} \Delta\sigma = 2\pi a r_e^2 \Delta\kappa \Bigg[& \left(\frac{1+a}{1-a}\right)^2 + \frac{4}{(1-a)^2}\left(1 + \frac{1-a}{a}\Delta\kappa\right)^{-1} \\ & + (a-1)\left(1 + \frac{\Delta\kappa}{2}\right) + \frac{1 - 6a - 3a^2}{(1-a)^3\Delta\kappa} \ln\left(1 + \frac{1-a}{a}\Delta\kappa\right) \Bigg], \end{aligned} \tag{8.29}$$

with $\Delta\kappa = \Delta E_\gamma/E_{\gamma,\max} \ll 1$. All photons in this energy range are scattered to the forward direction within a half-cone angle $\theta \sim \gamma_e^{-1}\sqrt{\Delta\kappa/a}$. For an electron beam interacting with a laser pulse at an angle of α_{int} in the horizontal plane (x-plane), a luminosity representing the probability of collisions between electron and laser beams per unit cross-section per unit time is obtained by $L[\mathrm{mb}^{-1}\,\mathrm{s}^{-1}] = N_e N_L f_L/2\pi\Sigma$, where N_e is the number of electrons contained in an electron bunch, N_L is the number of photons per laser pulse, f_L is a repetition rate of laser pulses and $\Sigma = \sigma_L^2 S$ is an area where two beams overlap with

$$S \equiv \left(1 + \frac{\sigma_e^2}{\sigma_L^2}\right)\cos\left(\frac{\alpha_{\mathrm{int}}}{2}\right)\left[1 + \left(\frac{1 + \sigma_{ez}^2/\sigma_{Lz}^2}{1 + \sigma_e^2/\sigma_L^2}\right)\frac{\sigma_{Lz}^2}{\sigma_L^2}\tan^2\left(\frac{\alpha_{\mathrm{int}}}{2}\right)\right]^{1/2}, \tag{8.30}$$

where σ_e and σ_{ez} are the root mean square (r.m.s.) transverse size and bunch length of the electron beam, σ_L and σ_{Lz} the r.m.s. transverse spot size and pulse length of the laser beam, respectively. For a head-on collision providing the efficient Gamma-beam production, a crossing angle between electron and laser beams is chosen to be $\alpha_{\mathrm{int}} = 0$. Tuning the beam focusing system and the interaction optics so as to be $\sigma_e \approx \sigma_L$, the luminosity turns out to be $L = N_e N_L f_L/(\pi r_{L\,\mathrm{int}}^2)$, where $r_{L\,\mathrm{int}} = 2\sigma_L$ is

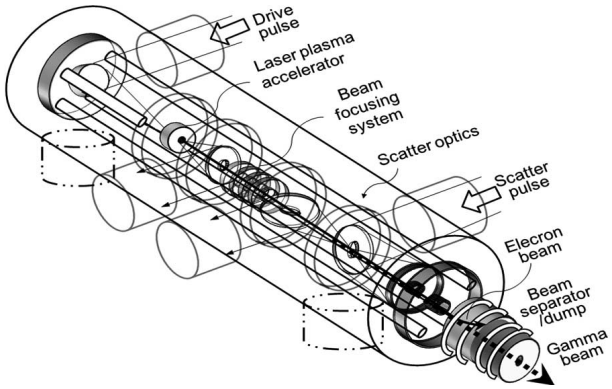

Fig. 23. – A schematic illustration for the Gamma-beam source, based on inverse Compton scattering off relativistic electron beams driven by a laser wakefield accelerator.

a laser spot radius at the interaction point. Using $N_e = Q/e = 6.24 \times 10^9 Q[\mathrm{nC}]$ and $N_L = U_{LS}/(e\hbar\omega_L) = 5.0334 \times 10^{18} U_{LS}[\mathrm{J}]\lambda_L[\mu\mathrm{m}]$, where Q_e is charge of the electron bunch, $U_{LS} = P_{LS}\tau_{LS}$ is energy of the scatter pulse with peak power P_{LS} and duration τ_{LS}, the luminosity is calculated as

$$(8.31)\quad L[\mathrm{mb}^{-1}\,\mathrm{s}^{-1}] = \frac{N_e N_L f_L}{2\pi\Sigma} = \frac{Q I_{LS\,\mathrm{int}}\tau_{LS} f_L}{2e^2\hbar\omega_L} \approx 1.57 \times 10^{-14}\lambda_L[\mu\mathrm{m}]Q_e[\mathrm{nC}]I_{LS\,\mathrm{int}}[\mathrm{W/cm}^2]\tau_{LS}[\mathrm{fs}]f_L[\mathrm{s}^{-1}],$$

where $I_{LS\,\mathrm{int}}$ is the focused intensity of the scatter pulse at the interaction point. Thus, the total Gamma-beam flux is given by

$$(8.32)\quad N_\gamma[\mathrm{s}^{-1}] = L\sigma_{\mathrm{tot}} \approx 1.57 \times 10^{-14}\sigma_{\mathrm{tot}}[\mathrm{mb}]\lambda_L[\mu\mathrm{m}]Q_e[\mathrm{nC}]I_{LS\,\mathrm{int}}[\mathrm{W/cm}]\tau_{LS}[\mathrm{fs}]f_L[\mathrm{s}^{-1}].$$

A fractional Gamma-beam flux with photon energy spread $\Delta\kappa = \Delta E_\gamma/E_{\gamma\,\max}$ is estimated as

$$(8.33)\quad \Delta N_\gamma[\mathrm{s}^{-1}] = L\Delta\sigma \approx 1.57 \times 10^{-14}\Delta\sigma[\mathrm{mb}]\lambda_L[\mu\mathrm{m}]Q_e[\mathrm{nC}]I_{LS\,\mathrm{int}}[\mathrm{W/cm}^2]\tau[\mathrm{fs}]f_L[\mathrm{s}^{-1}].$$

Figure 23 illustrates schematically the Gamma-beam source, generated via laser Compton scattering off electron beams driven by a laser wakefield accelerator.

Here we consider an application of the all-optical gamma beam source to the detection for nuclear resonance fluorescence. When a nucleus absorbs photons equal to the excitation energy, the nucleus is excited to the definite state due to resonant excitation, instantaneously followed by decaying mainly to a lower state with a re-emission of the radiation equivalent to the absorbed energy. This process is referred to as nuclear resonance fluorescence (NRF) [225, 236, 237], for which the lifetime of the excited nuclear state of the order of 100 ps corresponds to an energy width $\Gamma \sim 10^{-5}$ eV for the absorption and re-emission at the exact resonance. Since this resonant property of NRF

is in unique contrast to other nuclear absorption phenomena such as photonuclear reactions and the giant dipole resonance, involving the continuum states of nuclei with broad absorption spectra, the NRF interrogation is capable of characterizing a nucleus in the nuclear structure and its excited states in terms of their energy, lifetime, angular momentum, and parity. The absorption cross-section for a nucleus in the state i to capture a photon and be directly excited to the state j, taking into account the Doppler broadening due to the thermal motion of the nucleus at the resonance, is given by [225]

$$\sigma_{\mathrm{NRF}}(E_{\mathrm{res}}) = 2.5 \times 10^3[\mathrm{b}] \left(\frac{1\,\mathrm{MeV}}{E_{\mathrm{res}}}\right)^2 \frac{2J_j+1}{2J_i+1} \frac{\Gamma_0}{\Gamma_{\mathrm{thermal}}}\,, \tag{8.34}$$

where J_j denotes spin of the i-state, E_{res} is the excitation energy of the i-state relative to the j-state, Γ_0 is the intrinsic width of the resonantly excited state to the ground state and $\Gamma_{\mathrm{thermal}}$ is the Doppler width, defined by $\Gamma_{\mathrm{thermal}} = E_{\mathrm{res}}(2kT_{\mathrm{eff}}/m_{\mathrm{nucleus}}c^2)^{1/2}$ for the effective temperature T_{eff} and the mass m_{nucleus} of the nucleus with the Boltzmann constant k. For a typical radioactive nuclide with nuclear mass number $A = 200$, $E_{\mathrm{res}} = 1\,\mathrm{MeV}$ and $T_{\mathrm{eff}} = 300\,\mathrm{K}$, the Doppler width is $\Gamma_{\mathrm{thermal}} = 0.5\,\mathrm{eV}$.

For the NRF interrogation, Gamma-ray sources need to cover the excitation energies of most of the nuclides from 10 keV to 10 MeV. Using such a Gamma-ray source, consider the detection of NRF from a nuclide contained at a concentration level of $C_{\mathrm{nucl}}\,\mathrm{Bq/g}$ in a material such as concrete when irradiated with Gamma rays at a flux of F_{GB} photons/s/keV. The number of NRF photons detected for the measuring time T_{measure} by a detection system with the efficiency of $\varepsilon_{\mathrm{detector}}$ can be estimated as [236]

$$N_{\mathrm{NRF}} = \varepsilon_{\mathrm{detector}}\sigma_{\mathrm{NRF}}F_{\mathrm{GB}}L_{\mathrm{int}}T_{\mathrm{measure}}d_{\mathrm{material}}C_{\mathrm{nucl}}N_A/(A_S m_A), \tag{8.35}$$

where L_{int} is the interaction length, d_{material} the density of material, $N_A = 6.022 \times 10^{23}\,\mathrm{mol}^{-1}$ the Avogadro's constant, A_S the specific activity and m_A the atomic mass number of the radioactive nucleus. Here $n_{\mathrm{nucl}} = d_{\mathrm{material}}C_{\mathrm{nucl}}N_A/(A_S m_A)$ represents the number of radioactive nuclei contained in a unit volume of material. As an example, the number of NRF photons from U-238 with resonance energy $E_{\mathrm{res}} = 2.17\,\mathrm{MeV}$, cross-section $\sigma_{\mathrm{NRF}} = 28\,\mathrm{mb\text{-}keV}$ and specific activity $A_S = 1.2 \times 10^4\,\mathrm{Bq/g}$ contained at a concentration level $C_{\mathrm{nucl}} = 1\,\mathrm{Bq/g}$ in concrete with density $d_{\mathrm{material}} = 2\,\mathrm{g/cm}^3$, corresponding to $n_{\text{U-238}} \sim 4.2 \times 10^{17}\,\mathrm{cm}$, will be $N_{\mathrm{NRF}} \sim 1.2 \times 10^{-6}F_{\mathrm{GB}}$, detected by the detector with the total efficiency $\varepsilon_{\mathrm{detector}} = 1\%$ for the interaction length $L_{\mathrm{int}} = 1\,\mathrm{m}$ and the measuring time $T_{\mathrm{measure}} = 100\,\mathrm{s}$.

The all-optical laser plasma accelerator-based Gamma-beam source at photon energy of 2.17 MeV for the detection of NRF photons from U-238 can be designed as follows. The maximum photon energy of $E_{\gamma\,\max} = 2.17\,\mathrm{MeV}$ is generated from the inverse Compton scattering between a laser of $0.8\,\mu\mathrm{m}$ wavelength and electrons with beam energy of $E_b = 303.4\,\mathrm{MeV}$. Using the design formulas eqs. (8.13)–(8.24), an electron beam with energy of 303.4 MeV and charge of 1 nC can be delivered from the laser plasma accelerator driven by a laser pulse with the peak power of 44 TW, duration of 56 fs, and energy of 2.5 J, which is focused on spot radius of $12\,\mu\mathrm{m}$, corresponding to $a_0 = 3$, in the entrance of gas cell with length of 3 cm, operated at plasma density of $1 \times 10^{18}\,\mathrm{cm}^{-3}$. Provided that the electron beam with radius of $25\,\mu\mathrm{m}$ interacts head-on with a scatter laser pulse with wavelength of $0.8\,\mu\mathrm{m}$, peak power of 10 TW, duration of 1 ps and energy of 10 J, focused on spot radius of $25\,\mu\mathrm{m}$, correspondingly at the intensity of $I_{L\,\mathrm{int}} = 10^{18}\,\mathrm{W/cm}^2$, a total Gamma-beam flux yields 8.3×10^{10} (8.3×10^{12}) photons/s at the repetition rate

of 10 Hz (1 kHz), while a fractional Gamma-beam flux with the spectral bandwidth of 0.1% results in 1.3×10^8 (1.3×10^{10}) photons/s, corresponding to the gamma ray flux of $F_{\mathrm{GB}} \sim 5.8 \times 10^7$ (5.8×10^9) photons/(s keV). Accordingly, the number of NRF photons from U-238 yields $N_{\mathrm{NRF}} \sim 440$ (440), which will be detected by the detector with the total efficiency of 10% (1%) for the interaction length $L_{\mathrm{int}} = 1\,\mathrm{m}$ and the measuring time $T_{\mathrm{measure}} = 100\,\mathrm{s}$ (10 s). Here the values in brackets correspond to the performance of the Gamma-beam source at the operation of 1 kHz. Figure 23 illustrates schematically the Gamma-beam source, generated via laser Compton scattering off electron beams driven by a laser plasma accelerator.

9. – Application to medicine

9˙1. *Introduction.* – Though materials science and technology may be very important as part of LWFA applications, here we focus on medical applications. The intense laser technology has given a new set of impetus to make innovations in nuclear medicine and pharmacology, not to speak in the broader medicine at large. Our applications to medicine are enabled on our discussions from sect. **3** (electron beams), sect. **5** (ions beams), and sect. **8** (gamma beams).

As a direct application of LWFA electrons, we recognize the use of LWFA ultrashort electron pulses (compared with electron bunches of conventional accelerators) for ultrafast radiology. Crowell *et al.* [238] as well as Brozek-Pluskab *et al.* [239] have applied LWFA electrons to ultrafast radiolysis. Richter *et al.* [240] have irradiated LWFA created electrons on *in vitro* cells. X-rays emitted by betatron oscillations in LWFA [221-223] may be also employed for diagnosis such as phase contrast imaging [241]. Their direct use of LWFA electrons as therapy applications include the intraoperative radiation therapy (IORT) [242]. This approach takes advantage of the compactness of the electron source for the surgeon, while he can avoid the surface tissue damage due to the electron's higher dose at the entrance by opening the organ with tumor during the operation. These applications are well reviewed in the latest book [243], so that we need not to delve into these topics here further.

The usage of γ-photons for various applications (including medicine in particular) that was generated by the laser Compton X-ray process is getting quite important of late. In this category, what is called sometimes all-optical γ-photon generation has been achieved. By supplying electrons by LWFA that stream in opposite direction against another laser pulse the scattering of laser by LWFA electrons yields upshifted backscattered photons of γ- and X-ray regimes though the laser Compton scattering [229,230,244,245]. In the laser Compton scattering process we note that the high-energy electrons that propagate at the ultrarelativistic energies with the Lorentz factor $\gamma \gg 1$ may be considered a medium in which the electrostatic and magnetic Lorentz force nearly compensate each other so that they are behaving similarly to plasma (*i.e.* $|\boldsymbol{E} + \boldsymbol{v} \times \boldsymbol{B}/c| = E/\gamma^2 \ll E$). Because the nearly total compensation of this space charge force in plasma we are allowed to explore relatively high-density regime of LWFA at such densities as $10^{18}\,\mathrm{cm}^{-3}$. In comparison the density of uncompensated electron beam is perhaps typically at $10^{11}\,\mathrm{cm}^{-3}$. So, there exist similarities and differences between the physical processes of LWFA and laser Compton scattering. We will regard it meritorious to discuss these applications to the creation of various radioisotopes through such processes as (γ, n), (γ, p) in some details below.

In addition the γ-beam may be used to hit the K_α-edge of the specific element with high Z. Since the cross-section suddenly rises at the K_α-edge to excite an electron and induce nuclear resonant fluorescence (NRF). If such an element is carried by a vector

drug, this NRF photo signal serves as the specific biological marker, such as a cancer cell. The cross-section of the high-Z element K_α-shell and those of lighter (ordinary) biological elements are lopsided toward the former. Thus a relatively low-dose high-energy γ-photon irradiation has attractive properties: i) the sensitive and site-specific NRF photon signal shows the location of sought after cells (diagnosis); ii) the overall dosage is low, since the high-energy γ-photon cross-section of the elements of biological tissues is small. Such properties may be exploited for a diagnosis of blood cell cancer, for example. The knockout of the inner K_α-shell electron induces the cascade of Auger electron. Such a process has been observed in Ti targeted by X-ray of a synchrotron light source, for example in [246]. If the heavy element carried by the vector drug is irradiated with the γ-beam right above the K_α-edge energy, not only the above NRF photon tells us the presence and location of the cancer cell, but also the subsequent Auger electron emissions should kill the adjacent cancer cell. This should be an Auger therapy *par excellence*.

Further applications of intense laser-generated radiative beams to medicine include that of laser-driven ions. For example, laser driven proton beams, though not yet achieved to be of the quality for use in real applications, have been considered for future use for radio-oncology therapy machines, as they can be quite compact and other advantages [29, 247]. This topic is also well covered in the above recent book [243] and perhaps not much further review here is necessary. Here we wish to point out, as we commented in sect. **5** in general and sect. **5**˙3 in particular, that the laser-driven proton acceleration already yields more than enough energies of protons for such purposes. These laser-driven proton beams (on the order of 20 MeV) can induce nuclear reactions to produce various short-lived radioisotopes for medical relevance. Simultaneously their compactness of laser acceleration helps to deliver onsite production coping for their fast decay. These include the following isotopes: ^{15}O (produced from nitrogen) has the decay time so short (a few minutes) appropriate for the cardiovascular diagnosis; ^{11}C produced from ^{14}N via (p,α); ^{13}N from ^{16}O via (p,α) (both of them decay in or less than 20 min) for molecular imaging and systemic radiotherapy; $^{99\mathrm{m}}$Te from ^{99}Mo via (p,n) (decaying in 6 hours); ^{67}Cu produced from ^{70}Zn via (p,α) (decaying in 2.5 days), suggesting respective differentiated applications of diagnosis, therapy, and nuclear pharmacology [248, 249]. (For the physiological speed needed for short radio-decay times the peptide carriers may be suited for these radioisotopes).

These can also induce secondary reactions [250], which can produce neutrons, for example. These are produced through nuclear processes such as the (n,p), (n,γ), and xn processes. In some of these categories of applications, it matters that the laser-driven processes can be much more compact in comparison with the conventional technology. Thus, when it comes to producing some radioactive isotopes, for example, those that are extremely short lived, they need to be produced in the vicinity of each needing hospital. A typical case may be the generation of ^{64}Cu, ^{67}Cu (having a decay time of a few days) from ^{64}Zn, ^{67}Zn through the (n,p) processes [251, 252].

Accelerated proton beams by laser as discussed in sect. **5** can also play an important role to produce interesting (p,n) processes, which can also produce a host of isotopes of medical use. An excellent review may be found in [253]. These include ^{14}O, ^{89}Zr, ^{64}Cu. In these (n,p), (p,n), (γ,p), and (p,γ) processes the end products are chemically distinct from the start materials so that the separation of the products from the original is easier, as compared to such processes as (γ,n) and (n,γ), etc. Those that involve β- and α-decay are also convenient, either as the primary or secondary process. In particular when some of these products of radioisotopes are appropriately short-lived, these may become ideal

substances for nuclear medicine and pharmacology to detect particular tissues such as cancer cells directed by a vector drug, and may be conveniently washed away after their radioactivity becomes decayed away after the short half lifetime. Such fast decaying radioisotopes may not be carried from the production site quickly enough to the necessary clinics (for example). Here the compactness of our technology based on laser may have crucial advantages over the conventional methods, such as conventional accelerator and nuclear reactors. Furthermore, such short-lived, vector-drug directed radioisotopes may decay where the target tumor may reside (or its neighborhood). If the decay products have a relatively short range (such as α and β), they act as a tumor-killing therapy tool on the very target that has been identified by the diagnosing emission signal, *i.e.* diagnoses and killings in a tight combination. This is sometimes called theranostics [248, 249]. A recent progress in employing nanoparticle loading on a molecular cluster that may be delivered to tumor cells is also worth noting [254]. For a recent review book on these subjects, see for example [253]. In the following we concentrate on the γ-induced photonuclear reactions and their nuclear medicine applications [255, 256].

In addition to the medical applications, diagnostic (and further secondary irradiation) applications of laser-driven radiation and accelerated particle beams on industrial materials are to become available.

9˙2. *Medical radioisotopes with high specific activity produced in photonuclear reactions.* – The laser-driven γ beams are spurring the possible clinical usage of a novel class of radioisotopes that are very useful for nuclear medicine but are not easy to obtain otherwise. These radioisotopes may be delivered to specific cells/DNA/proteins/peptides of the tumor with a specific vector drug, where cancer cells may be killed by their radioactivity. This method is not hampered by the beam scattering of ion therapy mentioned in sect. **9˙1.** nor restricted by non-metastasis, which are the general limitations of electron beam radiation therapy.

In a new development the intense, high-repetition-rate, diode pumped lasers in combination with intense, brilliant, relativistic electron beams allow to produce very intense, brilliant γ beams via Compton backscattering. There are several existing or planned laser Compton γ-ray facilities around the world, including: HIγS [257], NewSUBARU [258], MEGa-ray [221, 228], ELI-NP [255, 256], and ERL-LCS [227]. For example, the MEGa-ray at LLNL has realized γ beams, which have order(s) of magnitude higher flux than the existing γ beams, which allows to produce many new medical radioisotopes for diagnostics and therapy. The new γ beams will also have a much smaller band width $\Delta E\gamma/E\gamma$, allowing to address individual nuclear levels with strong population. Here, on the one hand, by (γ, γ') photoexcitation new nuclear isomers can be produced, which decay frequently by many conversion and Auger electrons, allowing for a short-range killing of tumor cells in the surrounding 10–200 μm range after they have been transported to the overexpressed acceptors of the cancer cells. But also by $(\gamma, x\mathrm{n} + y\mathrm{p})$ photonuclear reactions many new medical radioisotopes can be produced. We will discuss in detail many new specific radioisotopes. As an example we here want to mention so-called "matched" pairs for diagnostics and therapy of the same chemical element. Here pairs like: ^{44}Sc/^{47}Sc, ^{61}Cu or ^{64}Cu/^{67}Cu, ^{86}Y/^{90}Y, ^{123}I or ^{124}I/^{131}I or ^{152}Tb/^{149}Tb or ^{161}Tb, where one of the isotopes was so far difficult to produce by classical methods, are of special interest. Here the basic idea is to use bioconjugates [259] that show a high affinity and selectivity to bind to peptide receptors or antigens, that are overexpressed on certain cancer cells compared to normal cells. These therapies are called Peptide Receptor Radio Therapy (PRRT), when peptides are used as bioconjugates or radioimmunother-

apy (RIT), when antibodies are used. This therapy allows to fight diseases, which are not localized or cancer types with multiple metastasis. Once the suitable radioisotopes have been produced, the main task stays with radiochemistry and radiopharmaceutics to build the proper bioconjugates to reach the cancer cells in the optimum way. While we are pushing for the treatment of very small tumors in laser-driven ion therapy, with the new therapeutic medical radioisiotopes one is going for shorter-range emitted radiation (α particles, low-energy electrons) killing only cancer cells and cancer stem cells in the immediate surrounding, where the bioconjugate was delivered.

9˙3. *Presently used nuclear reactions to produce medical radioisotopes.* – Today the most frequently employed nuclear reactions for the production of medical radioisotopes are the following.

1) *Neutron capture*

Neutron capture (n,γ) reactions transmute a stable isotope into a radioactive isotope of the same element. High specific activities are obtained, if the (n,γ) cross-section is high and the target is irradiated with a high neutron flux. Neutrons most useful for (n,γ) reactions have energies from meV to keV (thermal and epithermal neutrons) and are provided in the irradiation positions of high flux reactors at flux densities of $10^{14}\,\mathrm{n/(cm^2 s)}$ up to few $10^{15}\,\mathrm{n/(cm^2 s)}$. If the neutron capture cross-section is sufficiently high (*e.g.* 2100 barn for $^{176}\mathrm{Lu}(\mathrm{n},\gamma)^{177}\mathrm{Lu}$), then a good fraction of the target atoms can be transmuted to the desired product isotopes, resulting in a product of high specific activity.

2) *Nuclear fission*

Fission is another process used for isotope production in nuclear reactors. Radiochemical separation leads to radioisotopes of "non-carrier-added" quality, with specific activity close to the theoretical maximum. Fission is the dominant production route for the generator isotopes ^{99}Mo and ^{90}Sr, for the β^- emitting therapy isotope ^{131}I and for the SPECT (single-photon emission computed tomography) isotope ^{133}Xe.

3) *Charged particle reactions with p, d or α ions*

Imaging for diagnostic purposes requires either β^+ emitters for PET (mainly ^{18}F, ^{11}C, ^{13}N, ^{15}O, ^{124}I, or ^{64}Cu), or isotopes emitting gamma-rays with suitable energy for SPECT (about 70 to 300 keV), if possible without $\beta^{+/-}$ emission to minimize the dose to the patient. Thus electron capture decay is preferred for such applications, *e.g.*: ^{67}Ga, ^{111}In, ^{123}I, ^{201}Tl. Usually these neutron-deficient isotopes cannot be produced by neutron capture on a stable isotope (except for ^{64}Cu). Instead, they are mainly produced by charged-particle induced reactions such as (p,n), $(\mathrm{p},2\mathrm{n})$, ... High specific activities of the final product are achievable, if the product differs in chemical properties from the target (*i.e.* different Z) and can be chemically separated from the remaining bulk of target material. Thus Z must be changed in the nuclear reaction, *e.g.* in (p,n), $(\mathrm{p},2\mathrm{n})$, (p,α) reactions. The energies of the charged particle beams for such reactions are usually in the range of 10 to 30 MeV and can be supplied with high currents (0.1 to 1 mA) by small cyclotrons.

4) *Generators*

Another important technique is the use of generators, where short-lived radionuclides are extracted "on-tap" from longer-lived mother nuclides. Here the primary radioisotope

(that was produced in the nuclear reaction) has a longer half-life than the final radioisotope (that is populated by decay of the primary radioisotope and is used in the medical application). The primary radioisotope is loaded onto the generator and stays there chemically fixed. The final radioisotope will grow in and can be repetitively extracted and used.

5) *Photonuclear reactions*

The inverse process to (n, γ), namely (γ, n), also allows producing neutron-deficient isotopes, but conventional γ ray sources do not provide sufficient flux density for efficient production of radioisotopes with high total activity and high specific activity. Therefore, this process played no role until now.

9˙4. *Specific radioisotopes produced in photonuclear reactions*. – We now focus to discuss the different γ-induced reactions and specific radioisotopes that may be produced by photonuclear reactions, that are enabled by the aforementioned breakthroughs of brilliant γ beam technology in the item 5 above. In [256] we reviewed a broad list of producible radio-isotopes by this method. For example, Ra^{225} may be created from Ra^{226} by γ-beam irradiation through the (γ, n) process. This radioisotope has a lifetime of ~ 15 days by the $\beta =$ decay into Ac^{225}, which quickly α-decays. Thus the decay times of Ra^{225} and of its decay product Ac^{225} are short enough for a very useful radioactive marker if attached to a vector drug, which might seek cancer cells. Because of the short lifetime, the signal is significant, while it decays away to be innocuous, as far as radioactivity is concerned shortly after. Thus it may serve as a good diagnostic material. Furthermore, since this decays with the emission of an α-particle whose mean free path is short, it can kill an adjacent cancer cell, serving as a candidate among the group of isotopes that act as a dual marker-killer (with a cancer-seeking vector drug). See in sect. **9˙**4.1 item 2 for Ra^{225} and Ac^{225}. This example of Ra^{225} is not alone and we may find various such appropriate radioisotopes for various different applications [260].

For the sake of dual marker-killer approaches of targeted cells, we should point out the use of laser Compton γ-photon itself irradiating a tissue that contains a high-Z element (that need not be radioactive) carried by a vector drug. By tuning to the energy slightly above the high-Z element's K_α-shell energy level, the γ-photon induces the inner-shell electron ionization and thus a nuclear fluorescence signal (a marker function). It is fairly well known that such inner-shell electron excitation induces multiples of cascade Auger electron emissions, These electrons with short mean free paths serve as a convenient "killer" mechanism to the adjacent cells.

With a bandwidth of 10^{-3}, this results at 10 MeV in a spectral flux density of $10^{14}\,\gamma/(\mathrm{cm}^2\,\mathrm{s\,eV})$. With γ lenses the beam cross-section could be improved by 10^4 and a better bandwidth is expected. We compare these to thin-target yields obtained by thermal neutron capture at a typical flux density of $10^{14}\,\mathrm{n}/(\mathrm{cm}^2\,\mathrm{s})$ in high-flux reactors. Note that like for the potential beam parameters of γ beam facilities, there is also a wide range of flux densities available at the irradiation positions of high-flux reactors. Some positions provide flux densities of several 10^{12} to $10^{13}\,\mathrm{n}/(\mathrm{cm}^2\,\mathrm{s})$, while few special reactors have positions that even exceed $10^{15}\,\mathrm{n}/(\mathrm{cm}^2\,\mathrm{s})$, namely SM3 in Dimitrovgrad [261], HFIR in Oak Ridge [262] and the ILL's high-flux reactor in Grenoble. Since hitherto no γ beams with sufficiently small bandwidth were available to exploit resonant excitation, there are obviously no such measured cross-sections. Presently, we can only estimate a lower bound using the averaged cross-sections measured at bremsstrahlung facilities [263-265]. For cases where no measured cross-sections are available, we interpolate experimental

cross-sections of the same reaction channel on nearby elements, taking into account the energy above the reaction threshold. We have submitted a proposal to the HIγS facility to measure the expected strong resonant gateway states for radioisotope production, which frequently can be predicted from known neighboring nuclei.

Even when using conservative assumptions, the estimated specific activities are promising for specific isotopes. The total radioisotope activity achievable in a nuclear reactor can be relatively high since, thick (several cm) and large (several cm^2) targets can be used if the cross-sections are not too high (leading to self-absorption and local flux depression). Multiple irradiation positions allow producing various radioisotopes with activities of many TBq.

For the γ beam we estimate the total activities by integrating to one interaction length, *i.e.*, where the initial γ-beam intensity has dropped to $1/e = 37\%$ of its intensity. Higher total activities can be achieved with thicker targets at the expense of lower specific activity and vice versa. The total interaction cross-section is usually dominated by the atomic processes of Compton effect and pair creation, but not for γ beams with very small bandwidth. We conservatively consider any γ-ray as lost after interaction. In reality, part of the Compton scattering goes forward under small angles and the γ-rays that have lost little energy can still induce photonuclear reactions. The usable target thickness ranges from $20\,\mathrm{g/cm}^2$ for heavy elements to $40\,\mathrm{g/cm}^2$ for light elements, *i.e.*, in total only few mg target material are exposed to the small area of the γ beam. With nonresonant reactions of the order of 0.1 TBq activity can be produced per day, corresponding to tens (for β^- therapy isotopes) to thousands (for imaging isotopes and therapy with alpha emitters) of patient doses.

9˙4.1. Radioisotopes via the (γ, n) reaction. When excited well beyond the neutron binding energy, a nucleus readily loses a neutron. Competing reactions such as de-excitation by gamma ray emission are far less probable.

1) ^{99}Mo/^{99m}Tc: The presently most used radioisotope for nuclear medicine studies is ^{99m}Tc. Its 140 keV γ-ray is ideal for SPECT imaging. With a relatively short half-life of 6 h and the quasi-absence of beta particles, the radiation dose to the patient is sufficiently low. ^{99m}Tc is conveniently eluted in non-carrier-added quality from simple and reliable ^{99}Mo ($T_{1/2} = 66\,\mathrm{h}$) generators that can be used for about one week. Various technetium compounds have been developed for a multitude of nuclear medicine applications [259]. The combination of these advantages explains why ^{99m}Tc is used in about 80% of all nuclear-medicine studies. Until recently five nuclear reactors were used to produce about 95% of the world needs of ^{99}Mo by neutron-induced fission of highly enriched ^{235}U targets. Recently the two reactors that used to produce the majority of the ^{99}Mo supply had extended shutdowns, leading to a serious ^{99}Mo/^{99m}Tc supply crisis [266, 267]. A facility providing $10^{15}\,\gamma$/s could produce via $^{100}\mathrm{Mo}(\gamma, \mathrm{n})$ reactions several TBq per week. Since the present request is 3000 TBq per week, many such facilities would be required to assure the worldwide ^{99}Mo supply.

This example demonstrates that the new production method by γ beams is not intended to compete with large-scale production of established isotopes. The advantage of γ beams for radioisotope production lies clearly in the very high specific activity that can be achieved for radioisotopes or isomers that are very promising for nuclear medicine, but that are presently not available in the required quality or quantity.

2) ^{225}Ra/^{225}Ac: Alpha emitters are very promising for therapeutic applications, since the emitted alphas deposit their energy very locally (typical range of one to few cancer cell diameters) with high linear energy transfer (LET) and, hence, high probability for

irreparable double strand breaks. An alpha emitter coupled to a cancer cell specific bioconjugate can be used for targeted alpha therapy to treat disseminated cancer types (leukemia), micro-metastases of various cancers or to destroy chemo- and radiation-resistant cancer cells (*e.g.*, glioblastoma). One promising alpha emitter is ^{225}Ac ($T_{1/2} =$ 10 days) that decays by a series of four alpha decays and two beta decays to ^{209}Bi. These radioisotopes have been discussed already.

3) ^{169}Er: ^{169}Er decays with 9.4 days half-life by low-energy beta emission (100 keV average beta energy). These betas have a range of 100 to 200 μm in biological tissue, corresponding to few cell diameters. The short beta range makes this isotope very interesting for targeted radiotherapy [268].

4) ^{165}Er: ^{165}Er is one example for an isotope that decays mainly by low-energy Auger electrons. Their range is shorter than one cell diameter. Hence, these Auger emitters have to enter the cell and approach the cell's nucleus to damage the DNA and destroy a cell. Coupled to a bioconjugate that is selectively internalized into cancer cells it can enhance the ratio for dose equivalent delivered to the tumor cell with respect to normal cells. This should result in an improved tumor treatment with less side effects.

5) ^{47}Sc: ^{47}Sc is a promising low-energy beta emitter for targeted radiotherapy. Scandium is the lightest rare-earth element. Most established labeling procedures for valence III metals (Y, Lu, ...) can be applied directly for Sc. Its 159 keV gamma line allows imaging of ^{47}Sc distribution by SPECT or gamma cameras. Alternatively, the β^+ emitting scandium isotope ^{44}Sc can be used for PET imaging as a "matched pair". Carrier-free ^{47}Sc can be produced by ^{50}Ti(p, α) or ^{47}Ti($\mathrm{n_{fast}}$, p) reactions followed by chemical separation. The alternative production via ^{46}Ca(n, γ)^{47}Ca $\rightarrow$ ^{47}Sc is uneconomic due to the extremely low natural abundance of ^{46}Ca.

6) ^{64}Cu: ^{64}Cu is a relatively long-lived β^+ emitter ($T_{1/2} = 12.7$ h) with various applications in nuclear medicine [269]. ^{64}Cu-ATSM is a way to measure hypoxia of tumors. Hypoxia is an important effect influencing the resistance of tumor cells against chemo- or radiation therapy. ^{64}Cu can also act itself as therapeutic isotope due to its emission of β^- (191 keV mean energy) and low-energy Auger electrons.

7) ^{186}Re: ^{186}Re is a radioisotope suitable for bone pain palliation, radiosynovectomy and targeted radionuclide therapy. Rhenium is chemically very similar to its homologue technetium, thus known compounds that have been developed for imaging with ^{99m}Tc can also be labeled with ^{186}Re and used for therapy. ^{186}Re is currently either produced by neutron capture on ^{185}Re, resulting in limited specific activity, or by ^{186}W(p, n) reactions followed by chemical Re/W separation. Enriched ^{187}Re targets should be used to minimize contamination of the product with long-lived ^{184,184m}Re by ^{185}Re(γ, n) reactions.

9˙4.2. Radioisotopes via the (γ, p) reaction. Even when excited beyond the proton binding energy, a nucleus does not necessarily lose a proton. The latter is bound by the Coulomb barrier, leading to a suppression of the proton loss channel. Only for an excitation well beyond the proton binding energy, the proton gains enough kinetic energy for tunneling efficiently through the Coulomb barrier. However, such excitation energies are usually also above the neutron binding energy or even the two-neutron binding energy. Hence neutron emission competes with proton emission and the cross-sections for (γ, p) reactions may be one order of magnitude lower than the competing channels. Thus, the achievable specific activity (specific activity with respect to the target mass) is limited for (γ, p) reactions. However, the product isotope differs chemically from the target since it has one proton less ($Z_{\mathrm{product}} = Z_{\mathrm{target}} - 1$). After irradiation, a chemical separation of the

product isotope from the target can be performed, ultimately resulting in a high specific activity that is only compromised by competing reactions leading to other isotopes of the product element (such as (γ, np), $(\gamma, 2\mathrm{n})\mathrm{EC}/\beta^+$, etc.) or product burn-up by (γ, n).

– ^{47}Sc: Besides the $^{48}\mathrm{Ca}(\gamma, \mathrm{n})^{47}\mathrm{Ca} \to {}^{47}\mathrm{Sc}$ reaction, ^{47}Sc can also be produced via the $^{48}\mathrm{Ti}(\gamma, \mathrm{p})\ ^{47}\mathrm{Sc}$ reaction. The established Sc/Ti separation schemes can be employed for the chemical processing. Compared to the $^{47}\mathrm{Ti}(\mathrm{n}, \mathrm{p})$ way here the direct production of disturbing long-lived ^{46}Sc (via $^{46}\mathrm{Ti}(\mathrm{n}, \mathrm{p})$ or $^{47}\mathrm{Ti}(\gamma, \mathrm{p})$, respectively) can be limited more easily, since ^{48}Ti is the most abundant titanium isotope and can be enriched more easily to high abundance. However, the irradiation times have to be kept relatively short to prevent excessive formation of ^{46}Sc impurity by $^{47}\mathrm{Sc}(\gamma, \mathrm{n})$ reactions.

– ^{67}Cu: ^{67}Cu is also a promising beta-emitter for targeted radiotherapy. Alike ^{47}Sc it has a sufficiently long half-life for accumulation in the tumor cells when bound to antibodies and its 185 keV gamma ray allows imaging with SPECT or gamma cameras. Together with the PET imaging isotopes ^{61}Cu or ^{64}Cu, it forms a "matched pair". The usual production routes $^{68}\mathrm{Zn}(\mathrm{p}, 2\mathrm{p})$, $^{70}\mathrm{Zn}(\mathrm{p}, \alpha)$, or $^{64}\mathrm{Ni}(\alpha, \mathrm{p})$ are all characterized by low yields. The former requires energetic protons ($\gg 30$ MeV from larger cyclotrons) and the latter two methods use expensive enriched targets with low natural abundances.

– Isotopes with higher Z: In principle, also heavier β^- emitters used for radionuclide therapy such as ^{131}I, ^{161}Tb or ^{177}Lu could be produced by (γ, p) reactions (on ^{132}Xe, ^{162}Dy or ^{178}Hf targets respectively).

Even though we have presented only a tip of an iceberg of medical applications of intense laser (and in particular that of nuclear photonics), the reader should see that there is a vast arena of the convergence of medicine and laser emerging. Perhaps the convergence will not be limited between medicine and laser, but still broader fields that include nuclear physics, biochemical, and nanomaterial sciences will be converging to form an exciting frontier. We refer the reader to recent books such as [243, 260] for additional glimpse into the latest developments in such fields.

10. – Conclusions

The laser wakefield acceleration introduced several fundamentally novel philosophies and principles in both accelerator physics and plasma physics, as described in sect. **1**. Some of the principles such as the employment of an already broken material of plasma as a medium was inherited from the bold research by such pioneers as Veksler and Rostoker, while ameliorating the instabilities arising in plasmas by the principle of high phase velocity and that of a fs ultrafast laser driver. The other pillars of this philosophy such as the resonance of the eigenmodes and the relativistic coherence reinforced the large accelerating gradient and its coherent maintenance. It amounted to a bold step forward to climb the ever higher frequency of the driving electromagnetic wave from the RF range to the optical laser range some several orders by a single stroke. As we have seen in sects. **2** and **6**, we are about to witness another quantum jump by several orders in the driver's frequency from optical laser to X-ray laser.

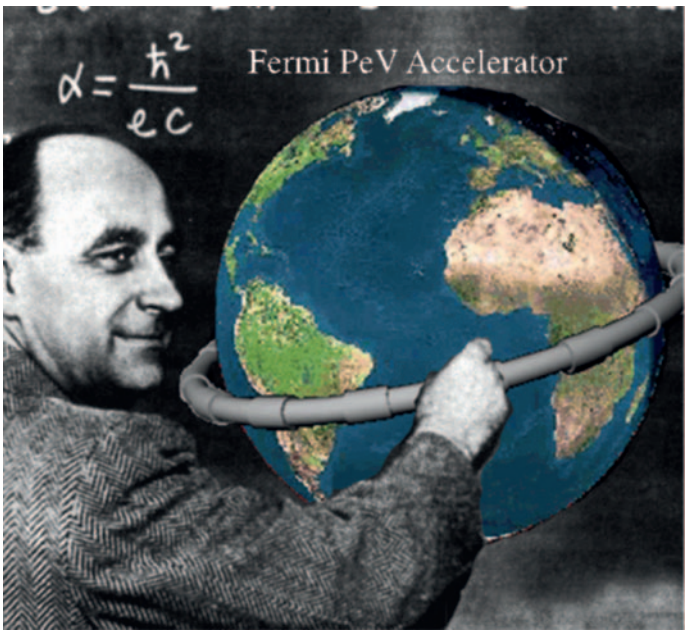

Fig. 24. – Fermi's PeV vision.

10·1. *The Higgs energy and Fermi's PeV*. – Since the LWFA energy gain scales as n_{cr}/n_e (as defined in sect. **3**), we have envisioned [93] that one way to increase the achievable electron energies in LWFA is to decrease the electron density. As shown in sect. **3**, this brings in two consequences: i) to increase the laser pulse energy, as the laser energy increases in proportion to the laser occupation volume; ii) the consequencial lengthening of the acceleration distance. The first issue is more serious, as the energy increase of high-intensity laser increases the cost roughly proportional to the laser energy. One of our suggestions has been thus to utilize the world's large energy lasers such as LMJ, NIF, LLE, SIOM, and GSI [270], which have been prepared for other purposes already, but with appropriate compression they can become applicable for the present purpose. The initiative by the IZEST (International Center for Zetta- Exawatt Science and Technology) to promote such utilization, planning, and collaboration is noteworthy [270]. It is also quite helpful that the world high-intensity laser organization ICUIL coordinates such worldwide efforts [271]. These activities have arisen because the utilization of such large-energy lasers requires a coordinated effort and substantial administrative and financial commitment and vision. We look forward to seeing some bold step forward in this direction.

In the use of a large energy laser (such as at LMJ) in a low-density plasma, we realize that even though typically such a laser has a very low rep rate, we may be able to conduct an invaluable experiment that does not depend on high rep rate and high luminosity. As is popularly known, Fermi boldly suggested an ultimate acceleration at PeV (see fig. 24), which girdles the entire Earth [109]. We take up Fermi's challenge here with LWFA. As analyzed [113], LWFA with a MJ laser allows us to obtain PeV over O (2 km). Unique experiments not dependent on high luminosity at a very high energy may be designed such as the graininess of the vacuum due to a "superstring theoretic"

effect (sect. **4**). In addition the usage of high-intensity and/or high-fluence lasers to make frontier physics discoveries has been considered (see sect. **6**). These include the exploring of dark matter by studying the interference of photons with new particles (four-wave mixing with lasers) [265] originally used in [149]. It may be also possible to pick up neutrinos by laser [266] (originally used in [150]). Moreover, recently the suggestion of a possible "fifth force", showing an exotic decay (mediated by an unknown particle) [267] for the discovered anomaly [268] of the excited state of ^{8}Be, has been made. This provides us an intriguing challenge if laser Compton gamma photons (as discussed in sect. **8**) provide an interesting path (which may be an inverse process) to check such a suggestion [267]. How would Fermi respond to these novel and daring endeavors that LWFA and its stimulated laser technology have brought up?

Meanwhile, we find that wakefield mechanism is at work in the Mother Nature. Most significantly in the jets of AGN [180]. This mechanism is provided by the accretion disk instability triggering a natural large amplitude coherent disturbance on the jets, which creates a very large energy gain of particles, both ions and electrons. The former should give rise to ultrahigh-energy cosmic rays that can go beyond 10^{19} eV, beyond which the venerable Fermi's stochastic acceleration would lose energies even for protons. The latter should manifest as the phenomenon of blazar gamma emissions.

10˙2. *CAN laser and its applications.* – Most of the current requests for high-energy accelerators are that of a collier (as we discussed in sect. **2** and alternatives mentioned in sect. **4**), in which high luminosity is one of the important requirements along with the beam energy [41]. This realization led to recommendations compiled under the Joint Task Force of the ICUIL-ICFA on Laser Acceleration launched between ICUIL and ICFA [271] and resulted in a final report published in [42]. In this report it is pointed out that the most important (and not fulfilled by the current high-intensity laser technology) is the lack of high rep rate and accompanying low efficiency. In response to this challenge [40] came up with an innovative adoption of high rep rate and high-efficiency fiber laser technology (albeit lacking the ability to achieve high intensity), turning fiber lasers into high intensity by coherent stacking of fibers, called CAN (Coherent Amplification Network). This new technology (promoted by the consortium headed by IZEST in France, including a consortium member of CERN) has been developed by organizations such as Ecole Polytechnique, Thales, U. of Southhampton. If and when such a technology is realized in its full capacity, as predicted in [40], an immense spectrum of applications should be supported in addition to a laser collider. This is because most of the societal applications including medical ones typically need the high rep rate characteristics. Because of this breakthrough, CAN is expected to play a major role in expanding intense laser applications.

10˙3. *New compression technique and ELI prospect.* – A novel laser compression technique that may permit even a single-cycled optical laser pulse has been invented [37]. As has been discussed in sects. **2** and **6**, this technique shown in a proof-of-principle experiment at the ELI-NP site [272]. The reduction of an ultrafast laser pulse (tens of fs) into a single-cycled optical laser pulse is a very significant step. This is because a single-cycled laser pulse has the unique property that the ponderomotive force has not compensated its amplitude and possesses a more direct and coherent structure. These, of course, enhance the efficiency and magnitude of the laser acceleration. At the optical frequency such as laser pulse, it has been shown in sect. **5**, that SCLA (Single-Cycled Laser Acceleration) is very effective and yielding high-quality laser accelerated beams of

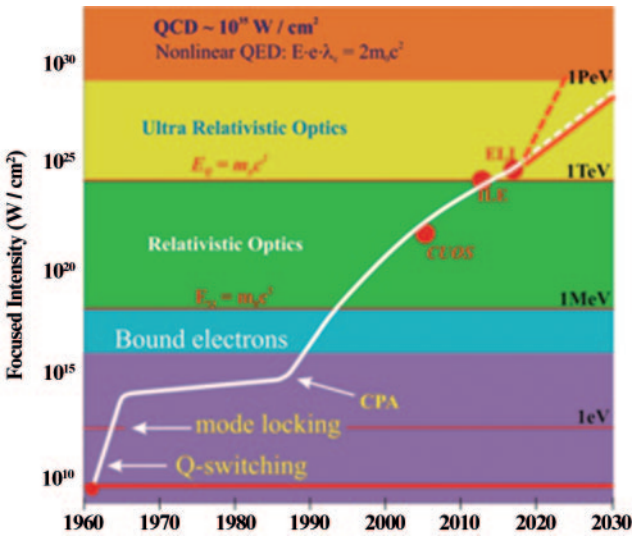

Fig. 25. – The laser intensity in the years. A shortcut (dotted red line) toward EW and ultrahigh intensities. (After [142] with revisions.)

ions. If we apply this technique to a PW laser, we estimate that a resultant laser with TFC and the relativistic mirror would be in an unprecedented regime of parameters. At ELI-NP where a 10 PW laser will be installed in a couple of years, the consideration is ongoing to pulse-compress a 10 PW laser into an EW X-ray laser.

For one thing, such a pulse may be generated via the TFC on a compact setup. Thus this serves as a table-top compact ion accelerator that may be employed for uses in nuclear medicine (some of which have been discussed in sect. **9**), nuclear pharmacology, and other societal applications.

10˙4. *"TeV on a chip"*. – The invention of the TFC combined with the relativistic mirror brings us a new powerful tool of X-rays, a single-cycled intense X-ray laser, as discussed in sects. **2** and **6**. The scaling of LWFA (discussed in sect. **3**) dictates that with high-energy X-ray photons the critical density increases by many orders of magnitude, allowing us to take even solid density electrons as an accelerating medium (nanostructured materials, for example) [45, 273]. The adoption of nanostructured materials is a creative integration of i) high density (solid density) media for LWFA and ii) an evacuated hole for accelerated particle that also focuses wakefields [152]. Of course, such a radical concept needs to be tested in experimental investigations. Of particular importance is the realization of the X-ray laser driver.

10˙5. *New frontiers: Exawatts and zeptoseconds*. – The introduction of the idea of LWFA [3] and the advent of the CPA [38] reinforced each other to usher in high-field science [6, 39, 143]. Now we envision that these two fundamental ideas are even more intertwined and opening a new accelerated progress. For example, the ever-increasing laser intensity as seen in fig. 25 may rise even faster, as these two powerful ideas generate even more and newer applications. Previously, the path toward EW seems to take ever higher energy of laser such as MJ lasers. Now a new vista appears to arise with the new compression technique and its application to new accelerating media for LWFA.

These new tools are so new that we cannot foresee their full implications. However, we could make a tentative but bold anticipation. For example, the zeptosecond X-ray laser matches very well with nuclear physics, while fs fits well chemistry and atomic physics investigations. We also anticipate that instead of larger machines and higher energies, these developments tend to strive for shorter machines and more intensity, more compact accelerators and other applications devices. These anticipated tendencies should be also conducive to societally useful applications.

Abbreviations

The acronyms are shown either by their respective spelling or reference.

Section 1

LWFA	(Laser Wakefield Acceleration)
CPA	(Chirped Pulse Amplification)
FCT	(Thin Film Compression)
CCAN	(Coherent Amplification Network)
RMP	(Relativistic Mirror Compression)
EM	(Electromagnetic)
PIC	(Particle-in-Cell)
UHC	(Ultra High Contrast)
TNSA	(Target Normal Sheath Acceleration)
RPA	(Radiation Pressure Acceleration)
CAIL	(Coherent Acceleration of Ions by Laser)
PEM	(Plasma Expansion Model)

Section 2

B	(B-Integral)
CETAL	(Center for Advanced Laser Technology, Bucharest, Romania)
ELI-NP	(Extreme Light Infrastructure-Nuclear Physics)
BELLA	[87]
PVC	(Poly Vinyl Chloride)
PVdC	(Poly Vinylidene Chloride)
GVD	(Group Velocity Dispersion)

Section 3

SMLWFA	(Self-Modulated Laser Wakefield Acceleration)
SIOM	[84]
GIST	[83] (Guanju Institute of Science and Technology)
FACET	[88] (at Stanford Linear Accelerator Center (SLAC))
AWAKE	[89] (at CERN (European Center for Nuclear Research))
CERN SPS	(CERN Super Proton Synchrotron)
SLAC	(Stanford Linear Accelerator Center, Stanford University)
RFS	(Raman Forward Scattering)
PETAL	(laser at LMJ facility in France)
LMJ	(Laser Mega Joule)
SSC	(Superconducting Super Collider)
JTF	(Joint Task Force of the ICUIL-ICFA Collaboration)

ICUIL (International Committee for Ultrahigh Intensity Lasers under IUPAP-International Union for Pure and Applied Physics)
ICFA (International Committee for Future Accelerators under IUPAP)
CAN (Coherent Amplification Network)

Section 4

GRB (gamma Ray Burst)
NIF (National Ignition facility at LNLL)
QED (Quantum Electro Dynamics)
QCD (Quantum Chromo Dynamics)

Section 5

SCLA (Single Cycled Laser Acceleration)
BOA (Break Out Afterburner)

Section 6

OPCPA (Optical Parametric Chirped Pulse Amplification)
RHHG (Relativistic Higher Harmonic Generation)
ATS (Attosecond Tunneling Spectroscopy)
AS (Attosecond Streaking)
EUV (Extreme Ultra Violet)
CM (Center of Mass)

Section 7

UHECR (Ultra High Energy Cosmic Rays)
AGN (Active Galactic Nuclei)
MRT (Magneto Rotational Instability)
LPQPO (Long Period Quasi Periodic Oscillations)
GZK process (Greisen-Zatsepin-Kuzmin process)
UHEγ (Ultra High Energy gamma)
JEM-EUSO (Japanese Experimental Module - Extreme Universe Space Observatory)
ANITA [205]
ARA [206]
ARIANNA [207]
VHE (Very High Energy)
BL Lac (BL Lacertae)
VLBA (Very Long Baseline Array)
BH (Black Hole)

Section 8

EUVL (EUV Lithography)
DUV (Deep Ultra Violet)
LPP (Laser Produced Plasma)
HVM (High Volume Manufacturing)
FEL (Free Electron Laser)
SASE (Self-Amplified Spontaneous Emission)
SRF (Superconducting Radio Frequency)
PPM (Pure Permanent Magnet)
NRF (Nuclear Resonance Fluorescence)

Section 9

HIγS	[257]
New SUBARU	[258]
MEGa-ray	[218]
ELI-NP	[256]
ERL-LCS	[227]
PRRT	(peptide Receptor Radio Therapy)
RIT	(Radio Immuno Therapy)
SPECT	(Single Photon Emission Computed Tomography)
PET	(Positron Emission Tomography)
HFIR	[262]
ILL	(Institute Laue-Langevin, Grenoble)
SM3	[261]
LET	(Linear Energy Transfer)
DNA	(Deoxyribo Nucleic Acid)

Section 10

IZEST	(Institute for Zetta-Exawatt Science and Technology, Ecole Polytechnique)
LLE	(Laboratory for Laser Energetics, University of Rochester)
GSI	[270] (Helmholtz Center for Heavy Ion Research, in collaboration with IZEST (International Center for Zetta-Exawatt Science and Technology))

* * *

The first author (TT) acknowledges his humbled gratefulness for the award of the Enrico Fermi Prize by the Italian Physical Society. He cherishes this honor, particularly because what this work amounts to is standing on the shoulder of Enrico Fermi and extending Fermi's vision. He feels extremely lucky to be able to do so. We would like to thank many pioneers and colleagues who contributed to this long journey of investigations by giving us encouragements, guidance, collaboration, and countless helps, including: K. Abazajian, F. Albert, H. Azechi, C. Barty, S. Barwick, P. Bolton, M. Borghesi, A. Bracco, B. Brocklesby, P. Bucksbaum, S. Bulanov, R. Byer, A. Caldwell, M. Campbell, A. Chao, S. Chu, L. Cifarelli, S. Chattopadhay, P. Chen, C. Cohen-Tannoudji, S. Corde, P. Corkum, J. Dawson†, S. DeSilvestri, T. Ditmire, F. Dollar, M. Downer, T. Ebisuzaki, E. Esarey, T. Esirkepov, R. Falcone, J. Faure, J. Feng, M. Fujiwara, A. Giulietti, G. Gulsen, E. Goulielmakis, D. Habs, D. Hammer, T. Hayakawa, M. Hegelich, B. Holzer, K. Homma, W. Horton, S. Ichimaru, S. Iijima, K. Ishikawa, C. Joshi, T. Juhasz, M. Kando, Y. Kato, T. Katsouleas, I. Kim, Y. Kishimoto, F. Krausz, K. Krushelnick, A. Lankford, J. Leboeuf, W. Leemans, A. L'Huillier, R. Li, A. Litvak, F. Mako, V. Malka, R. Matsumoto, C. Max, P. McKenna, J. Meyer-ter-Vehn, H. Milchberg, K. Mima, S. Mukamel, M. Murnane, N. Naumova, A. Necas, D. Neely, D. Niculae, A. Olinto, T. O'Neil, F. Pegoraro, A. Pirozhkov, R. Rassmann, B. Richter, J. Rosenzweig, N. Rostoker†, R. Ruth, D. Ryutov, A. Salam†, W. Sandner†, J. Schreiber, A. Sergeev, K. Shibata, V. Shiltsev, Y. Shin, Z. Siwy, H. Sobel, M. Spiro, P. Sprangle, A. Suzuki, P. Taborek, T. Tait, Y. Takahashi†, F. Tamonoi, K. Tanaka, M. Teshima, M. Tigner, B. Tromberg, D. Umstadter, C. Wahlstrom, J. Wheeler, U. Wienands, T. Yamazaki, X. Yan, K. Yokoya, N. Zamfir, M. Zepf, X. M. Zhang, J. Zuegel, and E. Zweibel. We have been blessed with excellent students and associates who made very close camaraderie during these

times and exceptional contributions in the formative years, who include: N. Canac, M. Cavenago, L. M. Chen, S. Cheshkov, A. Deng, D. Fisher, J. Koga, T. Kurki-Suonio, A. Mizuta, B. Newberger, M. Ottinger, B. Rau, C. Siders, S. Steinke, D. Strickland, and M. Zhou. Our students D. Farinella and C. Lau made dedicated and careful check of our manuscript. It has been a great honor to get involved with all these colleagues throughout this work, without whom this work would not have been completed. The present work was supported by the Norman Rostoker Fund at UCI. K. Nakajima in this work was supported by the Institute for Basic Science under IBS-R012-D1.

REFERENCES

[1] Panofsky W., "The Evolution of Accelerators and Colliders." [Online]. Available: `http://www.slac.stanford.edu/pubs/beamline/27/1/27-1-panofsky.pdf`.
[2] Tajima T., "Laser acceleration and its future", *Proc. Jpn. Acad. Ser. B*, **86** (2010) 147.
[3] Tajima T. and Dawson J., "Laser electron accelerator", *Phys. Rev. Lett.*, **43** (1979) 267.
[4] Chen P., Dawson J., Huff R. W. and Katsouleas T., "Acceleration of electrons by the interaction of a bunched electron beam with a plasma", *Phys. Rev. Lett.*, **54** (1985) 693.
[5] Caldwell A., Lotov K., Pukhov A. and Simon F., "Proton-driven plasma-wakefield acceleration", *Nat. Phys.*, **5** (2009) 363.
[6] Mourou G. A., Tajima T. and Bulanov S. V., "Optics in the relativistic regime", *Rev. Mod. Phys.*, **78** (2006) 309.
[7] Veksler V. I., "Coherent Principle of Acceleration of Charged Particles", presented at the CERN Symposium on High Energy Acelerators and Pion Physics, CERN, Geneva, Switzerland, 1956, p. 80.
[8] Graybill S. and Uglum J., "Observation of Energetic Ions from a Beam-Generated Plasma", *J. Appl. Phys.*, **41** (1970) 236.
[9] Poukey J. and Rostoker N., "One-dimensional model of relativistic electron beam propagation", *Plasma Phys.*, **13** (1971) 897.
[10] Rostoker N. and Reiser M., "Collective Methods of Acceleration", *Harwood Lond.*, 1979.
[11] Ryutov D. and Stupakov G., "Formation of fast-electron cloud during injection of intense relativistic electron beam into vacuum", *Sov. J. Plasma Phys.*, **2** (1976) 309.
[12] Mako F., "Novel particle and radiation sources and advanced materials", in *The physics of plasma-driven accelerators and accelerator-driven fusion: The Proceedings of Norman Rostoker Memorial Symposium*, Vol. **1721**, AIP, New York (2016) p. 50001.
[13] Mako F., Fisher A., Rostoker N., Tzach D. and Roberson C. W., "Collective Ion Acceleration Controlled by a Gas Gradient", *IEEE Trans. Nucl. Sci.*, **26** (1979) 4199.
[14] Mako F. and Tajima T., "Collective ion acceleration by a reflexing electron beam: Model and scaling", *Phys. Fluids 1958–1988*, **27** (1984) 1815.
[15] Tajima T. and Mako F., "Self-consistent potential for a relativistic magnetized electron beam through a metallic boundary", *Phys. Fluids 1958–1988*, **21** (1978) 1459.
[16] Snavely R. *et al.*, "Intense high-energy proton beams from petawatt-laser irradiation of solids", *Phys. Rev. Lett.*, **85** (2000) 2945.
[17] Clark E. *et al.*, "Energetic heavy-ion and proton generation from ultraintense laser-plasma interactions with solids", *Phys. Rev. Lett.*, **85** (2000) 1654.
[18] Maksimchuk A., Gu S., Flippo K., Umstadter D. and Bychenkov V. Y., "Forward ion acceleration in thin films driven by a high-intensity laser", *Phys. Rev. Lett.*, **84** (2000) 4108.
[19] Mora P., "Plasma expansion into a vacuum", *Phys. Rev. Lett.*, **90** (2003) 185002.
[20] Fuchs J. *et al.*, "Laser-driven proton scaling laws and new paths towards energy increase", *Nat. Phys.*, **2** (2006) 48.

[21] Andreev A. *et al.*, "Fast-ion energy-flux enhancement from ultrathin foils irradiated by intense and high-contrast short laser pulses", *Phys. Rev. Lett.*, **101** (2008) 155002.
[22] Andreev A. *et al.*, "Optimal ion acceleration from ultrathin foils irradiated by a profiled laser pulse of relativistic intensity", *Phys. Plasmas 1994-Present*, **16** (2009) 13103.
[23] Neely D. *et al.*, "Enhanced proton beams from ultrathin targets driven by high contrast laser pulses", *Appl. Phys. Lett.*, **89** (2006) 021502.
[24] Ceccotti T. *et al.*, "Proton acceleration with high-intensity ultrahigh-contrast laser pulses", *Phys. Rev. Lett.*, **99** (2007) 185002.
[25] Esirkepov T., Borghesi M., Bulanov S., Mourou G. and Tajima T., "Highly efficient relativistic-ion generation in the laser-piston regime", *Phys. Rev. Lett.*, **92** (2004) 175003.
[26] Esirkepov T., Yamagiwa M. and Tajima T., "Laser ion-acceleration scaling laws seen in multiparametric particle-in-cell simulations", *Phys. Rev. Lett.*, **96** (2006) 105001.
[27] Matsukado K. *et al.*, "Energetic protons from a few-micron metallic foil evaporated by an intense laser pulse", *Phys. Rev. Lett.*, **91** (2003) 215001.
[28] Yan X. *et al.*, "Generating high-current monoenergetic proton beams by a circularly polarized laser pulse in the phase-stableacceleration regime", *Phys. Rev. Lett.*, **100** (2008) 135003.
[29] Rau B. and Tajima T., "Strongly nonlinear magnetosonic waves and ion acceleration", *Phys. Plasmas 1994-Present*, **5** (1998) 3575.
[30] Henig A. *et al.*, "Radiation-pressure acceleration of ion beams driven by circularly polarized laser pulses", *Phys. Rev. Lett.*, **103** (2009) 245003.
[31] Tajima T., Habs D. and Yan X., "Laser acceleration of ions for radiation therapy", *Rev. Accel. Sci. Technol.*, **2** (2009) 201.
[32] Yan X., Tajima T., Hegelich M., Yin L. and Habs D., "Theory of laser ion acceleration from a foil target of nanometer thickness", *Appl. Phys. B*, **98** (2010) 711.
[33] Passoni M., Tikhonchuk V., Lontano M. and Bychenkov V. Y., "Charge separation effects in solid targets and ion acceleration with a two-temperature electron distribution", *Phys. Rev. E*, **69** (2004) 26411.
[34] Schreiber J. *et al.*, "Analytical model for ion acceleration by high-intensity laser pulses", *Phys. Rev. Lett.*, **97** (2006) 45005.
[35] Steinke S. *et al.*, "Efficient ion acceleration by collective laser-driven electron dynamics with ultra-thin foil targets", *Laser Part. Beams*, **28** (2010) 215.
[36] O'Neil T., "Collisionless damping of an electron plasma wave", *Phys. Fluids*, **8** (1965) 2255.
[37] Mourou G., Mironov S., Khazanov E. and Sergeev A., "Single cycle thin film compressor opening the door to Zeptosecond-Exawatt physics", *Eur. Phys. J. ST*, **223** (2014) 1181.
[38] Strickland D. and Mourou G., "Compression of amplified chirped optical pulses", *Opt. Commun.*, **56** (1985) 219.
[39] Tajima T., Mima K. and Baldis H., *High-Field Science* (Springer) 2000.
[40] Mourou G., Brocklesby B., Tajima T. and Limpert J., "The future is fibre accelerators", *Nat. Photon.*, **7** (2013) 258.
[41] Xie M., Tajima T., Yokoya K. and Chattopadhyay S., "Studies of laser-driven 5 TeV e^+e^- colliders in strong quantum beamstrahlung regime", *AIP Conf. Proc.*, **398** (1997) 233.
[42] Leemans W., Chou W. and Uesaka M., "ICFA Beam Dynamics Newsletter", no. 56, 2011.
[43] Naumova N., Nees J., Sokolov I., Hou B. and Mourou G., "Relativistic generation of isolated attosecond pulses in a λ 3 focal volume", *Phys. Rev. Lett.*, **92** (2004) 63902.
[44] Naumova N., Sokolov I., Nees J., Maksimchuk A., Yanovsky V. and Mourou G., "Attosecond electron bunches", *Phys. Rev. Lett.*, **93** (2004) 195003.
[45] Tajima T., "Laser acceleration in novel media", *Eur. Phys. J. ST*, **223** (2014) 1037.
[46] Mourou G. and Tajima T., "More intense, shorter pulses", *Science*, **331** (2011) 41.

[47] Grischkowsky D. and Balant A., "Optical pulse compression based on enhanced frequency chirping", *Appl. Phys. Lett.*, **41** (1982) 1.
[48] Knox W. *et al.*, "Femtosecond dynamics of resonantly excited excitons in room-temperature GaAs quantum wells", *Phys. Rev. Lett.*, **54** (1985) 1306.
[49] Nisoli M., De Silvestri S. and Svelto O., "Generation of high energy 10 fs pulses by a new pulse compression technique", *Appl. Phys. Lett.*, **68** (1996) 2793.
[50] Nisoli M. *et al.*, "Compression of high-energy laser pulses below 5 fs", *Opt. Lett.*, **22** (1997) 522.
[51] Rolland C. and Corkum P. B., "Compression of high-power optical pulses", *J. Opt. Soc. B*, **5** (1988) 641.
[52] Wheeler J., Mourou G. and Mironov S., "Laser compression by the thin film compression", 2016. (private communication)
[53] Zhou M. *et al.*, "Proton acceleration by single-cycle laser pulses offers a novel monoenergetic and stable operating regime", *Phys. Plasmas 1994-Present*, **23** (2016) 43112.
[54] Potemkin A. K., Khazanov E. A., Martyanov M. A. and Mar'yana S. K., "Compact 300-J/300-GW Frequency-Doubled Neodymium Glass Laser—Part I: Limiting Power by Self-Focusing", *IEEE J. Quantum Electron.*, **45** (2009) 336.
[55] Akhmanov S. A., Vysloukh V. A. and Chirkin A. S., *Optics of femtosecond laser pulses* (Moscow, Nauk) 1988.
[56] Mironov S., Lozhkarev V., Luchinin G., Shaykin A. and Khazanov E., "Suppression of small-scale self-focusing of high-intensity femtosecond radiation", *Appl. Phys. B*, **113** (2013) 147.
[57] Hassan M. T. *et al.*, "Optical attosecond pulses and tracking the nonlinear response of bound electrons", *Nature*, **530** (2016) 66.
[58] Corkum P. and Krausz F., "Attosecond science", *Nat. Phys.*, **3** (2007) 381.
[59] An der Brügge D. and Pukhov A., "Enhanced relativistic harmonics by electron nanobunching", *Phys. Plasmas 1994-Present*, **17** (2010) 33110.
[60] Bulanov S. V., Naumova N. and Pegoraro F., "Interaction of an ultrashort, relativistically strong laser pulse with an overdense plasma", *Phys. Plasmas 1994-Present*, **1** (1994) 745.
[61] Braun A., Korn G., Liu X., Du D., Squier J. and Mourou G., "Self-channeling of high-peak-power femtosecond laser pulses in air", *Opt. Lett.*, **20** (1995) 73.
[62] Tajima T., "High energy laser plasma accelerators", *Laser Part. Beams*, **3** (1985) 351.
[63] Esarey E., Schroeder C. B. and Leemans W. P., "Physics of laser-driven plasma-based electron accelerators", *Rev. Mod. Phys.*, **81** (2009) 1229.
[64] Hamster H., Sullivan A., Gordon S., White W. and Falcone R., "Subpicosecond, electromagnetic pulses from intense laser-plasma interaction", *Phys. Rev. Lett.*, **71** (1993) 2725.
[65] Durfee Iii C. and Milchberg H., "Light pipe for high intensity laser pulses", *Phys. Rev. Lett.*, **71** (1993) 2409.
[66] Nakajima K. *et al.*, "A proof-of-principle experiment of laser wakefield acceleration", *Phys. Scr.*, **1994** (1994) 61.
[67] Nakajima K. *et al.*, "Observation of ultrahigh gradient electron acceleration by a self-modulated intense short laser pulse", *Phys. Rev. Lett.*, **74** (1995) 4428.
[68] Modena A. *et al.*, "Electron acceleration from the breaking of relativistic plasma waves", *Nature*, **377** (1995) 606.
[69] Marques J. *et al.*, "Temporal and spatial measurements of the electron density perturbation produced in the wake of an ultrashort laser pulse", *Phys. Rev. Lett.*, **76** (1996) 3566.
[70] Siders C. *et al.*, "Laser wakefield excitation and measurement by femtosecond longitudinal interferometry", *Phys. Rev. Lett.*, **76** (1996) 3570.
[71] Dewa H. *et al.*, "Experiments of high energy gain laser wakefield acceleration", *Nucl. Instrum. Methods Phys. Res. A*, **410** (1998) 357.

[72] Mangles S. *et al.*, "Monoenergetic beams of relativistic electrons from intense laser–plasma interactions", *Nature*, **431** (2004) 535.
[73] Geddes C. *et al.*, "High-quality electron beams from a laser wakefield accelerator using plasma-channel guiding", *Nature*, **431** (2004) 538.
[74] Faure J. *et al.*, "A laser–plasma accelerator producing monoenergetic electron beams", *Nature*, **431** (2004) 541.
[75] Geddes C. *et al.*, "Production of high-quality electron bunches by dephasing and beam loading in channeled and unchanneled laser plasma accelerators", *Phys. Plasmas 1994-Present*, **12** (2005) 56709.
[76] Leemans W. *et al.*, "GeV electron beams from a centimetre-scale accelerator", *Nat. Phys.*, **2** (2006) 696.
[77] Faure J., Rechatin C., Norlin A., Lifschitz A., Glinec Y. and Malka V., "Controlled injection and acceleration of electrons in plasma wakefields by colliding laser pulses", *Nature*, **444** (2006) 737.
[78] Matlis N. H. *et al.*, "Snapshots of laser wakefields", *Nat. Phys.*, **2** (2006) 749.
[79] Hafz N. A. *et al.*, "Stable generation of GeV-class electron beams from self-guided laser–plasma channels", *Nat. Photon.*, **2** (2008) 571.
[80] Buck A. *et al.*, "Real-time observation of laser-driven electron acceleration", *Nat. Phys.*, **7** (2011) 543.
[81] Liu J. *et al.*, "All-optical cascaded laser wakefield accelerator using ionization-induced injection", *Phys. Rev. Lett.*, **107** (2011) 35001.
[82] Pollock B. *et al.*, "Demonstration of a narrow energy spread, 0.5 GeV electron beam from a two-stage laser wakefield accelerator", *Phys. Rev. Lett.*, **107** (2011) 45001.
[83] Kim H. T. *et al.*, "Enhancement of electron energy to the multi-GeV regime by a dual-stage laser-wakefield accelerator pumped by petawatt laser pulses", *Phys. Rev. Lett.*, **111** (2013) 165002.
[84] Lu H. *et al.*, "Laser wakefield acceleration of electron beams beyond 1 GeV from an ablative capillary discharge waveguide", *Appl. Phys. Lett.*, **99** (2011) 91502.
[85] Wang X. *et al.*, "Quasi-monoenergetic laser-plasma acceleration of electrons to 2 GeV", *Nat. Commun.*, **4** (2013) 1988.
[86] Leemans W. *et al.*, "Multi-GeV electron beams from capillary-discharge-guided subpetawatt laser pulses in the self-trapping regime", *Phys. Rev. Lett.*, **113** (2014) 245002.
[87] "BELLA - Berkeley Lab Laser Accelerator." [Online]. Available: `http://bella.lbl.gov/`.
[88] "SLAC - Stanford Linear Accelerator." [Online]. Available: `https://www6.slac.stanford.edu/`.
[89] "AWAKE - Advanced Wakefield Experiment." [Online]. Available: `http://awake.web.cern.ch/awake/`.
[90] Mourou G., "Laser Particle Physics Paradigm", Proposal for ERC-2013-SyG - Synergy Grant - Proposal no. 610036 LP3." 2013.
[91] Kostyukov I., Pukhov A. and Kiselev S., "Phenomenological theory of laser-plasma interaction in 'bubble' regime", *Phys. Plasmas 1994-Present*, **11** (2004) 5256.
[92] Lu W., Huang C., Zhou M., Mori W. and Katsouleas T., "Nonlinear theory for relativistic plasma wakefields in the blowout regime", *Phys. Rev. Lett.*, **96** (2006) 165002.
[93] Nakajima K. *et al.*, "Operating plasma density issues on large-scale laser-plasma accelerators toward high-energy frontier", *Phys. Rev. ST Accel. Beams*, **14** (2011) 91301.
[94] Nakajima K., Lu H., Zhao X., Shen B., Li R. and Xu Z., "100-GeV large scale laser plasma electron acceleration by a multi-PW laser", *Chin. Opt. Lett.*, **11** (2013) 13501.
[95] Nakajima K., "Laser electron acceleration beyond 100 GeV", *Eur. Phys. J. ST*, **223** (2014) 999.
[96] Nakajima K., "Laser-driven electron beam and radiation sources for basic, medical and industrial sciences", *Proc. Jpn. Acad. Ser. B Phys. Biol. Sci.*, **91** (2015) 223.
[97] Nakajima K., Kim H. T., Jeong T. M. and Nam C. H., "Scaling and design of high-energy laser plasma electron acceleration", *High Power Laser Sci. Eng.*, **3** (2015) e10.

[98] Martins S. F., Fonseca R., Lu W., Mori W. and Silva L., "Exploring laser-wakefield-accelerator regimes for near-term lasers using particle-in-cell simulation in Lorentz-boosted frames", *Nat. Phys.*, **6** (2010) 311.
[99] Kalmykov S. Y. *et al.*, "Dark-current-free petawatt laser-driven wakefield accelerator based on electron self-injection into an expanding plasma bubble", *Plasma Phys. Control. Fusion*, **53** (2010) 14006.
[100] Chen M., Esarey E., Schroeder C., Geddes C. and Leemans W., "Theory of ionization-induced trapping in laser-plasma accelerators", *Phys. Plasmas 1994-Present*, **19** (2012) 33101.
[101] Ren C. *et al.*, "Compressing and focusing a short laser pulse by a thin plasma lens", *Phys. Rev. E*, **63** (2001) 26411.
[102] Volfbeyn P., Esarey E. and Leemans W., "Guiding of laser pulses in plasma channels created by the ignitor-heater technique", *Phys. Plasmas 1994-Present*, **6** (1999) 2269.
[103] Xiao Y.-F. *et al.*, "Efficient generation of extended plasma waveguides with the axicon ignitor-heater scheme", *Phys. Plasmas 1994-Present*, **11** (2004) L21.
[104] Clark T. and Milchberg H., "Time-and space-resolved density evolution of the plasma waveguide", *Phys. Rev. Lett.*, **78** (1997) 2373.
[105] Ditmire T., Shigemori K., Remington B., Estabrook K. and Smith R., "The production of strong blast waves through intense laser irradiation of atomic clusters", *Astrophys. J. Suppl. Ser.*, **127** (2000) 299.
[106] Johnston T. W. and Dawson J. M., "Correct values for high-frequency power absorption by inverse bremsstrahlung in plasmas", *Phys. Fluids 1958-1988*, **16** (1973) 722.
[107] "FACET - Facility for Advanced Accelerator Experimental Tests." [Online]. Available: `http://science.energy.gov/hep/facilities/user-facilities/facet/`.
[108] Schroeder C., Esarey E., Geddes C., Benedetti C. and Leemans W., "Physics considerations for laser-plasma linear colliders", *Phys. Rev. ST Accel. Beams*, **13** (2010) 101301.
[109] "List of accelerators in particle physics", *Wikipedia*, 21-Nov-2016.
[110] Cheshkov S., Tajima T., Horton W. and Yokoya K., "Particle dynamics in multistage wakefield collider", *Phys. Rev. ST Accel. Beams*, **3** (2000) 71301.
[111] Green M. B. and Seiberg N., "Contact interactions in superstring theory", *Nucl. Phys. B*, **299** (1988) 559.
[112] Ellis J., Mavromatos N. and Nanopoulos D., "Derivation of a vacuum refractive index in a stringy space–time foam model", *Phys. Lett. B*, **665** (2008) 412.
[113] Tajima T., Kando M. and Teshima M., "Feeling the Texture of Vacuum Laser Acceleration toward PeV", *Prog. Theor. Phys.*, **125** (2011) 617.
[114] Caldwell A., "Collider physics at high energies and low luminosities", *Eur. Phys. J. ST*, **223** (2014) 1139.
[115] Caldwell A. and Wing M., "VHEeP: A very high energy electron–proton collider", 2016.
[116] Katsouleas S. W. T. and Su J. D. J., "Beam loading efficiency in plasma accelerators", *Part. Accel.*, **22** (1987) 81.
[117] Faure J. *et al.*, "Observation of laser-pulse shortening in nonlinear plasma waves", *Phys. Rev. Lett.*, **95** (2005) 205003.
[118] Amelino-Camelia G., Ellis J., Mavromatos N., Nanopoulos D. V. and Sarkar S., "Tests of quantum gravity from observations of γ-ray bursts", *Nature*, **393** (1998) 763.
[119] Coleman S. and Glashow S. L., "Cosmic ray and neutrino tests of special relativity", *Phys. Lett. B*, **405** (1997) 249.
[120] Coleman S. and Glashow S. L., "High-energy tests of Lorentz invariance", *Phys. Rev. D*, **59** (1999) 116008.
[121] Sato H. and Tati T., "Hot universe, cosmic rays of ultrahigh energy and absolute reference system", *Prog. Theor. Phys.*, **47** (1972) 1788.

[122] Sato H., "Extremely High Energy and Violation of Lorentz Invariance", ArXivastro-Ph0005218, May 2000.
[123] Albert J. *et al.*, "Probing quantum gravity using photons from a flare of the active galactic nucleus Markarian 501 observed by the {MAGIC} telescope", *Phys. Lett. B*, **668** (2008) 253.
[124] Aharonian F. *et al.*, "Limits on an energy dependence of the speed of light from a flare of the active galaxy PKS 2155-304", *Phys. Rev. Lett.*, **101** (2008) 170402.
[125] González M., Dingus B., Kaneko Y., Preece R., Dermer C. and Briggs M., "A γ-ray burst with a high-energy spectral component inconsistent with the synchrotron shock model", *Nature*, **424** (2003) 749.
[126] Abdo A. *et al.*, "Fermi observations of GRB 090902B: a distinct spectral component in the prompt and delayed emission", *Astrophys. J. Lett.*, **706** (2009) L138.
[127] Abdo A. *et al.*, "A limit on the variation of the speed of light arising from quantum gravity effects", *Nature*, **462** (2009) 331.
[128] Takahashi Y., Hillman L. and Tajima T., "Relativistic Lasers ans High Energy Astrophysics: Gamma Ry Bursts and Highest Energy Acceleration", in *High Field Science* (Kluwer, NY) 2000, p. 171.
[129] Narozhny N., *Sov Phys-JETP*, **27** (1968) 360.
[130] Baier V. and Katkov V., "Pair creation by a photon in an electric field", *Phys. Lett. A*, **374** (2010) 2201.
[131] Kando M. *et al.*, "Demonstration of Laser-Frequency Upshift by Electron-Density Modulations in a Plasma Wakefield", *Phys. Rev. Lett.*, **99** (2007) 135001.
[132] Miller G. H., Moses E. I. and Wuest C. R., "The national ignition facility", *Opt. Eng.*, **43** (2004) 2841.
[133] Macchi A., Cattani F., Liseykina T. V. and Cornolti F., "Laser acceleration of ion bunches at the front surface of overdense plasmas", *Phys. Rev. Lett.*, **94** (2005) 165003.
[134] Robinson A., Zepf M., Kar S., Evans R. and Bellei C., "Radiation pressure acceleration of thin foils with circularly polarized laser pulses", *New J. Phys.*, **10** (2008) 13021.
[135] Hegelich B. M. *et al.*, "Laser acceleration of quasi-monoenergetic MeV ion beams", *Nature*, **439** (2006) 441.
[136] Schwoerer H. *et al.*, "Laser-plasma acceleration of quasi-monoenergetic protons from microstructured targets", *Nature*, **439** (2006) 445.
[137] Lau C., Yeh P.-C., Luk O., McClenaghan J., Ebisuzaki T. and Tajima T., "Ponderomotive acceleration by relativistic waves", *Phys. Rev. ST Accel. Beams*, **18** (2015) 24401.
[138] Spencer I. *et al.*, "Experimental study of proton emission from 60-fs, 200-mJ high-repetition-rate tabletop-laser pulses interacting with solid targets", *Phys. Rev. E*, **67** (2003) 46402.
[139] McKenna P. *et al.*, "Characterization of proton and heavier ion acceleration in ultrahigh-intensity laser interactions with heated target foils", *Phys. Rev. E*, **70** (2004) 36405.
[140] Kim I. J. *et al.*, "Radiation Pressure Acceleration of Protons with Femtosecond Petawatt Laser Pulses", in *The International Committee on Ultrahigh Intensity Lasers (ICUIL)* (Goa, India) 2014.
[141] Macchi A., Borghesi M. and Passoni M., "Ion acceleration by superintense laser-plasma interaction", *Rev. Mod. Phys.*, **85** (2013) 751.
[142] Yin L., Albright B., Bowers K., Jung D., Fernández J. and Hegelich B., "Three-dimensional dynamics of breakout afterburner ion acceleration using high-contrast short-pulse laser and nanoscale targets", *Phys. Rev. Lett.*, **107** (2011) 45003.
[143] Tajima T. and Mourou G., "Zettawatt-exawatt lasers and their applications in ultrastrong-field physics", *Phys. Rev. ST Accel. Beams*, **5** (2002) 31301.
[144] Dubietis A., Jonušauskas G. and Piskarskas A., "Powerful femtosecond pulse generation by chirped and stretched pulse parametric amplification in BBO crystal", *Opt. Commun.*, **88** (1992) 437.

[145] Baeva T., Gordienko S. and Pukhov A., "Theory of high-order harmonic generation in relativistic laser interaction with overdense plasma", *Phys. Rev. E*, **74** (2006) 46404.
[146] Zepf M. *et al.*, "Role of the plasma scale length in the harmonic generation from solid targets", *Phys. Rev. E*, **58** (1998) R5253.
[147] Bulanov S. V., Esirkepov T. and Tajima T., "Light intensification towards the Schwinger limit", *Phys. Rev. Lett.*, **91** (2003) 85001.
[148] Zewail A. H., "Femtochemistry: Atomic-scale dynamics of the chemical bond", *J. Phys. Chem. A*, **104** (2000) 5660.
[149] Homma K., Habs D. and Tajima T., "Probing the semi-macroscopic vacuum by higher-harmonic generation under focused intense laser fields", *Appl. Phys. B Lasers Opt.*, **106** (2012) 229.
[150] Tajima T. and Homma K., "Fundamental Physics Explored with High Intensity Laser", *Int. J. Mod. Phys. A*, **27** (2012) 1230027.
[151] Ishikawa K., Tajima T. and Tobita Y., "Anomalous radiative transitions", *Prog. Theor. Exp. Phys.*, **2015** (2015) 013B02.
[152] Zhang X. *et al.*, "Particle-in-cell simulation of x-ray wakefield acceleration and betatron radiation in nanotubes", *Phys. Rev. Accel. Beams*, **19** (2016) 101004.
[153] Huang Z. and Ruth R. D., "Effects of focusing on radiation damping and quantum excitation in electron storage rings", *Phys. Rev. Lett.*, **80** (1998) 2318.
[154] Deng A. *et al.*, "Electron beam dynamics and self-cooling up to PeV level due to betatron radiation in plasma-based accelerators", *Phys. Rev. ST Accel. Beams*, **15** (2012) 81303.
[155] Itatani J., Quéré F., Yudin G. L., Ivanov M. Y., Krausz F. and Corkum P. B., "Attosecond streak camera", *Phys. Rev. Lett.*, **88** (2002) 173903.
[156] Kienberger R. *et al.*, "Atomic transient recorder", *Nature*, **427** (2004) 817.
[157] Goulielmakis E. *et al.*, "Single-cycle nonlinear optics", *Science*, **320** (2008) 1614.
[158] Uiberacker M. *et al.*, "Attosecond real-time observation of electron tunnelling in atoms", *Nature*, **446** (2007) 627.
[159] "ELI – extreme light infrastructure – european project, ELI Beamlines Facility in the Czech Republic." [Online]. Available: `http://www.eli-beams.eu/`. [Accessed: 18-Nov-2016].
[160] Mourou G. A. and Naumova N. M., "A Qualitative Introduction to Extreme Light Infrastructure", *AIP Conf. Proc.*, **1228** (2010) 1.
[161] Kaplan A. and Shkolnikov P., "Lasetron: a proposed source of powerful nuclear-time-scale electromagnetic bursts", *Phys. Rev. Lett.*, **88** (2002) 74801.
[162] Lambropoulos P., "Topics on multiphoton processes in atoms", *Adv. At. Mol. Phys.*, **12** (1976) 87.
[163] Keldysh L., "Ionization in the field of a strong electromagnetic wave", *Zh. Éksp. Teor. Fiz.*, **47** (1964) 1945; *Sov. Phys. JETP*, **20** (1965) 1307.
[164] Schwinger J., *Phys. Rev.*, **82** (1951) 664; Schanbacher V., *Phys. Rev. D*, **26** (1982) 489.
[165] Nikishov A. and Ritus V., "Quantum processes in the field of a plane electromagnetic wave and in a constant field. I", *Sov. Phys. JETP*, **19** (1964) 529.
[166] Reiss H. R., "Absorption of light by light", *J. Math. Phys.*, **3** (1962) 59.
[167] Tajima T. and Shibata K., "Plasma astrophysics", in *Frontiers in physics*, Vol. **98** (Addison Wesley, Reading, MA) 1997.
[168] Tajima T. and Necas A., "Robustness of waves with a high phase velocity", in *The Physics of Plasma-Driven Accelerators and Acceleration-Driven Fusion: The Proceedings of Norman Rostoker Memorial Symposium* Vol. **1721** (AIP, New York) 2016, p. 020006.
[169] Kotera K. and Olinto A. V., "The Astrophysics of Ultrahigh-Energy Cosmic Rays", *Annu. Rev. Astron. Astrophys.*, **49** (2011) 119.
[170] Fermi E., "Galactic Magnetic Fields and the Origin of Cosmic Radiation.", *Astrophys. J.*, **119** (1954) 1.
[171] Hillas A., "The origin of ultra-high-energy cosmic rays", *Annu. Rev. Astron. Astrophys.*, **22** (1984) 425.

[172] Chen P., Tajima T. and Takahashi Y., "Plasma wakefield acceleration for ultrahigh-energy cosmic rays", *Phys. Rev. Lett.*, **89** (2002) 161101.
[173] Nakar E., "Short-hard gamma-ray bursts", *Phys. Rep.*, **442** (2007) 166.
[174] Chang F.-Y., Chen P., Lin G.-L., Noble R. and Sydora R., "Magnetowave induced plasma wakefield acceleration for ultrahigh energy cosmic rays", *Phys. Rev. Lett.*, **102** (2009) 111101.
[175] Holcomb K. and Tajima T., "A mechanism for gamma-ray bursts by Alfvén-wave acceleration in a nonuniform atmosphere", *Astrophys. J.*, **378** (1991) 682.
[176] Ebisuzaki T. and Tajima T., "Astrophysical ZeV acceleration in the relativistic jet from an accreting supermassive blackhole", *Astropart. Phys.*, **56** (2014) 9.
[177] Shibata K., Tajima T. and Matsumoto R., "Magnetic accretion disks fall into two types", *Astrophys. J.*, **350** (1990) 295.
[178] O'Neill S. M., Reynolds C. S., Miller M. C. and Sorathia K. A., "Low-frequency oscillations in global simulations of black hole accretion", *Astrophys. J.*, **736** (2011) 107.
[179] Matsumoto R. and Tajima T., "Magnetic viscosity by localized shear flow instability in magnetized accretion disks", *Astrophys. J.*, **445** (1995) 767.
[180] Ebisuzaki T. and Tajima T., "Pondermotive acceleration of charged particles along the relativistic jets of an accreting blackhole", *Eur. Phys. J. ST*, **223** (2014) 1113.
[181] Shakura N. I. and Sunyaev R., "Black holes in binary systems. Observational appearance.", *Astron. Astrophys.*, **24** (1973) 337.
[182] Ashour-Abdalla M., Leboeuf J., Tajima T., Dawson J. and Kennel C., "Ultrarelativistic electromagnetic pulses in plasmas", *Phys. Rev. A*, **23** (1981) 1906.
[183] Esirkepov T. Z., Kato Y. and Bulanov S., "Bow wave from ultraintense electromagnetic pulses in plasmas", *Phys. Rev. Lett.*, **101** (2008) 265001.
[184] Pirozhkov A. *et al.*, "Soft-X-ray harmonic comb from relativistic electron spikes", *Phys. Rev. Lett.*, **108** (2012) 135004.
[185] Bulanov S. V., Esirkepov T. Z., Kando M., Pirozhkov A. S. and Rosanov N. N., "Relativistic mirrors in plasmas. Novel results and perspectives", *Phys.-Uspekhi*, **56** (2013) 429.
[186] Asada K. and Nakamura M., "The structure of the M87 jet: A transition from parabolic to conical streamlines", *Astrophys. J. Lett.*, **745** (2012) L28.
[187] Mima K., Horton W., Tajima T. and Hasegawa A., *Nonlinear Dynamics, and Particle Acceleration*, edited by Ichikawa Y. and Tajima T. (AIP, New York) 1991, p. 27.
[188] Ichimaru S., "Basic principles of plasma physics", 1973.
[189] Berezhiani V. and Murusidze I., "Relativistic wake-field generation by an intense laser pulse in a plasma", *Phys. Lett. A*, **148** (1990) 338.
[190] Jackson J. D., *Electrodynamics* (Wiley, New York) 1975.
[191] Urry C. and Padovani P., "Altered luminosity functions for relativistically beamed objects. II-Distribution of Lorentz factors and parent populations with complex luminosity functions", *Astrophys. J.*, **371** (1991) 60.
[192] Hartman R. *et al.*, "The third EGRET catalog of high-energy gamma-ray sources", *Astrophys. J. Suppl. Ser.*, **123** (1999) 79.
[193] Aharonian F. *et al.*, "An exceptional very high energy Gamma-Ray flare of PKS 2155–304", *Astrophys. J. Lett.*, **664** (2007) L71.
[194] Ackermann M. *et al.*, "The second catalog of active galactic nuclei detected by the Fermi Large Area Telescope", *Astrophys. J.*, **743** (2011) 171.
[195] Ajello M. *et al.*, "The luminosity function of Fermi-detected flat-spectrum radio quasars", *Astrophys. J.*, **751** (2012) 108.
[196] Broderick A. E., Chang P. and Pfrommer C., "The cosmological impact of luminous TeV blazars. I. Implications of plasma instabilities for the intergalactic magnetic field and extragalactic gamma-ray background", *Astrophys. J.*, **752** (2012) 22.
[197] Greisen K., "End to the cosmic-ray spectrum?", *Phys. Rev. Lett.*, **16** (1966) 748.
[198] Zatsepin G. T. and Kuz'min V. A., "Upper limit of the spectrum of cosmic rays", *Zh. Eksp. Toor. Fiz. Pisma Redaktsiiu*, **4** (1966) 114.

[199] Kotera K., Allard D. and Olinto A. V., "Cosmogenic neutrinos: parameter space and detectabilty from PeV to ZeV", *J. Cosmol. Astropart. Phys.*, **2010** (2010) 13.
[200] Arlen T. *et al.*, "Rapid TeV Gamma-Ray Flaring of BL Lacertae", *Astrophys. J.*, **762** (2012) 92.
[201] Takahashi Y., Collaboration J.-E. and others, "The Jem-Euso Mission", *New J. Phys.*, **11** (2009) 65009.
[202] Kajino F., collaboration J.-E. and others, "The JEM-EUSO mission to explore the extreme Universe", *Nucl. Instrum. Methods Phys. Res. A*, **623** (2010) 422.
[203] Santangelo A., Bittermann K., Mernik T. and Fenu F., "Space based studies of UHE neutrinos", *Prog. Part. Nucl. Phys.*, **64** (2010) 366.
[204] Gorodetzky P., "Status of the JEM EUSO telescope on International Space Station", *Nucl. Instrum. Methods Phys. Res. A*, **626** (2011) S40.
[205] Barwick S. *et al.*, "Constraints on cosmic neutrino fluxes from the antarctic impulsive transient antenna experiment", *Phys. Rev. Lett.*, **96** (2006) 171101.
[206] Allison P. *et al.*, "Design and initial performance of the Askaryan Radio Array prototype EeV neutrino detector at the South Pole", *Astropart. Phys.*, **35** (2012) 457.
[207] Barwick S. W., "Performance of the ARIANNA Prototype Array", in *Proceedings, 33rd International Cosmic Ray Conference (ICRC2013): Rio de Janeiro, Brazil, July 2-9, 2013*, p. 825.
[208] Gaidos J. *et al.*, "Extremely rapid bursts of TeV photons from the active galaxy Markarian 421", 1996.
[209] Albert J. *et al.*, "Discovery of very high energy γ-ray emission from the low-frequency-peaked BL lacertae object BL lacertae", *Astrophys. J. Lett.*, **666** (2007) L17.
[210] Aleksić J. *et al.*, "MAGIC discovery of very high energy emission from the FSRQ PKS 1222+ 21", *Astrophys. J. Lett.*, **730** (2011) L8.
[211] Saito S., Tanaka Y., Takahashi T., Madejski G., D'Ammando F. and others, "Very Rapid High-amplitude Gamma-Ray Variability in Luminous Blazar PKS 1510–089 Studied with Fermi-LAT", *Astrophys. J. Lett.*, **766** (2013) L11.
[212] Deng A. *et al.*, "Generation of Preformed Plasma Channel for GeV-Scaled Electron Accelerator by Ablative Capillary Discharges", *Plasma Sci. Technol.*, **13** (2011) 362.
[213] Abdo A. A. *et al.*, "The first catalog of active galactic nuclei detected by the Fermi large area telescope", *Astrophys. J.*, **715** (2010) 429.
[214] Barwick S. W., Abazajian K., Tajima T. and Ebisuzaki T., private communication (2013).
[215] Lister M. *et al.*, "MOJAVE: Monitoring of Jets in Active Galactic Nuclei with VLBA Experiments. V. Multi-Epoch VLBA Images", *Astron. J.*, **137** (2009) 3718.
[216] Marscher A. P. *et al.*, "Probing the inner jet of the quasar PKS 1510–089 with multi-waveband monitoring during strong gamma-ray activity", *Astrophys. J. Lett.*, **710** (2010) L126.
[217] Lyutikov M. and Lister M., "Resolving doppler-factor crisis in active galactic nuclei: Non-steady magnetized outflows", *Astrophys. J.*, **722** (2010) 197.
[218] Abdo A. *et al.*, "Spectral properties of bright Fermi-detected blazars in the gamma-ray band", *Astrophys. J.*, **710** (2010) 1271.
[219] Canac N., Abazajian K., Tajima T., Ebisuzaki T. and Horiuchi S., "Observational signatures of the gamma rays from bright blazars as interpreted from the wakefield theory", 2016 (private communication).
[220] Mizuta A., Ebisuzaki T., Tajima T. and Nagataki S., "GRMHD simulation of relativistic jet launch and UHECR acceleration", 2016 (private communication).
[221] Albert F. *et al.*, "Characterization and applications of a tunable, laser-based, MeV-class Compton-scattering γ-ray source", *Phys. Rev. ST Accel. Beams*, **13** (2010) 70704.
[222] Corde S. *et al.*, "Femtosecond x rays from laser-plasma accelerators", *Rev. Mod. Phys.*, **85** (2013) 1.
[223] Farinella D. *et al.*, "High energy photon emission from wakefields", *Phys. Plasmas 1994-Present*, **23** (2016) 73107.

[224] Fujiwara M. *et al.*, "Parity Non-Conservation Measurements with Photons at SPring-8", *AIP Proc.*, **802** (2005) 246.
[225] Pruet J., McNabb D., Hagmann C., Hartemann F. and Barty C., "Detecting clandestine material with nuclear resonance fluorescence", *J. Appl. Phys.*, **99** (2006) 123102.
[226] Habs D., Tajima T., Schreiber J., Barty C., Fujiwara M. and Thirolf P., "Vision of nuclear physics with photo-nuclear reactions by laser-driven$\backslash$ sf$\backslash$ gamma beams", *Eur. Phys. J. D*, **55** (2009) 279.
[227] Kikuzawa N. *et al.*, "Nondestructive detection of heavily shielded materials by using nuclear resonance fluorescence with a laser-compton scattering γ-ray source", *Appl. Phys. Express*, **2** (2009) 36502.
[228] Barty C., "Numerical simulation of nuclear materials detection, imaging and assay with MEGa-rays", presented at the Institute of Nuclear Materials Management (INMM), 2011.
[229] Phuoc K. T. *et al.*, "All-optical Compton gamma-ray source", *Nat. Photon.*, **6** (2012) 308.
[230] Powers N. D. *et al.*, "Quasi-monoenergetic and tunable X-rays from a laser-driven Compton light source", *Nat. Photon.*, **8** (2014) 28.
[231] Pagani C., Saldin E., Schneidmiller E. and Yurkov M., "Design considerations of 10kW-scale, extreme ultraviolet SASE FEL for lithography", *Nucl. Instrum. Methods Phys. Res. A*, **475** (2001) 391.
[232] Elleaume P., Chavanne J. and Faatz B., "Design considerations for a 1\AA SASE undulator", *Nucl. Instrum. Methods Phys. Res. A*, **455** (2000) 503.
[233] Lu W. *et al.*, "Generating multi-GeV electron bunches using single stage laser wakefield acceleration in a 3D nonlinear regime", *Phys. Rev. ST Accel. Beams*, **10** (2007) 61301.
[234] al Ackermann W. *et al.*, "Operation of a free-electron laser from the extreme ultraviolet to the water window", *Nat. Photon.*, **1** (2007) 336.
[235] Tolhoek H., "Electron polarization, theory and experiment", *Rev. Mod. Phys.*, **28** (1956) 277.
[236] Hajima R., Hayakawa T., Kikuzawa N. and Minehara E., "Proposal of nondestructive radionuclide assay using a high-flux gamma-ray source and nuclear resonance fluorescence", *J. Nucl. Sci. Technol.*, **45** (2008) 441.
[237] Angell C., Hajima R., Hayakawa T., Shizuma T., Karwowski H. J. and Silano J., "Demonstration of a transmission nuclear resonance fluorescence measurement for a realistic radioactive waste canister scenario", *Nucl. Instrum. Methods Phys. Res. B*, **347** (2015) 11.
[238] Crowell R. A., Gosztola D. J., Shkrob I. A., Oulianov D. A., Jonah C. D. and Rajh T., "Ultrafast processes in radiation chemistry", *Radiat. Phys. Chem.*, **70** (2004) 501.
[239] Brozek-Pluska B., Gliger D., Hallou A., Malka V. and Gauduel Y. A., "Direct observation of elementary radical events: low-and high-energy radiation femtochemistry in solutions", *Radiat. Phys. Chem.*, **72** (2005) 149.
[240] Richter C. *et al.*, "Dosimetry of laser-accelerated electron beams used for in vitro cell irradiation experiments", *Radiat. Meas.*, **46** (2011) 2006.
[241] Kneip S. *et al.*, "X-ray phase contrast imaging of biological specimens with femtosecond pulses of betatron radiation from a compact laser plasma wakefield accelerator", *Appl. Phys. Lett.*, **99** (2011) 93701.
[242] Giulietti A. *et al.*, "Intense γ-ray source in the giant-dipole-resonance range driven by 10-TW laser pulses", *Phys. Rev. Lett.*, **101** (2008) 105002.
[243] Giulietti A., *Laser-Driven Particle Acceleration Towards Radiobiology and Medicine* (Springer) 2016.
[244] Chen S. *et al.*, "MeV-energy X rays from inverse Compton scattering with laser-wakefield accelerated electrons", *Phys. Rev. Lett.*, **110** (2013) 155003.
[245] Albert F. *et al.*, "Laser wakefield accelerator based light sources: potential applications and requirements", *Plasma Phys. Control. Fusion*, **56** (2014) 84015.

[246] Tamura K. *et al.*, "X-ray induced photoelectrochemistry on TiO 2", *Electrochimica Acta*, **52** (2007) 6938.
[247] Bulanov S. and Khoroshkov V., "Feasibility of using laser ion accelerators in proton therapy", *Plasma Phys. Rep.*, **28** (2002) 453.
[248] Niculae D., Puicea F. D., Esanu I., Negoita V. and Savu D., "Development of NOTA/DOTA cyclo-RGD dimers labelled with Ga-68 for cancer diagnosis and therapy follow-up", *J. Nucl. Med.*, **54** (2013) 1131.
[249] Niculae D., "Radioisotopes for nuclear medicine: molecular imaging, targeted therapy and theranostic", 07-Jul-2016.
[250] Zulick C. *et al.*, "Energetic neutron beams generated from femtosecond laser plasma interactions", *Appl. Phys. Lett.*, **102** (2013) 124101.
[251] Kin T. *et al.*, "New production routes for medical isotopes 64Cu and 67Cu using accelerator neutrons", *J. Phys. Soc. Jpn.*, **82** (2013) 34201.
[252] Kawabata M. *et al.*, "Production and separation of 64Cu and 67Cu using 14 MeV neutrons", *J. Radioanal. Nucl. Chem.*, **303** (2015) 1205.
[253] Bracco A. and Koerner G., "NuPECC Report 'Nuclear Physics for Medicine'", presented at the Nuclear Physics European Collaboration Committee (NuPECC), 2014.
[254] Croissant J. G. *et al.*, "Protein-gold clusters-capped mesoporous silica nanoparticles for high drug loading, autonomous gemcitabine/doxorubicin co-delivery, and in-vivo tumor imaging", *J. Controlled Release*, **229** (2016) 183.
[255] Habs D. and Köster U., "Production of medical radioisotopes with high specific activity in photonuclear reactions with γ-beams of high intensity and large brilliance", *Appl. Phys. B*, **103** (2011) 501.
[256] Habs D., Tajima T. and Koster U., "Laser-Driven Radiation Therapy", in *Current Cancer Treatment - Novel Beyond Conventional Approaches*, edited by Ozdemir O. (InTech), 2011.
[257] Litvinenko V. N. and HIγS F., "Recent results with the high intensity γ-ray facility", *Nucl. Instrum. Methods Phys. Res. A*, **507** (2003) 527.
[258] Miyamoto S. *et al.*, "Laser Compton back-scattering gamma-ray beamline on NewSUBARU", *Radiat. Meas.*, **41** (2006) S179.
[259] Schiepers C. and Hoh C. K., "FDG-PET Imaging in Oncology", in *Diagnostic Nuclear Medicine* (Springer) 2006, pp. 185–204.
[260] Hayakawa T., Senzaki M., Bolton P., Hajima R., Seya M. and Fujiwara M., *Nuclear Physics and Gamma-Ray Sources for Nuclear Security and Nonproliferation: Proceedings of the International Symposium* (World Scientific) 2014.
[261] Karelin Y. A. *et al.*, "Radionuclide production at the Russia State scientific center, RIAR", *Appl. Radiat. Isot.*, **48** (1997) 1585.
[262] Knapp Jr. F. R., Mirzadeh S., Beets A. and Du M., "Production of therapeutic radioisotopes in the ORNL High Flux Isotope Reactor (HFIR) for applications in nuclear medicine, oncology and interventional cardiology", *J. Radioanal. Nucl. Chem.*, **263** (2005) 503.
[263] Carroll J. *et al.*, "Photoexcitation of nuclear isomers by (γ, γ') reactions", *Phys. Rev. C*, **43** (1991) 1238.
[264] Carroll J. *et al.*, "Excitation of Te m 123 and Te m 125 through (γ, γ') reactions", *Phys. Rev. C*, **43** (1991) 897.
[265] von Neumann-Cosel P. *et al.*, "Resonant photoexcitation of isomers. 115Inm as a test case", *Phys. Lett. B*, **266** (1991) 9.
[266] Lewis D. M., "99 Mo supply-the times they are a-changing", *Eur. J. Nucl. Med. Mol. Imaging*, **36** (2009) 1371.
[267] Raloff J., "Desperately seeking moly: Unreliable supplies of feedstock for widely used medical imaging isotope prompt efforts to develop US sources", *Sci. News*, **176** (2009) 16.
[268] Uusijärvi H., Bernhardt P., Rösch F., Maecke H. R. and Forssell-Aronsson E., "Electron-and positron-emitting radiolanthanides for therapy: aspects of dosimetry and production", *J. Nucl. Med.*, **47** (2006) 807.

[269] Anderson C. J. and Ferdani R., "Copper-64 radiopharmaceuticals for PET imaging of cancer: advances in preclinical and clinical research", *Cancer Biother. Radiopharm.*, **24** (2009) 379.
[270] "International Center for Zetta-Exawatt Science and Technologyk, Ecole Polytechnique." [Online]. Available: `https://portail.polytechnique.edu/izest/en`. [Accessed: 18-Nov-2016].
[271] "International Committee on Ultrahigh Intensity Lasers Germany." [Online]. Available: `http://www.icuil.org/`. [Accessed: 18-Nov-2016].
[272] Wheeler J., Mourou G. and Tajima T., *Rev. Accel. Sci. Technol.*, in press 2017.
[273] Shin Y.-M., "Beam-driven acceleration in ultra-dense plasma media", *Appl. Phys. Lett.*, **105** (2014) 114106.